Towards ultrafast time-resolved experiments with nanoscale objects and surfaces

Dissertation

zur Erlangung des Doktorgrades
an der Fakultät für Mathematik, Informatik und Naturwissenschaften
Fachbereich Physik
der Universität Hamburg

Julia Hengster
aus Karlsruhe, Deutschland

Dezember 2016

1. Gutachter: JProf. Dr. Thorsten Uphues
2. Gutachter: Prof. Dr. Franz X. Kärtner

3. Gutachter: Prof. Dr. Robin Santra (Vorsitz der Prüfungskommission)
4. Gutachter: Prof. Dr. Wilfried Wurth
5. Gutachter: PD. Dr. Tim Laarmann

Disputation: 13. April 2017

Acknowledgements

I thank my supervisor JProf. Thorsten Uphues for giving me the opportunity to work in this challenging but interesting topic of attosecond science that is both connected to laser physics and to surface science. I am grateful for his hints for constructing the beamline, his patience in answering all the questions and the curiosity resulting in an uncountable number of ideas leading into interesting projects. I learned a lot about laser and nano science but also beyond during the last four years!

Additionally I thank Prof. Franz X. Kärtner for examining this thesis and being my co-supervisor within the IMPRS (International Max Planck Research School). Especially in the regular meetings he gave me good advise for reaching my goals. He is always keen on common projects bringing the knowledge of different groups together to outreach the individual abilities.

I am very grateful to my former group with Svetoslav Stankov, Anja Seiler, Shyjumon Ibrahimkutti and Ramu Pradip from the Karlsruhe Institute of Technology for enabling the sample characterisation with XPS and XRD.

My thanks also go to Prof. Armin Scrinzi and Mattia Lupetti for co-working on the idea of attosecond photoscopy and the proposal of the experimental realisation.

Also, I would like to thank the group of John Tisch from Imperial College, London, especially William Okell for the common beamtime with the gold and tungsten streaking experiments.

More thanks go to Prof. Holger Lange, Dr. Julia Rehbein, and Prof. Patrick Theato from the chemistry department, including their group members Florian Schulz, Sebastian Herrmann, Björn Mahrt, Nathalie Wagner and Michael Thielke for the sample preparation of different samples. Additionally I want to thank Charlotte Ruhmlieb und Svenja Patjens (AK Mews) for their help with the CVD preparation and AFM characterisation.

I am thankful to Miriam Barthelmeß for enable some first FIB sample structuring and AFM characterisation measurements.

I thank the CFEL team of the AG Wurth especially Giuseppe, Lukas and Florian for conducting XPS measurements on the UV ozone cleaned nanoparticle sample and helping out with vacuum parts. Special thanks go to Florian Hieke, who accompanied me running almost every thursday and helped to fight against the "Inneren Schweinehund".

More thanks go to Martin Michelswirth from Bielefeld who teached me a lot about XPS analysis and chemistry.

I want to thank the IMPRS with the three coordinators Anja Bleidorn, Sonia Utermann and Julia Quante and all the students. Within the IMPRS I could attend very helpful soft skill courses, as well as scientific courses, that helped a lot in everday life! Especially I want to thank all the other IMPRS fellows for having a lot of fun within the four years during the annual retreats, the PhD seminars and during other courses.

Additionally I want to thank Marek Wieland and Oliver Becker from the AG Drescher for helping out with vacuum, optic components and the installation of water or gas supply. Special thanks go to the leader of the mechanical workshop Stephan Fleig and his team manufacturing all the special components for the beamline and to the team of the electronics workshop. Also I want to thank our housekeeper Gisbert Mantei for the technical support during the numerous incidents and providing us left over food from all the events. Additionally, I want to thank all the people that are not named here explicitly for the good times during my PhD.

Special thanks go to our group members Alex, Ute, Tanja, Igor, Rene, Klaas and Joachim and the former group members Thomas, Niculina and Alex for the enjoyable time and helping in everyday office and lab life. I also want to thank the colleagues from the AG Frühling Ulrike, Martin, Markus and Sophie and Theo and Marie for the enjoyable times in the shared lab and the coffee breaks.

List of publications

Journal publications

- Okell, W. A. et al. Temporal broadening of attosecond photoelectron wavepackets from solid surfaces. Optica **2**, 383 (2015).
- Lupetti, M., Hengster, J., Uphues, T., Scrinzi, A. Attosecond Photoscopy of Surface Plasmon Polaritons. Phys. Rev. Lett. **113**, 113903 (2014).

Conference and Workshops: Talks

- Joint IMPRS Workshop 'Quantum Dynamics and Photon-Matter Interaction', Dresden, Germany (2013)
- LPHYS'13 , Prague, Czech Republic, (2013)
- LPHYS'14 , Sofia, Bulgaria (2014)
- Silap, Bordeaux, France (2015)

Conference and Workshops: Posters

- Fall School DFG Research Training Group 1355, Hamburg, Germany (2013)
- 3rd Summer School Ultrafast Nanooptics, Mülheim/Ruhr, Germany (2013)
- Photon14, London, United Kindom (2014)
- WE Heraeus Workshop - Ultrafast phenomena at nanostructures , Les Houches, France (2015)

Eidesstattliche Erklärung

Hiermit erkläre ich an Eides statt, die vorliegende Dissertation selbst verfasst und keine anderen als die angegebenen Hilfsmittel benutzt zu haben

22. Dezember 2016 Julia Hengster

Abstract

Attosecond streaking is an established technique for the investigation of ultrafast phenomena in atomic and molecular physics. The demonstration of attosecond streaking on solid surfaces revealed ultrafast dynamics in the electron transport properties already. However, only a few single crystalline materials have been investigated so far. The potential applicability to plasmonic nanostructured or thin film samples maintaining ultrafast electron oscillations on the time-scale of attosecond has not been realized yet. In this thesis proof-of-principle experiments on gold and tungsten trioxide demonstrate, that surface contaminated and polycrystalline or amorphous samples are applicable for the investigation with attosecond streaking. In these experiments, a broadening of the photoelectron wavepackets compared to the laser pulse was found. Furthermore, a sample cleaning procedure is established to prepare nanostructured samples nondestructively. Simulations are performed for the design and optimisation of vertical disk resonators. Special attention was turned on the orientation of the electric field to make the plasmonic field accessible in the streaking experiments. Additionally, the appearance of ultrafast surface modes is investigated. The realisation of the nanodisk resonators has been started by preparation of thin film triple layers and first characterisation measurements. For ultrafast time-resolved measurements on the simulated nanostructures and thin films a beamline for the generation of isolated attosecond pulses by high harmonic generation was built.

Zusammenfassung

Attosekunden-zeitaufgelöstes Photoelektronen Streaking ist eine etablierte Methode für die Untersuchung von extrem schnellen Prozessen in Atomen und Molekülen. Durch die Anwendung dieser Technik auf Festkörperproben konnten auch in solchen Systemen ultraschnelle Dynamiken beim Elektronentransport nachgewiesen werden. Jedoch wurden bislang nur wenige einkristalline Materialien untersucht. Auf nanostrukturierte plasmonische Proben oder dünne Filme, die ebenfalls elektronische Dynamiken auf einer ähnlichen Zeitskala aufweisen, wurde die Streaking-Technik bisher noch nicht angewendet.

Im Rahmen dieser Dissertation wurden Streaking-Experimente an Gold- und Wolframtrioxid Proben durchgeführt, die die prinzipielle Anwendbarkeit dieser Technik auf polykristalline und amorphe Proben mit Oberflächenkontamination zeigen. In diesen Experimenten wurde eine Verbreiterung des Photoelektronen-Wellenpackets relativ zur Laserpulsdauer nachgewiesen. Weiterhin wurde eine Präparationsprozedur entwickelt, mit deren Hilfe nanostrukturierte Proben zerstörungsfrei von Oberflächenkontaminationen gereinigt werden können.

Mit Hilfe von Simulationen wurden Mehrschicht-Resonatoren bestehend aus drei Scheiben entworfen und optimiert, die eine Orientierung des elektrischen Feldes senkrecht zur Oberfläche aufweisen. Damit erfüllen sie eine wichtige Anforderung, um in einem modifizierten plasmonischen Streaking-Experiment analysiert zu werden, da nur der Einfluss elektrischer Felder in Richtung des Elektronendetektors messbare Beiträge liefert. Außerdem wurde die Erzeugung von unterschiedlichen Oberflächen-Moden untersucht. Mit der Präparation von solchen Nanodisk-Resonatoren wurde bereits begonnen. Ein dreilagiges Schichtsystem wurde präpariert und daran erste Charakterisierungsmessungen durchgeführt.

Um zeitaufgelöste Experimente an den simulierten Nanostrukturen durchführen zu können wurde außerdem eine Apparatur zur Erzeugung von isolierten Attosekunden Pulsen auf Basis der hohen harmonischen Erzeugung aufgebaut, die die beschriebenen Experimente ermöglichen soll.

Contents

1. Introduction

Plasmonics has a long history and dates back to the Roman period of time where nanoparticles were used for the colouring of glass [1]. However, to discover the optical properties however took a long time up to the 20th century when collective electron motions were described for the first time as plasma oscillations [2] and their systematic excitation was studied [3, 4]. The applications of nanoparticles today have various fields. They are likely to revolutionize cancer therapy, where nanoparticles are used as tumor markers to destroy selectively only the cancer cells [5–7] or in diagnosis [8]. In the chip industry plasmonic structures such as waveguides or switches are potentially used as next generation components to speed up communication electronics so a new level. The way to ever faster information processing led to a broad interest and development of plasmonic devices bridging the limited operation speed of electrons and the limited feature size of dielectric photonics [9–11]. Understanding plasmons as collective oscillations of the free-electron gas density at optical frequencies raises important questions related to their propagation, damping and finally charge localization. A new type of question came up with respect to their plasmonic behaviour in space and more importantly in time, following the complex dynamics of the electromagnetic field [12–14].

The history of time-resolved imaging is comparably young and dates back to the 1870s when Eadweard Muybridge started time resolved photography to visualize the movement of a horse. Nowadays, time-resolved spectroscopy methods are used to visualize processes in structures smaller than six orders of magnitudes of the size of a horse. At the same time, the time-scale of the sampling event has been reduced by more than fourteen orders of magnitude enabling the time-resolved investigations of events on this time scale. At the femtosecond and attosecond time-scale one addresses fundamental electronic processes in atoms [15, 16], molecules [17–19] and surfaces [20–22].

The development in ultrafast laser physics [23–25] and spectral selection techniques of the energetic high harmonic radiation [26, 27] have evolved the pulse duration reached with high harmonic generation in the some ten attosecond regime. The attosecond streaking technique became an established setup for the investigation of fundamental processes happening on this time-scale [28, 29]. The shortest pulse duration depicting the edge of recent time resolution is defined by the shortest pulse which is currently $67\,\mathrm{as}$ [30].

In the first section of this thesis fundamental plasmon theory is introduced based on the interaction of light with matter described by Maxwell's Equations and the scattering at particles is described. The properties of surface plasmon polaritons are derived and different setups for their excitation are introduced. A surface plasmon polariton propagates at the interface of a metal and dielectric. During propagation it is damped and vanishes. The refinement of a surface plasmon to a particle is described by localised surface plasmons, where the electronic wave cannot leave the particle. When a plasmonic particle can be decomposed into more fundamental particle geometries, the response is determined by the interaction of

both fundamental plasmons. This effect is called hybridisation and is of fundamental interest throughout this work. Studying solid state samples, one has to take the band structure into account. Here, an optical excitation can transfer electrons from one energy band into another (interband plasmons) or within one band (intraband plasmons). This chapter closes with a short overview over preparation schemes and characterisation of plasmonic particles in general.

The next chapter covers attosecond physics. Fundamental basics in femtosecond laser physics as the generation of femtosecond pulses, the influence of the carrier envelope phase and its control are described. The scheme of high harmonic generation is explained, where infrared laser pulses are converted to extreme ultraviolet pulses, which built the basis for the generation of isolated attosecond pulses. Finally photoelectron spectroscopy is treated with a general description of electron transport mechanisms and attosecond streaking in gases and in condensed matter. The theoretical approach of attosecond photoscopy describes the adoption of streaking on condensed matter to plasmonic samples.

The investigation of samples with time-resolved photoelectron spectroscopy in the time domain is sensitive to the electric field direction towards the electron detector. Therefore, to find sample geometries where the electric field vector is oriented normal to the surface plane is of special interest. In the chapter of simulation gold-silica-gold and gold-silica-silver nano resonators are investigated, where the evolving electric field fulfils this requirement. The silica layer is a dielectric layer between the two interacting metal disks which determines the response of the resonator. In the simulation of gold-silica-gold sandwiches the influence of geometrical asymmetry is investigated by varying the disk thickness of the top disk and the diameter ratio of the top and bottom disk. Both parameters change the response attributed to hybridisation. By changing the material of the top disk in the gold-silica-silver sandwich an asymmetry in the dielectric function is introduced leading to a fundamental change in the response. In both sandwich structures surface plasmon modes are excited. The superposition of these modes shows a complex electric field pattern that changes within a few femtoseconds.

In the experimental part of this work the attosecond streaking on gold and oxidized tungsten films is presented. These experiments are proof-of-principle experiments, to demonstrate the streaking technique on non-crystalline and non-UHV prepared thin film samples. Both films are characterised accurately regarding their crystallinity and surface contamination with X-ray diffraction and X-ray photoelectron spectroscopy. The surface topology is investigated with atomic force microscopy. Furthermore, a non-destructive cleaning strategy for the preparation of nanostructures is shown based on UV-ozone cleaning.

The next step towards attosecond streaking experiments on the disk resonators is the preparation of triple layers of thin films and their characterisation. The triple layers are sputter-coated and characterised with X-ray photoelectron spectroscopy and atomic force microscopy. First angular resolved reflectivity measurements show the possibility of efficient coupling to plasmonic interactions.

Finally the beamline which was built in the framework of this thesis for photoelectron spectroscopy with isolated attosecond pulses is described . The laser system delivering the driving pulses for high harmonic radiation is discussed. The setup for incoupling the NIR beam is simulated for optimizing the focus radius and wavefront. The requirement of ultra-high vacuum conditions in the experimental chamber affects the vacuum setup of the whole

system. Furthermore, several devices have been built for sample and light manipulation as well as detectors for the measurement of the harmonic and electron spectrum. The HHG beam is characterised for its beam diameter and source size.

In a final section the calibration of the electron detector with xenon is proposed. Finally a proof-of-principle experiment is suggested to study the charge migration in a benzene ring in bromo-(L)-phenylalanin.

2. Plasmonics

2.1. Historical review

A plasmon is the collective oscillation of charge carriers and can be excited by an external electric field, e.g. a short laser pulse. For surfaces and nanostructures two kinds of plasmons occur: propagating surface plasmon polaritons (SPP) and localized surface plasmons (LSP). In the case of LSP the motion of the electrons are localized to the surface of a nanoparticle, whereas SPPs can propagate along a metal-dielectric interface over a long distance.

One of the first applications of plasmons was the colouration of glass already in the 4th century in Roman times. The extraordinary impressive Lycurgus cup (The British Museum, London) is made of glass doped with gold and silver colloidal nanoparticles which give the characteristic colour [1]. Depending on the illumination the cup appears green (illumination from front) or red (behind). Many centuries later the same technique was still used to colourize church windows, e.g. Notre Dame in Paris, France. Before the 20th century it was not understood what effects the colouration in these glasses. In 1902, *Wood* discovered anomalies in diffraction grating experiments [31]. He found that the intensity of the diffracted maxima depends on the angle of incidence. *Lord Rayleigh* gave a physical explanation only a few years later in 1907 [32] but without associating the anomalies to the motion of electrons. Almost 40 years later *Fano* explained the diffraction grating anomalies with quasi-stationary waves representing an energy current propagating along the surface of a metal [33]. The coupling of a light wave to a current wave requires a matching angle of incidence to maximize the energy transfer. *Bohm and Pines* described the collective motion of electrons in a dense electron gas as plasma oscillations theoretically in the 1950s [2]. They obtained a Hamiltonian covering both the collective oscillation of electrons and the individual electronic interactions. In the 1950s, *Kretschmann* and *Otto* investigated the coupling of light and plasmons and proposed two setups for efficient coupling [3, 4].

With respect to this long history, it is remarkable that the impact of plasmons on technology has become visible just recently. *Brongersma* and *Shalaev* figured out the potential of plasmonic devices in information technology [9]. Plasmonic devices can overcome the miniaturisation problem in photonic devices and the limited operation speed in electronic devices by coupling the benefits of both, the speed of light in photonics and the nanometre scale of electronics. Also in health care the impact of nanoparticle applications grows. In cancer diagnosis nanoparticles improve the targeting of tumour cells [7, 8] and have the potential to revolutionize cancer therapy [5, 6]. The behaviour of nanoparticles will be explained in more detail in the following sections.

This section covers the theoretical aspects of plasmonics starting with the fundamental Maxwell equations, Mie theory describing the scattering and absorption of light in particles on the basis of Maxwell's equations, the origin of SPPs and LSPs, as well as experimental

methods to launch and characterize plasmons.

2.2. Macroscopic Maxwell's equations

The behaviour of matter interacting with electromagnetic waves is determined by the electronic properties. Free and bound charge carriers built up free and bound currents. Both contribute to the total current density: $\mathbf{J} = \mathbf{J}_f + \mathbf{J}_b$. The free current density is induced by an electric field $\mathbf{J}_f = \sigma\mathbf{E}$ with the conductivity σ. Bound currents result from not uniformly distributed charges from temporarily changing electric or circulating magnetic dipole moments referred to as polarisation and magnetisation:

$$\textbf{Polarisation} \qquad \mathbf{P} = \epsilon_0\chi\mathbf{E} \tag{2.1}$$

$$\textbf{Magnetisation} \qquad \mathbf{M} = \chi_M\mathbf{H}. \tag{2.2}$$

The electric susceptibility χ, magnetic susceptibility χ_M, permittivity ϵ, and permeability μ are material properties, with the assumption that the medium is homogeneous, isotropic, and linear [34]. Vacuum permeability and permittivity are constants for the absence of matter and contribute to the values in matter with $\epsilon = \epsilon_0\epsilon_r$ and $\mu = \mu_0\mu_r$.

The electric displacement $\mathbf{D} = \epsilon_0\mathbf{E} + \mathbf{P}$ is a field resulting from an external field and the affected polarisability of the material. The magnetisation of matter together with the magnetic field $\mathbf{B}$ contribute to the magnetic field $\mathbf{H} = \frac{\mathbf{B}}{\mu_0} - \mathbf{M}$.

The interactions of light with matter are described by the macroscopic Maxwell's equations [34]:

$$\textbf{div } \mathbf{D} = \rho_F \qquad \textbf{Gauss's law} \tag{2.3}$$

$$\textbf{div } \mathbf{B} = 0 \qquad \textbf{Gauss's law for magnetism} \tag{2.4}$$

$$\textbf{rot } \mathbf{E} = -\frac{\partial \mathbf{B}}{\partial t} \qquad \textbf{Faraday's law} \tag{2.5}$$

$$\textbf{rot } \mathbf{H} = \frac{\partial \mathbf{D}}{\partial t} + \mathbf{J}_f \qquad \textbf{Ampere's law} \tag{2.6}$$

with electric displacement $\mathbf{D}$, the electric charge density ρ, the magnetic field $\mathbf{H}$, and the free current density $\mathbf{J}_f$.

The Gauss's law means that charges are the source of an electric field. The meaning of Gauss's law for electromagnetism is that there are no magnetic charges that induce the $\mathbf{B}$-field but it is created by dipoles and is a solenoidal field. The Faraday law connects the dynamics of a magnetic with an electric field, meaning that a temporal change of a magnetic field induces an electric one. The induction of a magnetic field by electric currents and temporally changing electric fields is stated in Ampere's law. [35]

The microscopic Maxwell equations are obtained by zeroing the magnetisation and polarisation. Science agrees universally on the microscopic Maxwell equations, whereas the macroscopic Maxwell equations have been further developed throughout the past years with new derivations claiming a more general and logical consistence [34].

2.3. Scattering at particles

The scattering of light at particles depends on the the relative size of the particle compared to the wavelength of the incoming light. Is the particle much bigger than the wavelength $s > 2 \ldots 10\lambda$, the scattering of light beam from dust particles the classical scattering theory can be applied. If the particle becomes smaller close to the wavelength $s \simeq \lambda$, e.g. scattering of light in a glass of milk, the Mie theory can be used. When the particle size is further reduced to $s < 0.2\lambda$, e.g. scattering of sun light on atmospheric particles resulting in the blue sky or the red colour of sunrises and sunsets, the theory of Rayleigh scattering is applied.

LSPs can be treated by Mie scattering. The resonant scattering is typically in the range of the particle size or above. The Mie theory is solved exactly only for spherical particle geometries. For solving scattering problems with non spherical particles one has to go beyond.

The Mie theory solves the Maxwell equations exactly [36]. A derivation is given by *Bohren* and *Huffman* in [34] or by *Hergert* and *Wriedt* in [37]. For an homogeneous, isotropic sphere the scattering and extinction cross sections are calculated for the number n of multipoles [34]:

$$C_{sca} = \frac{2\pi}{k^2} \sum_{n=1}^{\infty} (2n+1)(|a_n|^2 + |b_n|^2) \tag{2.7}$$

$$C_{ext} = \frac{2\pi}{k^2} \sum_{n=1}^{\infty} (2n+1)\,\mathrm{Re}(a_n + b_n) \tag{2.8}$$

with the wavevector k of the incoming wave, the multipole order n, and the scattering coefficents a_n and b_n:

$$a_n = \frac{m\psi_n(mx)\psi_n'(x) - \psi_n(x)\psi_n'(mx)}{m\psi_n(mx)\xi_n'(x) - \xi_n(x)\psi_n'(mx)} \tag{2.9}$$

$$b_n = \frac{\psi_n(mx)\psi_n'(x) - m\psi_n(x)\psi_n'(mx)}{\psi_n(mx)\xi_n'(x) - m\xi_n(x)\psi_n'(mx)} \tag{2.10}$$

with the relative refractive index $m = \frac{N_{part}}{N_{med}}$ of medium and particle refractive index and the Riccati-Bessel functions ψ_n and ξ_n. The efficiencies Q_{sca} and Q_{ext} are related to the cross sections and the cross sectional area by:

$$Q_{sca} = \frac{C_{sca}}{\pi a^2} \qquad \text{and} \qquad Q_{ext} = \frac{C_{ext}}{\pi a^2} \tag{2.11}$$

For calculating more sophisticated particle geometries one has to remodel the Mie theory. For modelling the scattering at an ellipsoidal sample geometries, cylinders, or others, I refer to *Bohren* and *Huffman* [34]. A quite general approach is the discrete dipole approximation (DDA), where the nanoparticle is represented as three dimensional dipole distribution. The reaction of the system is then calculated from the excitation with electric light field and the interplay between the dipoles.

2.4. Surface plasmon polaritons

For the understanding of surface plasmon polaritons (SPPs) it is important to understand the optical properties of metals. The plasma model describes the valence electrons in a metal as a free electron gas within a periodic ionic potential and external electric field [38]. The electrons can be excited by an external electric field, e.g. a light wave, described by the equation of motion:

$$m\mathbf{x}''(t) + m\gamma\mathbf{x}'(t) = -e\mathbf{E}(t) \tag{2.12}$$

with the electronic mass m, the damping coefficient due to collisions γ, and the harmonic driving light field $\mathbf{E}(t) = \mathbf{E}_0 \exp(-i\omega t)$ with the angular frequency ω and the amplitude E_0. Solving this differential equation leads to the collective oscillatory movement of electrons $\mathbf{x}(t) = \mathbf{x}_0 \exp(-i\omega t)$. The response of the electron gas incorporates phase shifts that are considered in the complex amplitude $\mathbf{x}_0$:

$$\mathbf{x}(t) = \frac{\mathbf{x}_0}{\mathbf{E}_0}\mathbf{E}(t) = \frac{e}{m(\omega^2 + i\gamma\omega)}\mathbf{E}(t) \tag{2.13}$$

The plasma frequency of the free electron gas is related to the macroscopic polarization resulting from the displaced electrons $\mathbf{P} = -ne\mathbf{x}$, with the number n and the charge e of electrons. The electric displacement is calculated by:

$$\mathbf{D} = \epsilon_0\mathbf{E} + P = \epsilon_0\mathbf{E} - ne\mathbf{x} = \epsilon_0\left(1 - \frac{ne^2}{\epsilon_0 m(w^2 + i\gamma\omega)}\right)\mathbf{E} = \epsilon_0\epsilon_r\mathbf{E} \tag{2.14}$$

This leads to the definition of the plasma frequency ω_p and the dielectric function $\epsilon(\omega)$:

$$\omega_p := \sqrt{\frac{ne^2}{\epsilon_0 m}} \qquad \text{and } \epsilon(\omega) = \epsilon_0\epsilon_r(\omega) \tag{2.15}$$

In Table 2.1 values for the plasma frequency ω_p for common metals are given.

Metal	Au	Ag	W	Pt	Cu
ω_p / eV	9.03	9.01	6.39	5.15	7.39

Table 2.1.: Plasma frequencies for metals typically used in plasmonic studies. Experimental data taken from [39].

In the Drude model $\epsilon(\omega) = 1 - \omega_p^2/\omega^2$, the discontinuity of the surface normal component of the electric field at the surface leads to $\epsilon(\omega) = -1$, and the surface plasma frequency is calculated by [40, 41]:

$$\omega_{SPP} = \frac{\omega_p}{\sqrt{2}} \tag{2.16}$$

In the case that the metal has a covering oxide layer or contact to another dielectric layer with the dielectric function ϵ_d, but not vacuum, the surface plasma frequency is shifted [38]:

$$\omega_{SPP} = \frac{\omega_p}{\sqrt{\epsilon_d + 1}} \tag{2.17}$$

and the wave vector of a SPP propagating along a surface is determined by:

$$k_{SPP} = \frac{\omega}{c}\sqrt{\frac{\epsilon_d \epsilon}{\epsilon_d + \epsilon}} \tag{2.18}$$

with the speed of light c.

For a multilayer system where a thin metal film with thickness $2a$ is covered by a dielectric with $\epsilon_2$on both sides, on both interfaces an SPP is excited:

$$\omega_+ = \frac{\omega_p}{\sqrt{1+\epsilon_2}}\sqrt{1 + \frac{2\epsilon_2 \exp(-2ka)}{1+\epsilon_2}} \tag{2.19}$$

$$\omega_- = \frac{\omega_p}{\sqrt{1+\epsilon_2}}\sqrt{1 - \frac{2\epsilon_2 \exp(-2ka)}{1+\epsilon_2}} \tag{2.20}$$

with the wavevector k The propagation of a plasmonic wave along the surface of a metal is illustrated in Figure 2.1. The electric light field drives the quasi-free electrons to delocalise

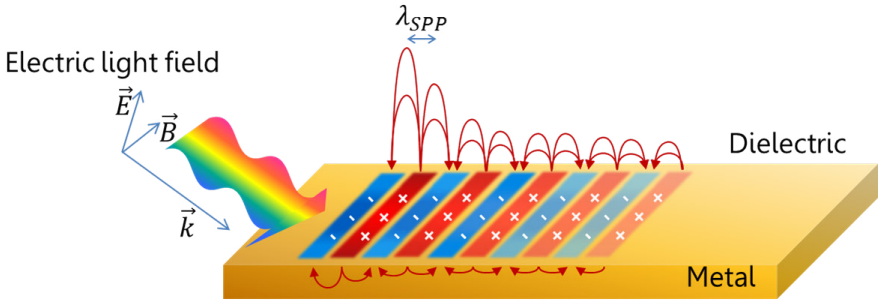

Figure 2.1.: Surface plasmon polariton at a metal dielectric interface. Figure adapted from [38].

and separate in positively and negatively charged regions. From the delocalisation an electric field builds up inside and outside the material driving the electrons back to their initial position. From this, an oscillation of electrons is initiated and results in an oscillating electric field with ω_{SPP} that propagates on the surface with k_{SPP}.

The dispersion relation describing the wavevector sensitive oscillation frequency of a free electron gas is given for the case that $\omega > \omega_p$ by:

$$\omega/\omega_p = \sqrt{1 + k^2 c^2}/\omega_p \tag{2.21}$$

In this regime the propagation of transverse electromagnetic waves, i.e. SPPs, are allowed. Different methods for the excitation of SPPs are explained in the following section.

2.5. Excitation of surface plasmon polaritons

There are different possibilities for the optical excitation of surface plasmon polaritons (SPP), e.g. prism- and grating coupling, or by strong focussing of optical beams. The main issue

launching a SPP is the difficulty of phase matching of the group velocities of the SPP and the light wave. Additionally the evanescent nature of the SPP requires an evanescent wave to be launched. [38] To fulfil the first requirement one has to match the wavevectors of the SPP and the incident light $\vec{k}_{SPP} = \vec{k}$ [3]. The second requirement can be realised by special light coupling with a grating or prism coupler where the dispersion is modified by propagation in glass or the modification of the metallic surface. The strong focusing technique uses an microscope objective with a high numerical aperture including angles of incidence greater than the critical angle for total internal reflection. At the surface the incident beam is reflected, but slightly shifted to the initial position (Goos-Hänchen effect [42]) so that the virtual reflection surface lies inside the material. The result is an evanescent wave on the surface, which excites a SPP on a metallic surface as a consequence.

In the following, two prism coupling techniques are presented. The Kretschmann [3] and Otto [4] configurations are possibilities to excite SPPs and are depicted in Figure 2.2 a) and b), respectively.

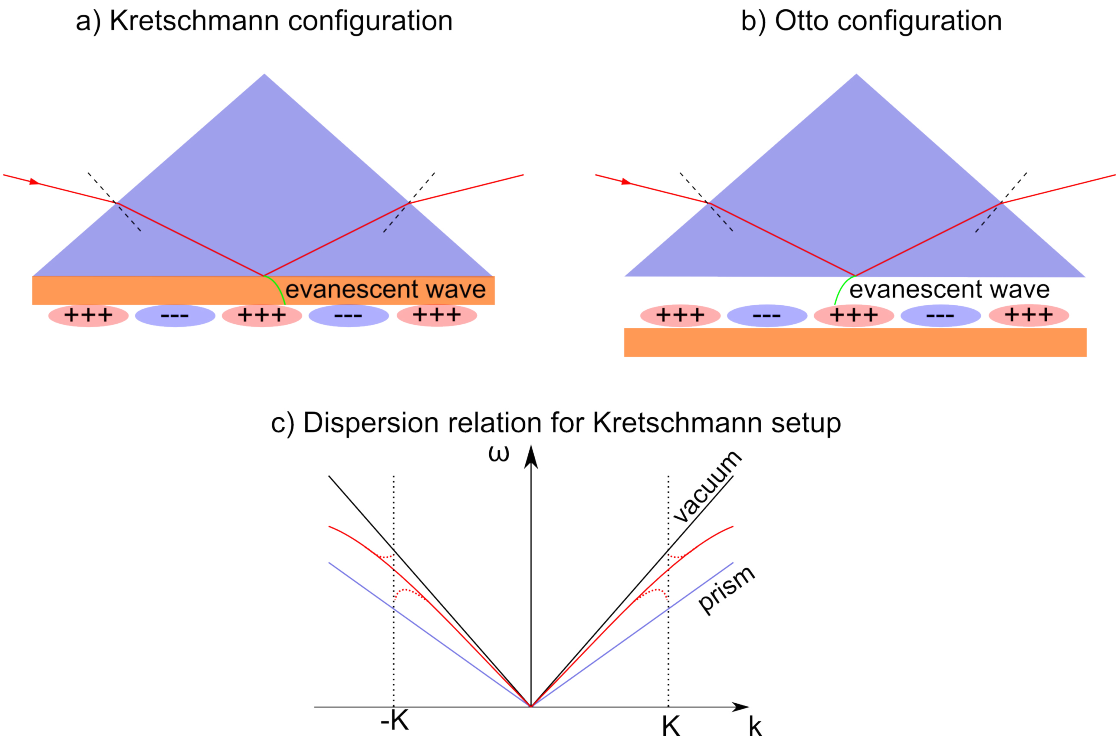

Figure 2.2.: Kretschmann a) and Otto b) configuration for launching SPPs and c) dispersion relation for the Kretschmann setup. Adapted from [38, 43]

In both setups the incoming light wave is propagating from air or vacuum into a glass prism. At the prism base the light wave is totally reflected and an evanescent wave is built up. In the Kretschmann configuration a metal film is evaporated directly on the prism base. Therefore, the evanescent wave resulting from the total reflection travels at the glass-metal interface. In the Otto configuration there is a dielectric (air) gap between the prism and the

metallic film. The evanescent wave propagates at the glass-air interface but the electric field still penetrates into the metallic film. This leads to a delocalisation of electrons resulting in a plasmonic oscillation. Figure 2.2 c) shows the dispersion relation for a metallic grating structure at the prism base. The light line in air and in the prism represent the dispersion $\omega(k)_{vacuum/prism} = kc_{air/prism}$ of light propagating in air and prism, respectively. The dispersion curve for the SPP is in between and intersects at a certain point k_{SPP} with the light and the prism light line. This determines the wave vector that efficiently transfers energy from the light wave to the plasmonic wave according to Equation 2.18.

2.6. Localised surface plasmons

The second class of plasmons are non-propagating localised surface plasmons (LSPs) that are refined in a conductive or metallic particle. LSPs can be excited directly by an oscillating electromagnetic field. The resonant modes of LSPs originate from the scattering of small particles described in Section 2.3 [38]. An approach from electrostatics is to calculate the electric field for a spherical particle starting from:

$$\mathbf{E} = -\nabla\Phi \tag{2.22}$$

with the potentials inside and outside the sphere:

$$\Phi_{in}(r,\theta) = -\tfrac{3\epsilon_d}{\epsilon+2\epsilon_d} E_0 r\cos\theta \tag{2.23}$$

$$\Phi_{out}(r,\theta) = -E_0 r\cos\theta + \tfrac{\epsilon-\epsilon_d}{\epsilon-2\epsilon_d} E_0 a^3 \tfrac{\cos\theta}{r^2} \tag{2.24}$$

with the dielectric functions of the sphere material ϵ, surrounding material ϵ_d, the radius of the sphere a, and the incoming field E_0. For scattering and absorption cross sections one finally obtains:

$$C_{sca} = \frac{8\pi}{3} k^4 a^6 \left|\frac{\epsilon-\epsilon_d}{\epsilon+2\epsilon_d}\right|^2 \tag{2.25}$$

$$C_{abs} = 4\pi k a^3 \mathsf{Im}\left(\frac{\epsilon-\epsilon_d}{\epsilon+2\epsilon_d}\right) \tag{2.26}$$

Nanoparticles are typically spherical or elliptical particles but can also be antenna structures composed of nanorods or bow-ties. The plasmon resonance depends on the geometrical particle dimensions and the material of the particle itself and the surrounding medium. Figure 2.3 demonstrates the resonance wavelength shift in the absorption spectra for different gold rod nanoparticles with varying length. The particles have equal thickness and height of $40\,\mathrm{nm}$ with an increasing length from $120\,\mathrm{nm}$ to $160\,\mathrm{nm}$. With increasing length the resonance shifts about $100\,\mathrm{nm}$ to longer wavelengths.

Nanoplasmonic particles have many applications due to their tunable resonance wavelength [44]. They are used in wavelength sensitive light detection [45], in biomedicine for cancer diagnosis and therapy [6, 8, 46], or optical antennas [47].

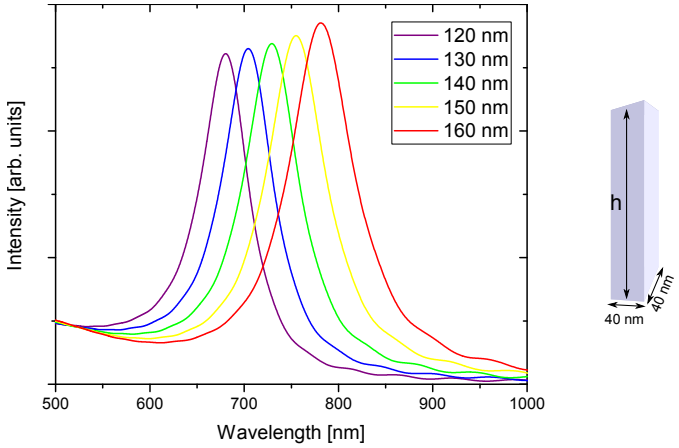

Figure 2.3.: Absorption spectra of different gold nanorods with a length from $120\,\mathrm{nm}$ to $160\,\mathrm{nm}$ and a thickness and height of $40\,\mathrm{nm}$.

2.7. Hybridisation of plasmons

For the treatment of the response of complex plasmonic nanoparticle geometries *Prodan et al.* developed the model of hybridization [48]. The hybridization model is the simplification of a complex sample geometry to a more general one. Hybridization is the existence of different plasmon modes originating from the fundamental underlying structures. Also structures composed of different materials like metals, insulators, or semi-metals can hybridize. The principle of hybridisation is explained on the example of a metal nanoshell particle in Figure 2.4. The nanoshell particle is composed of a spherical particle and a cavity both supporting a distinct resonance frequency. During the plasmonic excitation electrons are driven to one side of the particle, on the opposite side the positively charged ions remain. The composition of the sphere and the cavity around builds up a nanoshell particle. The thickness of the nanoshell is so small that both plasmons can interact with each other. In this case there are two possibilities for electron-hole formation, that are illustrated in Figure 2.4 a) with ω_- and ω_+ states. In the first case, the electrons are concentrated on the inner and outer surface of the shell on one side of the particle and the holes on the other side. Thus, both plasmon modes couple symmetrically in a bonding mode. In the other case, electron and holes arrange on the outer and inner surface respectively on one particle side and vice versa on the other side. In this case the two plasmon modes couple anti-symmetrically in an anti-bonding mode denoted with ω_+. The bonding mode is energetically preferred and has a lower resonance frequency. The resonance frequency of these modes depends on the inner a and outer radius b of the shell, and on the order of multipolar enhancement l:

$$\omega_{l\pm}^2 = \frac{\omega_B^2}{2}\left[1 \pm \frac{1}{2l+1}\sqrt{1+4l(l+1)\left(\frac{a}{b}\right)^{2l+1}}\right] \tag{2.27}$$

where $\omega_B = \sqrt{\frac{4\pi e^2 n_0}{m_e}}$ is the solid sphere plasmon resonance. Experimentally the model is supported by measuring the extinction spectrum of a double concentric nanoshell and the

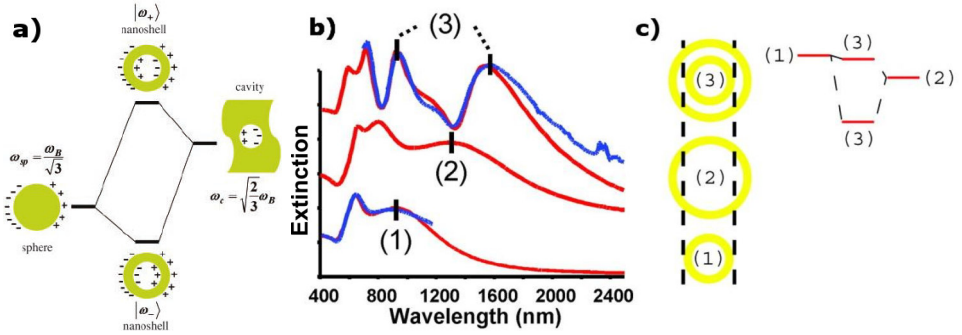

Figure 2.4.: Plasmon hybridisation model of metal nanoshell particles a) and experimental data b). The energy level diagram in c) displays energy relation of the supported plasmon modes for two fundamental sample geometries, a sphere, and a cavity formed by the surrounding material together with the two supported resulting modes in a nanoshell composed of the cavity and the spherical particle with symmetrical bonding and anti-symmetrical anti-bonding plasmon coupling. The model is supported with experimental (blue) and simulated data (red). The extinction spectra exhibit features from a concentric double nanoshell particle (3) and the two fundamental nanoshell particles (1) and (2). From [48]. Reprinted with permission from AAAS.

two fundamental nanoshell particles. For this sample geometry there are four energy levels exisiting. Each shell supports the bonding ω_- and anti-bonding mode ω_+. For the composed double nanoshell the modes are combined to ω_{--}, ω_{+-}, ω_{-+}, and ω_{++}. In the measured spectra in Figure 2.4 for the double nanoshell particle the ω_{--} and ω_{+-} resonances are clearly visible. With the model of hybridization it is possible to describe also other sample geometries such as nanorice particles [49], nanostars [50], or nanostructures composed of different materials like nano-sandwiches [51, 52].

Dmitriev et al. studied experimentally and with simulations the tunability of hybridization of gold-silica-gold nanosandwiches [52]. In these structures the electric field is aligned vertically in the surface plane, which is a requirement for the investigation of the electric field with attosecond streaking (described in Section 3.7.3). By controlling the thickness of the silica spacing layer or the aspect ratio of the top gold layer the coupling of the dipole orientations can be controlled. In Figure 2.5 the results for the variation of the spacing layer thickness are presented. The disk sandwich is composed from two $10\,\mathrm{nm}$ gold disks separated by a silica layer with variable thickness from $5\,\mathrm{nm}$ to $32\,\mathrm{nm}$. The diameter of the sandwich top disk varies for manufacturing reasons from $108\,\mathrm{nm}$ to $64\,\mathrm{nm}$ with increasing silica layer thickness. The lower disk has a diameter of $108\,\mathrm{nm}$. In a) a series of extinction spectra for the varying spacing layer thickness are shown together with the spectra for a single gold disk (blue curve) and a gold disk with the double thickness of the bottom gold disk (red curve). For a very thin spacing layer there is only one resonance located at the same frequency as the double layer gold disk at approximately $700\,\mathrm{nm}$. With increasing

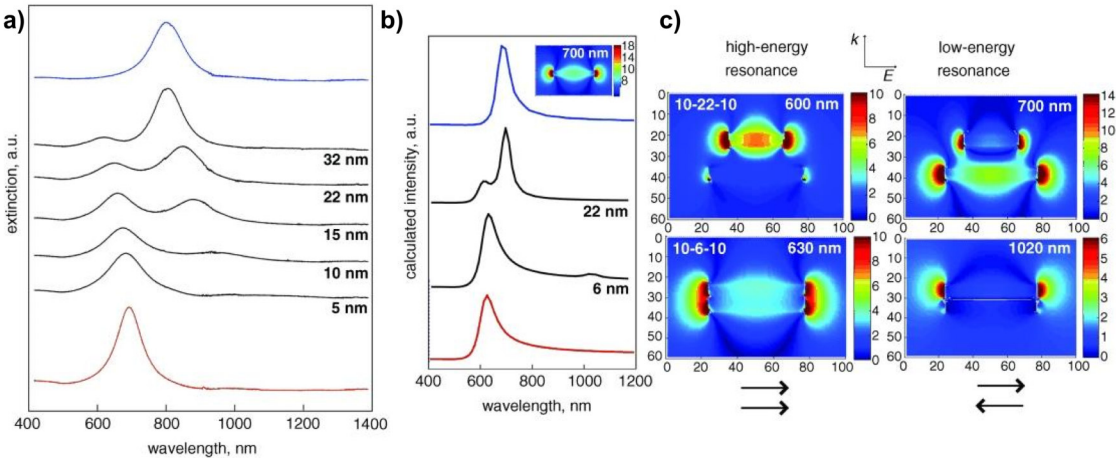

Figure 2.5.: Hybridisation of gold silica gold nanosandwiches. a) shows experimental extinction spectra of sandwiches with different spacing layer thickness together with a single disks of $10\,\mathrm{nm}$ (blue) and $20\,\mathrm{nm}$ (red). In b) and c) calculations of the extinction spectra and the electric near field in the resonances are presented. [52]

spacing layer thickness a second resonance appears and shifts from the low energy range to the position of the single disk resonance around $800\,\mathrm{nm}$. At the same time the intensity of the high energy resonance decreases. In the extreme case of a very thick spacing layer the sandwich behaves like a single gold disk. For a very thin layer, the sandwich appears to behave like a single gold disk with double thickness. Numerical calculations have a similar behaviour in b). More interesting are the simulations of the electric fields in c). The electric fields are calculated and the cross sections are plotted for a thick and thin spacing layer in top and bottom position, respectively, for the two resonance wavelengths. The disk with the thin spacing layer features a strong high energy resonance with the dipoles aligned parallel, whereas the disk with a thick spacing layer supports a strong low energy resonance where the dipoles are aligned anti-parallel.

2.8. Inter- and intraband plasmons

Plasmons occur not necessarily only in the conduction band on surfaces, also electronic oscillations between two energy bands can be excited. In intraband plasmons the electronic oscillation appears inside one energy band, e.g. the conduction band, whereas in interband plasmons electrons are moving between different energy bands. The resonance frequency of inter- and intraband depends on the conduction band electron density [53]. A low electron density with a high energy resonance is attributed to a longitudinal interband plasmons and the low energy resonance to intraband plasmons of the conduction band electrons. As the conduction electron density increases the intraband plasmon energy increases and even may take over the interband plasmon energy. At a certain conduction electron density both inter-

and intraband plasmons equalize. In this situation hybridisation occurs and both plasmons interfere. In Figure 2.6 the rise of a low energy resonance attributed to a conduction band intraband plasmon is studied by manipulating the conduction electron density. This is done by reducing tungsten trioxide to tungsten. The energy loss refers to the energy transferred

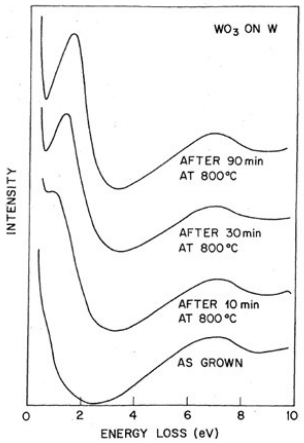

Figure 2.6.: Development of inter- and intraband plasmons in tungsten trioxide during the reduction to elementary tungsten by heating. The heating time and duration is noted next to the spectrum. Reprinted figure with permission from [53]. Copyright (1978) by the American Physical Society.

into the material. During the reduction of tungsten trioxide to tungsten the number of free conduction electrons is increased. The electrons involved in the binding to oxygen can now contribute to the conduction band. Therefore, the probability of driving an oscillation in the conduction band rises and a resonance peak in the energy loss spectrum is pronounced.

Sturm et al. investigated the influence of the band-structure on collective states in simple metals. They explain that a weak crystal potential modifies the dielectric function in two ways [54]. First, a plasmon can decay due to real interband transitions with small shifts resulting from virtual interband transitions. Second, the electron density is modulated by the Bloch character of single electron states. The latter depicts a collective mode called zone boundary collective state [55]. Zone-boundary collective states were found in lithium, natrium and aluminum that depend strongly, in contrast to plasmons, on the symmetry and on the crystal potential.

Schiffrin et al. and *Schultze et al.* report on current inducing and control in dielectrics by an external optical field [56, 57]. Applying the strong electric field of an ultrashort laser pulse to a dielectric leads to a splitting of the valence and conduction band states. At a certain field strength the both fans come close to intersect where anticrossings appear. This means below the critical field strength the valence band state is energetically preferred, and above the former conducting band state. The excitaton with a NIR laser pulse however populates also states in new valence band leading to a current in the dielectric.

2.9. Preparation and characterisation of nanoparticles

2.9.1. Preparation

Thin film samples

The preparation of surfaces by evaporation is well studied in surface science. Different techniques are used to grow thin films with only one or a few monolayers up to several $10\,\mathrm{nm}$. One can differentiate between chemical or physical processes.

Chemical methods are chemical vapour deposition (CVD) [58] and atomic layer deposition (ALD) [59]. Both processes use gaseous precursors of the deposited element. In the case of CVD the precursors are evaporated by heating and transported by a streaming gas (e.g. argon). The reactants are adsorbed at the sample surface where the chemical reaction starts. Non-reacting atoms or molecules are diffusing with the streaming gas. With the right parameters (e.g. temperature of the precursors, gas flow, sample temperature, interaction lengths) only the desired material is deposited on the substrate. ALD is a similar technique to CVD, but the precursors are introduced into the process consecutively. The process is self-limited due to the defined amount of reactants. For growing more than one of the defined layer, the process is repeated cyclically.

A physical preparation scheme for thin film preparation is sputtering. In this technique the target is bombarded with high energy ions (often heavy rare gases like argon) and the atoms are transferred into gas phase. Thereafter, the ejected atoms are condensed on a substrate leading to thin film growth. The film thickness and quality depends on the distance between the sputter target and the sample, from the sputter current, and density distribution in space.

Another physical technique is electron beam evaporation. Here an electron gun produces a high energy electron beam that heats a target material via inelastic collisions and it is evaporated. The evaporated material can then deposit on the sample substrate.

Nanostructured samples

For nanostructured samples one has to distinguish between nanostructuring a thin film, such as bow-tie or rectangular antenna structures, or depositing nanoparticles that are chemically or physically grown in solution.

In the first case, one can either write the structures directly into the thin film with a focused ion beam (FIB) [60] or produce the structures lithographically with a mask and subsequent depositing the material. The FIB produces ions (often gallium), that are accelerated to several keV and focused to the sample surface with electrostatic lenses. On the sample surface the ion beam knocks out atoms or ions. By steering the ion beam, two dimensional structures can be milled into the film. By applying a variable tilt of the surface also three dimensional structures can be produced. The minimum feature size of FIB writing is in the order of $10\,\mathrm{nm}$.

Another technique is electron beam (e-beam) lithography [61], where an electron sensitive resist is deposited before the thin film deposition, is manipulated with an electron beam. After exposure, the resist has another solubility and can be removed with the right solvent only in the exposed area. The produced mask is filled up to the desired structure thickness

with the sample material by thin film deposition. Finally, the resist is removed with another solvent together with the covering film. Only material in direct contact to the substrate remains.

The second case is the deposition of nanoparticles from solution. These nanoparticles can be synthesized physically or chemically, e.g. by laser ablation, evaporation-condensation, or chemical reduction. The deluted particles can be deposited with different coating techniques as spin-coating, dip-coating, or by evaporation of the solvent. For spin-coating the substrate is rotated with a high frequency. The nanoparticle solution is dropped on the substrate and dispersed due to rotation. The solvent evaporates and the particles remain on the substrate. Dip-coating uses the surface tension of the solvent. A substrate is positioned in the nanoparticle solution and then slowly pulled out under a certain angle. The surface tension drains the solvent back into the reservoir. The process parameters in both coating techniques are concentration of the nanoparticle solution, the solvent itself, rotational or pulling speed, and in the case of dip-coating the pulling angle. Simple evaporation of the nanoparticle solution does not require specific technique but the results are often not reproducible.

The contamination of surfaces can influence measurements or even make them impossible. Standard surface science cleaning techniques are sputtering or heating, where the sample surface is cleaned by electron or ion bombardment or evaporation of the contaminants, respectively. Unfortunately, these techniques are not suitable for nanostructured surfaces. The bombardment with electrons does not only remove contaminants but also the sample material and destructs the sample structures. Heating itself is a surface preserving technique, if the heating temperature is much smaller than the melting temperature. Nanostructures however have much lower melting temperatures than the evaporation temperature of typical surface contaminants. Therefore, cleaning with ultraviolet (UV) light and ozone is used [62]. UV light cracks the bondings of organic contaminants and simultaneously produces highly reactive free O^*-ions from Ozone. After reacting with the cracked contaminants, volatile molecules and a hydrophilic surface are produced. A demonstration of a UV-ozone cleaning procedure is presented in Section 5.6.

2.9.2. Characterisation

Darkfield microscopy and spectroscopy

The scattering spectrum of a nanoparticle is characteristic for its size, shape, and material. Therefore, dark field microscopy and spectroscopy became an established technique to observe single-particle plasmonic features [38, 63]. Darkfield microscopy, in contrast to standard microscopy, collects only the scattered light and is therefore not sensitive to the transmitted or directly reflected light. The scattered light spectrum is of interest for the investigation of the plasmon resonance. To combine a spectroscopic measurement with darkfield microscopy a standard microscope can be modified with a beam splitter where a part of the beam is sent into a spectrometre. The selective investigation of single nanoparticles is oftendesired. Therefore, a liquid crystal display (LCD) can be used to control the transmitting sections pixelwise. A setup for a darkfield microscope with an additional spectrometer is illustrated in Figure 2.7. In standard operation, the sample is illuminated from the side to guarantee that

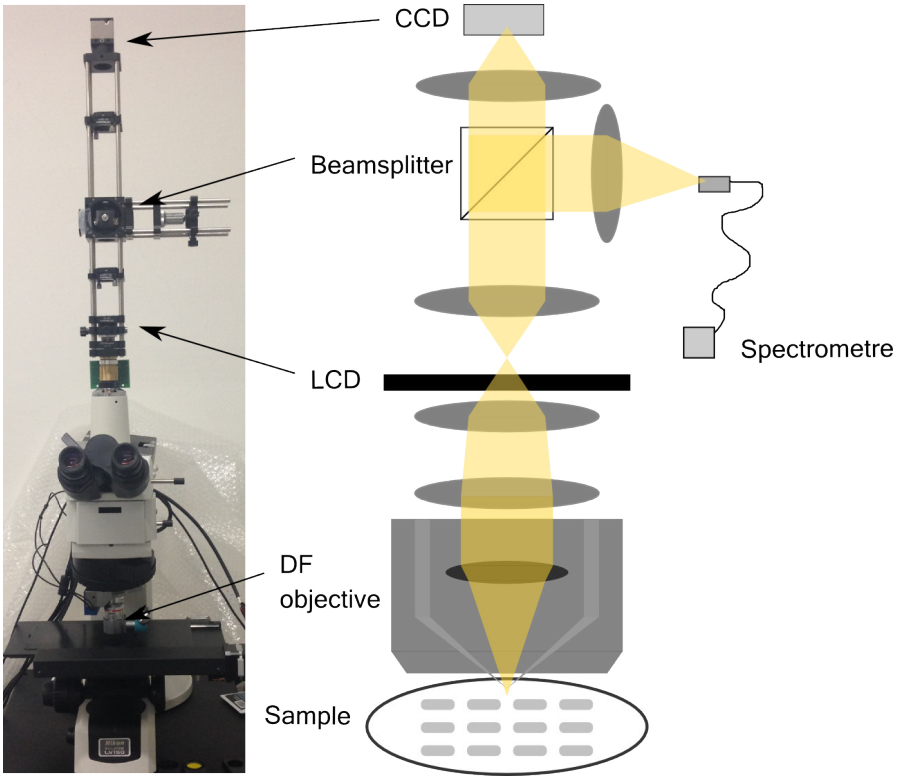

Figure 2.7.: Setup combining darkfield microscopy and spectroscopy with a selective field of view

only scattered light is collected with the objective. Specific darkfield objectives allow the illumination of the sample in a ring-like light path around the central aperture. The scattered light is collected through the central aperture. The LCD is positioned slightly off from the intermediate image plane and via a software nanoparticles of interest can be selected for spectroscopy and imaging . Behind the LCD the beam is split in two parts. The transmitted beam is collected with a colour sensitive CCD camera for the darkfield image. The reflected beam is focused into an optical fibre guiding the light to a spectrometre. This apparatus allows space selective spectroscopy.

X-ray photoelectron spectroscopy

X-ray photo electron spectroscopy (XPS) [64] is the working horse in surface science. It is used to investigate the chemical composition of the sample. It allows the analysis of materials on the sample surface and one can identify elementary materials, chemical bondings, oxidation states, and surface contamination. The X-ray penetration depth is on the order of ($1\,\mu\mathrm{m}$ to $10\,\mu\mathrm{m}$) but the limiting factor is the mean free path of photoelectrons in the order of few ten Angström [65]. Electrons generated deeper undergo energy losses and produce a background in the measured spectrum. The specific binding energy E_b of photoelectrons is

determined by measuring the photoelectrons kinetic energy E_{kin}:

$$E_{kin} = h\nu - E_b - \Phi_S \tag{2.28}$$

where Φ_S the resulting total working function. Depending on the material and oxidation state characteristic binding energies and peak shifts are observed.

In the analysis of photoelectron spectra it is important to separate between different physical phenomena. The spectral lines originate from the photoelectrons and Auger electrons. Also satellite peaks occur from spin-orbit coupling of the X-ray source material ($K\alpha$ line has satellites α_1 up to α_6). Other lines are X-ray ghosts, shake-ups, or multiplet splitting. The line identification starts with carbon and oxygen peaks ($C\,1s$, $O\,1s$) that are usually present in any spectrum. Then other intense lines are identified from the known sample materials. Chemical states are identified from the shifts relative to the elementary lines. For a quantitative analysis peak areas are compared. The background correction is very important. Several background types exist (linear, Shirley, Tougaard background,...). The linear background is simply a straight line and the easiest one. The Shirley background is scaled to the total number of photoelectrons at lower binding energies relative to the position. The Tougaard background takes losses into account from higher kinetic (lower binding) energy electrons that undergo losses. This processes happen arbitrarily and a background is formed.

X-ray diffraction

X-ray diffraction (XRD) [66]allows the characterisation of the crystal structure [67]. In a periodic crystal structure waves are diffracted depending on the wavelength λ, the distance between the lattice planes d, and the angle of incidence θ according to Bragg's law:

$$2d\sin\theta = n\lambda \tag{2.29}$$

In XRD the incidence angle of a monochromatic X-ray beam is scanned and the reflected intensity is measured in a $\theta - 2\theta$ setup. When the incidence angle approaches constructive interference of the diffracted beam the signal increases. Depending on the crystalline structure one can identify peaks of a distinct crystal orientation and its multiples (e.g. (110), (220),...) for a single crystal or peaks from multiple crystal orientations (e.g. (100), (110), (111) , ...). In the case of amorphous samples no peaks appear. The broadening of the peaks indicates the long range order quality of the crystal structure. A polycrystalline sample with a single crystalline zones, which are not regularly, has a broad peak, whereas one extended crystalline structure results in a very sharp peak.

X-ray reflectivity

With X-ray reflectivity the thickness of thin films or multilayers can be characterised [68]. Therefore, an X-ray beam is reflected from the sample with grazing incidence and the intensity of the reflected beam is measured. For a non-perfect surface quality the reflectivity $R(Q)$ differs from the ideal Fresnel reflection $R_F(Q)$ [69]:

$$\frac{R(Q)}{R_F(Q)} = \left| \frac{1}{\rho_\infty} \int_{-\infty}^{\infty} \exp(iQz)(\frac{d\rho_e}{dz})dz \right| \tag{2.30}$$

with $Q = 4\pi \sin\theta/\lambda$, the angle of incidence θ, the X-ray wavelength λ, the electron density ρ_e, material density below the surface ρ_∞, and the depth z. By fitting this formula to experimental data, one can deduce the electron density profile and therefore the film layer thickness.

Imaging techniques for nanostructures

Standard optical imaging of small particles is limited by diffraction. It depends on the numerical aperture of the microscope objective and the wavelength of the light. Therefore, the resolution is limited to structure sizes of about half of the wavelength. For investigating plasmonic nanoparticles with resonances in the visible spectrum the optical resolution is not sufficient. Modern imaging techniques like scanning electron microscopy (SEM) [70], atomic force microscopy (AFM), or scanning tunneling microscopy (STM) [71] enable spatial resolution down to the atomic scale. In SEM the sample is scanned with a high-energetic electron beam under vacuum conditions. On the sample surface the primary beam excites secondary electrons that are detected. Only secondary electrons originating from the topmost layers down to approximately a few nanometres are detected. The lateral resolution of SEM is in the order of a few nanometers but it does not give a height profile. The samples have to be conductive or need a conductive top layer, otherwise the sample is charged and further generation of secondary electrons is prohibited. For analysing samples with a resolution down to the atomic scale with topographic height information AFM/STM is used. The measurement principle of AFM is to scan a sample with a tip on a cantilever. When the tip approaches the sample surface, electrostatic, van der Waals, and chemical bonding forces lead to a bending of the cantilever. By measuring this bending with a laser beam that is reflected from the cantilever while scanning the substrate, it is possible to reconstruct an image of the surface and surface forces. In principle an AFM can operate under ambient conditions. An AFM can operate in contact, non-contact, and tapping mode. The best resolution down to the atomic scale is reached in non-contact mode under UHV conditions because of the missing water film on the surface and no contaminations.

A scanning near-field optical microscope (SNOM) is based on the working principle of an AFM but the forces interacting with the tip are near field forces from the sample [72]. The tip is illuminated with a laser beam and plasmons are excited. The plasmonic field has its maximum at the tip and is used to excite the sample resulting in stimulated light emission. The sample is raster-scanned and the optical and distance signal are measured. The map that is created contains optical information of the surface as well as topographic information. Especially for the investigation of plasmonic structures a SNOM delivers valuable information because one receives the spatially resolved optical response of the system.

Photoelectron-emission microscope

The photoelectron-emission microscope (PEEM) is a raster scan technique to probe the photoemission of plasmonic samples spatially with nanometre and temporally with attosecond resolution [73]. The technique is based on the attosecond streaking technology explained in Section 3.7.3. Photoelectrons are generated with an attosecond light pulse. A temporally

delayed NIR laser pulse excites a plasmon. The photoelectrons experience the electric field from the plasmon leading to a acceleration or deceleration. By detecting the kinetic energy of the photoelectrons for many time-delays, the electric field of the plasmon is obtained. In PEEM the sample is additionally raster scanned for generating a full map of the sample surface. However, this technique has difficulties. One problem is, that in this configuration one cannot distinguish between the laser and the plasmonic field. The assumption is, that the electric light field is short compared to the plasmonic field, and the plasmonic field is enhanced with respect to the light field, such that the contribution of the light field to the total field is low. Another difficulty is the long exposure times for raster-scanning the sample. Nanoplasmonic structures have a limited lifetime since thermal self-destruction leads to local melting.

3. Attosecond physics

3.1. General

The invention of the laser in 1960 by *Maiman* had a huge impact on technology. Lasers can be found in everyday devices like bar-code scanners in the supermarket, laser pointers, optical storages (CD, DVD, blue-ray discs), in medical equipment like laser scalpels, pulse measurement devices, cutting or welding devices, distance measurement devices, and micro- and nanostructuring. Without the invention of lasers modern physics such as the investigation of phenomena at ultrashort time scales reaching the attosecond region would not have been possible. The basic concepts of lasers like light quantisation and stimulated emission have already been studied by *Max Planck* and *Albert Einstein* in the beginning of the 20th century [74]. The benefit of lasers are the coherent and monochromatic emission of light with low divergence. Lasers consists basically of an optical medium emitting the light, a pump source transferring energy into the optical medium and a cavity selecting the photons with the proper energy and moment. We distinguish between continuous-wave (cw) lasers and pulsed lasers. For pulsed lasers, depending on the deserved pulse duration, different schemes are used. Switching the pump source enables pulse repetition rates up to $1\,\mathrm{kHz}$ with pulse durations down to $100\,\mathrm{ns}$ in CO_2 lasers. In this so called Q-switching technique the resonator losses from spontaneous emission are controlled by an attenuator and kept high as long as the active medium gained enough energy. Then the attenuator is switched off and the process of stimulated emission is started. With this technique a repetition rate of several MHz can be achieved with a pulse duration below $1\,\mathrm{ns}$ and peak powers up to GW. For the generation of laser pulses down to few femtosecond pulse duration the scheme of mode locking is applied which is explained in the following section. *Strickland and Mourou* invented the chirped pulse amplification scheme [23]. This scheme is state of the art until today for the generation of femtosecond pulses down to few ten femtoseconds with milli-joule pulse energy and used in a huge number of laser systems. A detailed introduction in the technology of femtosecond lasers and ultrashort laser pulse phenoma is given by *Rulliere* [74] and *Diels* [75]. In this case the temporal duration of the light pulses is connected with the spectral broadness. To reach even shorter light pulses nonlinear high harmonic generation (HHG) is needed. The shortest pulse generated so far has a pulse duration of $67\,\mathrm{as}$ [30].

3.2. Generation of ultrashort laser pulses

Hirlimann derives the formation of light pulse from "Gedanken" light pulses [74] by multiplying the electric field of a continuous light wave with the bell-shaped Gaussian function:

$$\mathbf{E}(t) = \mathbf{E}_0 \exp\left(-t^2/\tau^2 + i\omega_0 t)\right) \tag{3.1}$$

where τ is the pulse duration and ω_0 the central frequency. The spectrum of the light pulse can be calculated by the Fourier transformation and results also in a Gaussian function:

$$\mathbf{E}(\omega) = \exp(\frac{-(\omega-\omega_0)^2}{4\Gamma} \tag{3.2}$$

To determine the exact relationship between pulse duration and spectral width of the laser pulse one can start from the general time and frequency Fourier transformation:

$$E(t) = \frac{1}{\sqrt{2\pi}} \int_{-\infty}^{\infty} E(\omega) \exp(-i\omega t) d\omega \tag{3.3}$$

$$E(\omega) = \frac{1}{\sqrt{2\pi}} \int_{-\infty}^{\infty} E(t) \exp(i\omega t) dt \tag{3.4}$$

The pulse duration τ and the frequency width $\delta\nu$ are experimentally easily accessible at full width at half-maximum (FWHM) and related with the time-bandwidth product:

$$\Delta\nu \cdot \tau \ \geq K \tag{3.5}$$

The parameter K is determined by the pulse shape, e.g. Gaussian $K = 0.441$, exponential $K = 0.140$ or Lorentzian $K = 0.142$. For the generation of ultrashort laser pulses this bears several consequences. The shortest pulse can only be achieved with a Gaussian envelope and is called Fourier limited. The pulse duration depends on the spectral bandwidth, which covers the whole visible spectrum for a few femtosecond (fs) pulse. These pulses are necessarily not monochromatic anymore. Further more the transform-limited pulse requires a symmetrical spectrum with a linear time dependence of the phase ($\omega = \omega(t) = \frac{\partial\Phi}{\partial t} = \omega_0$) where the angular frequency ω equals the central angular frequency ω_0 in time domain. For higher orders it is beneficial to re-write Equation 3.3 and include the spectral phase $\phi(\omega)$:

$$E(t) = \frac{1}{\sqrt{2\pi}} \int_{-\infty}^{\infty} E(\omega) \exp(-i\omega(t)t) \exp(i\phi(\omega)) d\omega \tag{3.6}$$

The phase can be expressed as a Taylor expansion:

$$\phi(\omega) = \phi(\omega_0) + \phi'(\omega_0)(\omega-\omega_0) + \frac{1}{2}\phi''(\omega_0)(\omega-\omega_0)^2 + \frac{1}{6}\phi'''(\omega_0)(\omega-\omega_0)^3 + ... \tag{3.7}$$

The first term $\phi(\omega_0) = \Delta\phi$ describes the carrier envelope phase (CEP) which is the phase of the maximum of the electric field relative to the maximum of the envelope. The second term is called group delay and shifts the pulse in time. Both terms do not influence the pulse form, but the third term, the group velocity dispersion (GVD) does. The GVD results in a so called chirp, meaning that the lower frequencies are shifted to the leading part of the pulse and the higher to the tailing part, or the other way around. This effects a symmetrical broadening of the laser pulse. The higher orders lead to asymmetric broadening and the creation of pre- and post pulses. The influence of the CEP and the chirp are illustrated in Figure 3.1. On the left the electric field of a cosine (blue line) and a sine (magenta line) pulse are plotted. The envelope (dashed lines) and the intensity (shaded) are the same for both

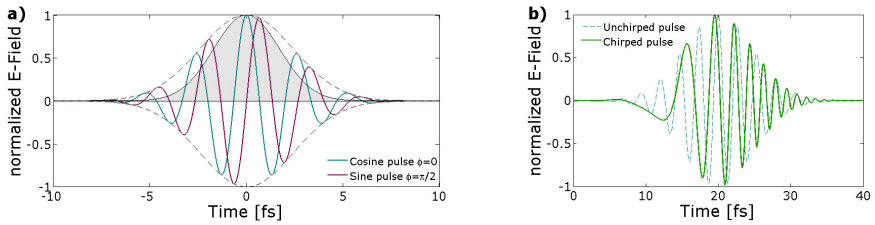

Figure 3.1.: Influence of the CEP a) and the chirp b) to the form of the electric field in a few-cycle laser puls.

pulses. The cosine pulse is symmetrical relative to the maximum of the envelope, whereas the sine pulse is anti-symmetrical. The maximum field intensity is reached only in the cosine pulse. On the right a chirped pulse is plotted (solid line) in comparison to a non-chirped pulse (dashed line) with the lower frequencies coming earlier than the higher frequencies. In the non-chirped pulse the zero-crossings are equidistant. Whereas, the zero-crossings of the chirped pulse are compressed or expanded over time.

Another requirement for the generation of ultrashort laser pulses is a fixed relation of the spectral components. A light bulb as white-light source never creates ultrashort pulses since the waves do not have the right phase relation. This is achieved with mode-locking and is demonstrated in Figure 3.2. It is based on the constructive interference of spectrally equidistant resonator modes at one position inside the cavity. The main challenge is to

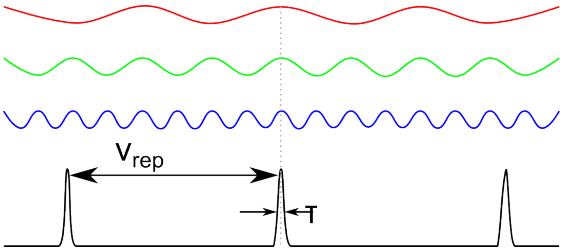

Figure 3.2.: Principle of Mode-locking where the phases of single monochromatic waves are related such that they interference constructively with the creation of a short pulse.

control the group- and phase-velocity dispersion in the cavity. Subsequent pulses with a repetition rate ν_{rep} undergo a shift of their CEP $\Delta\phi$, if the dispersion is non-zero. This results in a frequency offset ν_{CEO} influencing also the subsequent mode frequencies ν_m :

$$\nu_{CEO} = \frac{\Delta\phi}{2\pi}\nu_{rep} \qquad \nu_m = \nu_{CEO} + m\nu_{rep} \tag{3.8}$$

where m is the number of modes.

Kerr lens mode-locking is the predominant method for the generation of few-cycle laser pulses [76]. The non-linear Kerr lens effect describes the intensity dependence of the refractive index of a medium: $n(I) = n_0 + n_2 I$. n_0 represents the linear index of refraction

that is used at low light intensities in classical optics. n_2 represents the first order intensity dependent refractive index. A positive n_2 at a high intensity leads to a stronger refraction. For a Gaussian beam, where the intensity is not constant over the spatial beam profile, this results in a stronger refraction in the center than in the outer part and thus to self focussing of the beam. For the mode-locking principle this means that the intense maxima are stronger focused and suffer less from cavity losses than weaker maxima. Therefore, only the intense modes survive and get enhanced. The Kerr lens effect has to be initiated by an intensity fluctuation historically by a percussion nowadays a shaking mirror is typically used [74, 75].

For the generation of few-cycle pulses titanium doped sapphire (Ti:Sapphire) crystals are used as active medium. They have a broad emission from $650\,\mathrm{nm}$ to $1100\,\mathrm{nm}$.

The source of ultra-short laser pulses as described above is called oscillator. Typically oscillators generate durations down to $5\,\mathrm{fs}$, with repetition rates of $1\,\mathrm{MHz}$ to $100\,\mathrm{MHz}$, and pulse energies of $1\,\mathrm{nJ}$ to $1\,\mu\mathrm{J}$ [77]. However, non-linear or high energy applications require higher intensities (e.g. HHG: few $10^{14}\,\mathrm{W/cm^2}$). Therefore, amplification scheme of oscillator pulses are needed. Problems are the damage of optics due to high intensities and the required electric power, because amplifying a single pulse at a $1\,\mathrm{MHz}$ repetition by a factor of 10 requires 10 million times more energy.

The chirped pulse amplification principle is explained in Figure 3.3 and overcomes both problems by reducing the repetition rate and stretching temporally, amplifying, and compressing the pulse. Behind the oscillator, a stretcher composed of dispersive optical elements

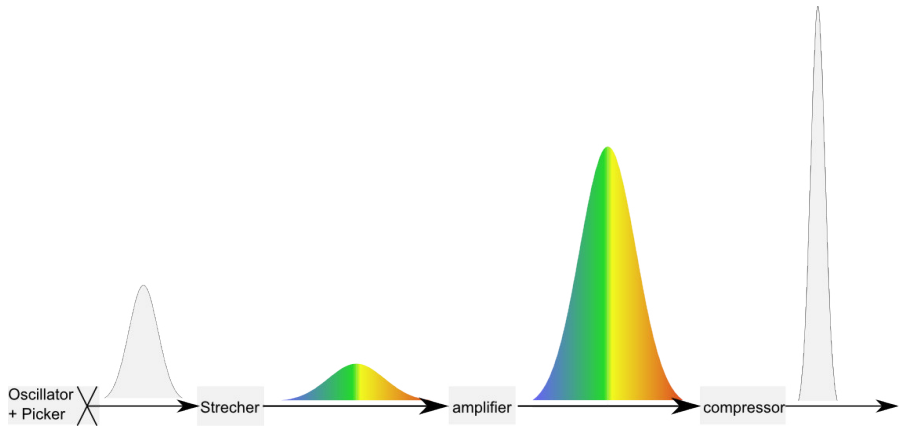

Figure 3.3.: Principle of chirped pulse amplification: A pulse picker reduces the repetition rate of the pulses. Then the pulses are stretched and amplified to much higher pulse energies. After amplification the pulses are compressed with opposite dispersion.

like a block of high dispersive material, chirped mirrors ,or gratings, creates a chirped pulse with a longer pulse duration. In a state-of-the-art CPA there are two amplification steps: a regenerative amplification stage is used for pre-amplification and a multipass. In the technique of regenerative amplification the pulse is trapped inside a resonator and transmitted only after the pulse has gained energy above a certain level. The switch typically is realized with a Pockels cell [78] rotating the light polarization and the pulse can leave the amplifi-

cation stage. Behind the preamplification stage, a pulse picker reduces the repetition rate. The second amplification stage is based on a multipass amplifier. This scheme is based on consecutive passes in a bow-tie like geometry through a single gain medium that is optically pumped. All optical length are designed in a way that the pulse propagates through the crystal synchronized to the pump pulses such that the pulse obtains most energy. Both concepts are illustrated in Figure 3.4. After the pulse is amplified a compressor with opposite

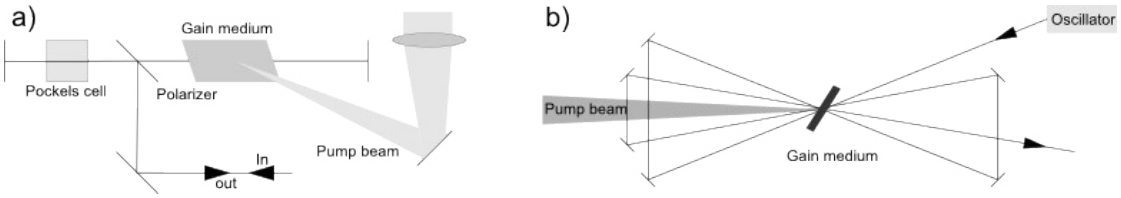

Figure 3.4.: Two concepts for laser pulse amplification used in chirped pulse amplification: a) regenerative amplifier and b) multipass amplifier.

dispersion is used to re-compress the pulses to the Fourier limit.

However, after undergoing the CPA amplification process it is difficult to recover the initial few fs pulse duration of the laser pulses due to gain narrowing [74]. *Nisoli et al.* [79] developed an optical compression technique including spectrally broadening of the pulse propagation through a noble gas filled hollow fibre. In the hollow fibre compressor a glass capillary is filled with a noble gas [80]. In the gas non-linear self-phase modulation occurs due to self-phase modulation with subsequent temporal compression with a quartz glass prism pair. If the intensity exceeds the threshold for the Kerr lens effect, the intensity dependent refractive index leads to an intensity dependent phase velocity. Therefore, the original frequency gets shifted by:

$$\omega(t) = \omega_0 + \Delta\omega(t) \qquad \text{with } \Delta\omega(t) = \frac{d\phi(t)}{dt} \tag{3.9}$$

with the shift of the instantaneous frequency $\Delta\omega$ and the phase ϕ.

The maximum phase shift is connected to the effective length L_{eff} of the nonlinear medium by:

$$\phi_{max} = n_2 \frac{\omega_0}{cA_{eff}} P_0 L_{eff} \tag{3.10}$$

with the nonlinear refractive index n_2, the pulse peak power P_0, and the effective mode area A_{eff} [81]. The effective length is calculated from the B-integral that describes the total spectral broadening [82]:

$$B = \frac{2\pi}{\lambda} \int_0^L n_2(z) I(z) dz = \frac{2\pi}{\lambda} n_2 I L_{eff} \tag{3.11}$$

with the peak intensity I.

A setup of an oscillator, amplifier, and a hollow fibre compressor is nowadays the working horse for high harmonic generation and especially attosecond science.

3.3. CEP control

There exist several techniques for measuring and actively controlling the CEP. One of the most often implemented techniques is the f-2f-interferometer proposed by *Telle et al.* [83]. The f-2f-interferometer is based on the metrology ability of a frequency comb by *Hänsch* [84] for which he received the Nobel prize in 2005. In this scheme the octave spanning laser pulse (or broadened to octave spanning by white light generation) is frequency doubled with a nonlinear crystal such that the tail of the fundamental spectrum overlaps with the beginning of the frequency doubled spectrum. Both spectra then contain a common spectral region with a high energy mode of the fundamental spectrum $\nu_{2n} = \nu_{CEO} + 2n\nu_{rep}$ and a low energy mode of the frequency doubled spectrum:

$$2\nu_n = 2\nu_{CEO} + 2n\nu_{rep} \tag{3.12}$$

When both modes overlap temporarily and spatially they are interfering with a beat note:

$$\nu_{beat} = 2\nu_n - \nu_{2n} = 2\nu_{CEO} + 2n\nu_{rep} - (\nu_{CEO} + 2n\nu_{rep}) = \nu_{CEO} \tag{3.13}$$

revealing directly the CEP. The beat note signal can be measured with a photodiode as an interference intensity.

The typical optical setup for the f-2f interferometer contains an interferometer where in one arm the laser pulse is frequency doubled [76]. The second arm carrying the fundamental pulse can be time delayed to control the temporal overlap. After recombination of both paths the signal is band pass filtered to detect only the beat note and measured with a photodiode. A more robust setup uses in place of the interferometer a periodically poled Lithium Niobate nonlinear crystal (PPLN crystal). The advantages of the PPLN-setup are that it provides spectral broadening if the pulse spectrum needs broadening to octave spanning, and frequency doubling [85].

Measuring the CEP of amplified laser pulses the detection scheme of the f-2f interferometer has to be adapted. During the amplification process the discrete modes in the spectrum of the oscillator output broaden. The CEP therefore cannot be detected as easily as described above. However, the main setup of the f-2f interferometer remains. To obtain an octave spanning spectrum the laser pulse is broadened by white-light generation. The electric field of the laser pulses after white light generation exhibiting a CEP ϕ_{CEP} is:

$$E_{WLG} = \sqrt{I_{WLG}(\omega)}\exp(i\phi_{WLG}(\omega) + \phi_{CEP}) \tag{3.14}$$

with the spectral phase ϕ_{WLG} added from white light generation and pulse intensity I_{WLG}. The frequency doubled spectrum is generated by focusing in a nonlinear crystal resulting in a pulse:

$$E_{SHG} = \sqrt{I_{SHG}(\omega)}\exp(i\phi_{SHG}(\omega) + 2\phi_{CEP}) \tag{3.15}$$

with the spectral phase ϕ_{SHG} added through white-light generation and pulse intensity I_{SHG}. After the frequency doubling both pulses are time delayed and focused on the detector where they interfere. The output signal at a detector is given by:

$$\begin{aligned} I_{final}(\omega) =& I_{WLG}(\omega) + I_{SHG}(\omega) \\ &+ \sqrt{I_{WLG}(\omega)I_{SHG}(\omega)}\cos\left(\phi_{SHG}(\omega) - \phi_{WLG}(\omega) + \omega\tau + \phi_{CEP}\right)) \end{aligned} \tag{3.16}$$

This signal is detected with a spectrometer. In the overlapping region of the fundamental and the frequency doubled pulse spectral fringes can be found. The frequency of these fringes is proportional to the inverse pulse duration $1/\tau$. The fringes are phase shifted obtaining also ϕ_{CEP} of the laser pulse. The CEP can now be retrieved by performing a Fourier analysis on the interferogram.

A single-shot detection of the CEP is Stereo-ATI [86]. In this method the sensitivity of above threshold ionization (ATI) of atoms to the CEP is used. The experimental setup is demonstrated in Figure 3.5 a). Xenon atoms are ionized in a gas target by a linearly polarized

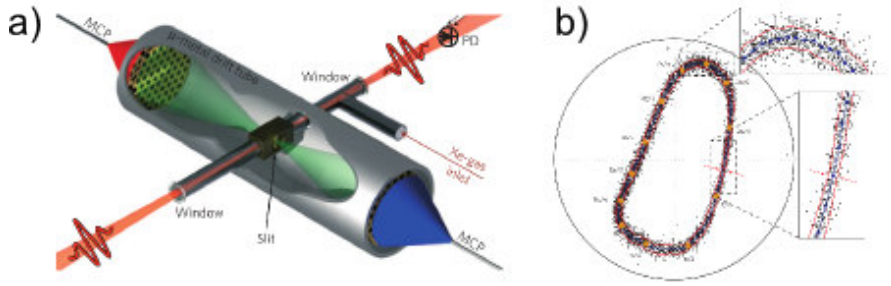

Figure 3.5.: Experimental setup of Stereo-ATI a) shown together with the CEP mapping of a non-stabilized pulse (black dots). Measurement points from stabilized pulses would occupy only a section of the ellipse. Reprinted by permission from Macmillan Publishers Ltd: Nature Physics [87], copyright (2009)

laser beam. The photoelectrons are driven into the direction of the electric field vectors of the laser pulse. The electron kinetic energy is measured on both sides with two time-of-flight spectrometers simultaneously. One can directly obtain the absolute phase by analysing the photoelectrons signal (b) for a non-stabilized pulse in the plane of polarisation).

The advantage of Stereo-ATI to the f-2f-interferometer is the single-shot deduction of the CEP directly from a physical process. The signal extraction is straightforward and needs only electronic processing. The disadvantages is that it requires a vacuum chamber and time-of-flight detection for the measurement of photoelectrons. Nevertheless, also this method is used by many groups for phase tagging and do not stabilize the CEP.

3.4. High harmonic generation

High harmonic generation (HHG) is a non-linear effect appearing when very strong light fields with a few $10^{14}\,\mathrm{W/cm^2}$ interact with a gaseous medium [76]. In the interaction area the strong laser field drives the atomic gas to emit coherent radiation with odd multiples of the driving frequency ω_L:

$$E_{HHG} = n\hbar\omega_L \qquad \text{with } n = 1, 3, 5, ... \tag{3.17}$$

This process cannot be explained by the nuclear Coulomb field destruction or simple multi-photon ionization. Keldysh suggested a tunnel mechanism where the strong electric laser

field suppresses the Coulomb field by bending the atomic potential [88]. In this situation the electron wave packets have a finite probability to tunnel into the continuum and to propagate freely driven by the electric laser field and gain energy. At a certain time the electric field reverses and drives the electron wave packet back to the parent ion. This recollision of the electron wave packet with the parent ion has a finite probability and a photon with the gained kinetic energy is emitted. This model is called semi-classical or three-step model [89] and is illustrated in Fig 3.6.

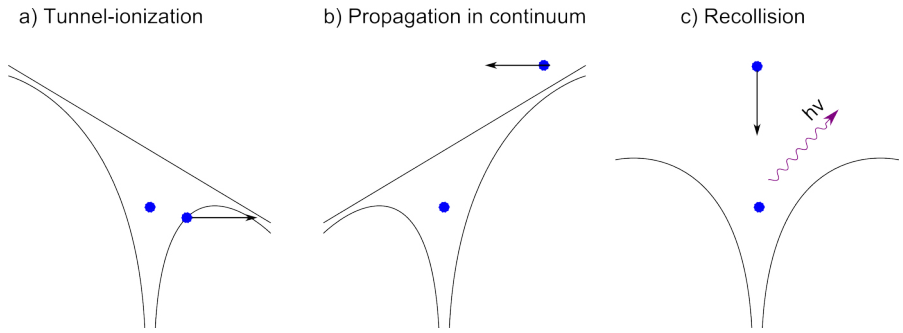

Figure 3.6.: Three step model of tunnel-ionization by P. Corkum: a) bending of the atomic potential such that an electron can tunnel, b) free propagation in the continuum gaining kinetic energy, c) recollision with the parent ion with emission of a higher energetic photon.

Another theory describing the tunnel ionization is the ADK theory of *Ammosov, Delone and Krainov* [90] using the quasi static approximation in the tunnelling regime. Therefore, by using static field ionization rates, also dynamic ionization processes can be modelled [91]. The ionization yield, i.e. the ratio from free electron density $n(t)$ and initial gas density n_0, can be calculated from:

$$\frac{n(t)}{n_0} = 1 - \exp\left(-\int_{-\infty}^{t} w(E(t'))dt'\right) \tag{3.18}$$

with the static field ionization rate w, and the peak electric field strength E of the laser pulse.

The propagation in the continuum supports different electron trajectories leading to earlier or later recollision times with the parent ion [92]. Figure 3.7 illustrates different electron paths returning after short trajectories in the accelerating electric laser field leading to a low kinetic energy and after long trajectories where the electron misses the parent ion in a first attempt but is driven back by the twice reversed field also leading to a low kinetic energy. Electrons with the highest energy gain return to the parent ion after propagation for almost one cycle right before they are decelerated by the reversed electric field. These electrons form the so called cut-off region.

The kinetic energy an electron gains during an average cycle in the electric field E with a carrier frequency ω is given by the ponderomotive potential [93]:

$$U_p = \frac{e^2 < E^2 >}{4m_e\omega^2} \tag{3.19}$$

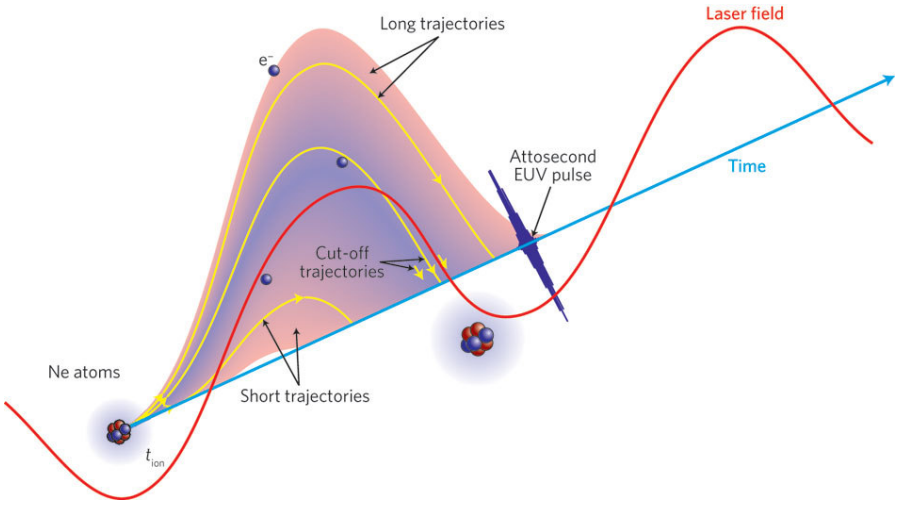

Figure 3.7.: Short and long trajectories in the HHG process with different recollision times. Electrons with a propagation time of almost one cycle of the electric laser field gain the most kinetic energy forming the cut-off region. Reprinted by permission from Macmillan Publishers Ltd: Nature Photonics [92], copyright (2012).

with the electron charge e and mass m_e. The cut-off energy, which is the highest energy an electron can gain, depends on the ionization potential I_p and the ponderomotive potential U_p [94]:

$$E_{cutoff} = 3.17U_p + I_p \tag{3.20}$$

The HHG spectrum has a universal shape illustrated in Figure 3.8 [94]. It shows regular equidistant peaks at odd multiples of the driving laser frequency. For quantum mechanical reasons, only the odd harmonics are emitted. Over the first orders the intensity decreases rapidly (perturbative regime), then a region with a plateau appears, and drops at the cut-off region [76].

The recollision of an electron with the parent ion happens every half-cycle of the electric field resulting in a subsequent emission of high harmonic pulses. Thus, a series of many half-cycles such as in a several $10\,\mathrm{fs}$ pulse results in a pulse train.

Papadogiannis et al. claimed first in 1999 that the high harmonic radiation exhibits features on the attosecond timescale [95]. *Paul et al.* confirmed the temporal structure of attosecond pulse trains by measuring not only the field autocorrelation but also the phase relation of the harmonic components [96]. The pulse train consists of single pulses of $250\,\mathrm{as}$ spaced by $1.35\,\mathrm{fs}$. Therefore, high harmonic generation was proposed to depict a promising light source for attosecond time-resolved experiments.

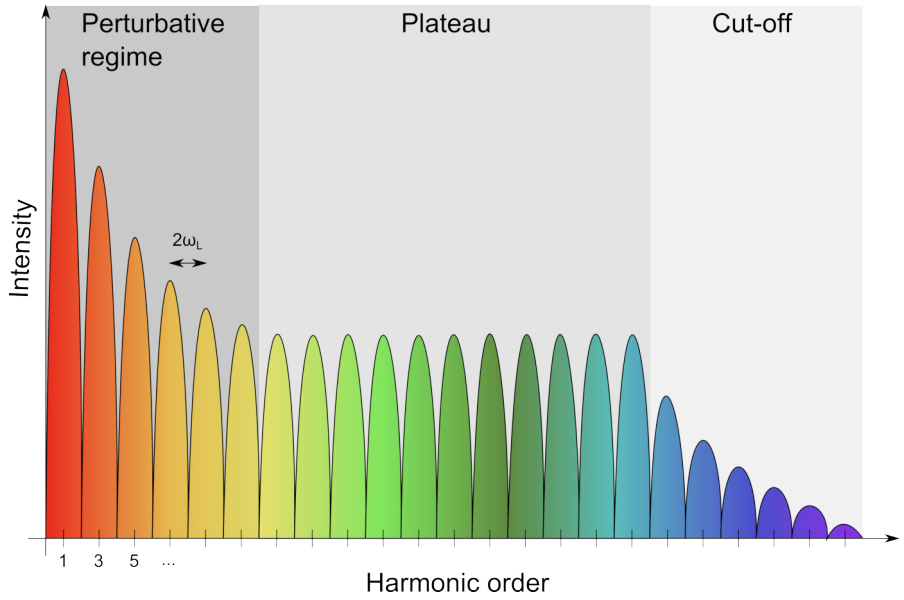

Figure 3.8.: HHG spectrum (left) containing the odd multiples of the driving laser frequency. The spectrum can be divided in three regimes: the perturbative regime, the plateau, and the cut-off region.

3.5. Generation of isolated attosecond pulses

Normally, HHG light pulses form a pulse train of attosecond bursts. However for time-resolved experiments observing dynamics directly in the time domain isolated attosecond pulses are more beneficial. Isolated attosecond pulses can be generated from HHG by various techniques [27, 97]. An overview is given in Figure 3.9. Amplitude and ionization gating are illustrated

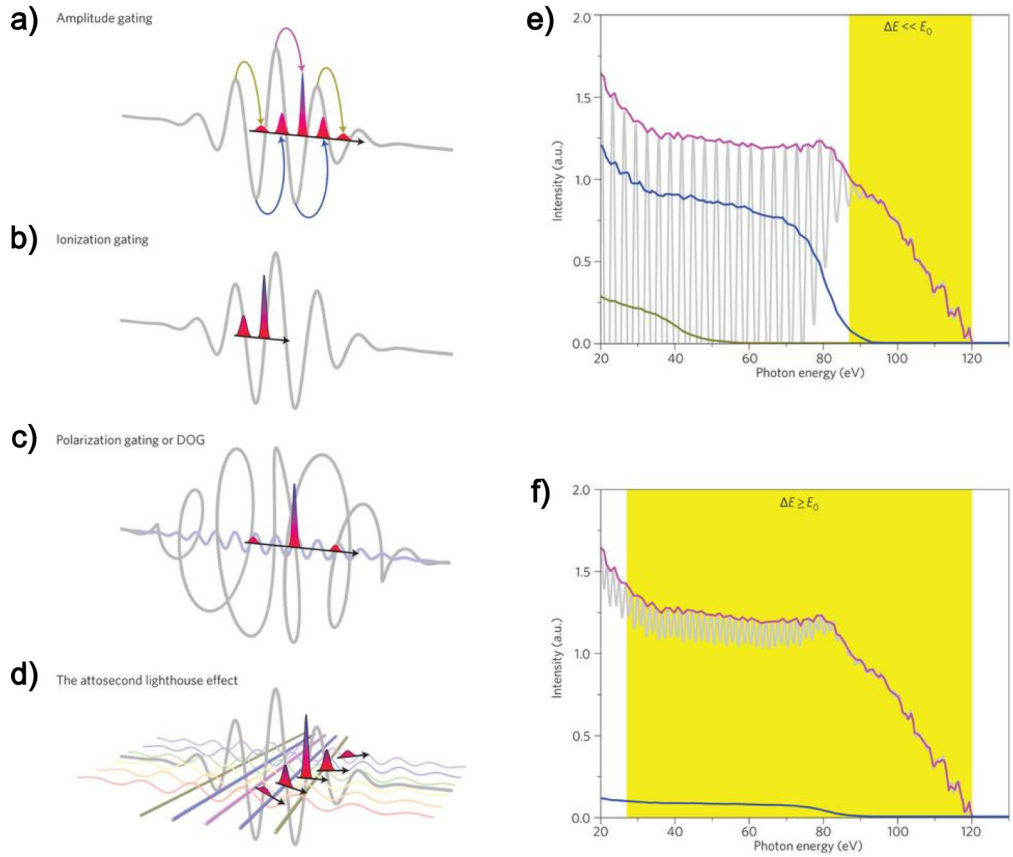

Figure 3.9.: Overview over different attosecond pulse generation schemes: a) amplitude gating, b) ionization gating, c) polarization gating, and d) attosecond lighthouse effect. The corresponding HHG spectra are shown e) for amplitude and ionization gating, and f) for polarization gating and attosecond lighthouse effect. In the case of amplitude and ionization gating only the cut-off region is usable for attosecond pulse generation. The different coloured lines refer to different half-cycle trajectories. Reprinted by permission from Macmillan Publishers Ltd: Nature Photonics [27], copyright (2014).

in a) and b), respectively, and use linearly polarized light to drive the high harmonic process. In amplitude gating the electrons are oscillating in the electric laser field and are driven back at some point after reversing the electric field. There are electrons that return earlier than one cycle of the electric field, and some later. Depending on the returning time the electrons

gain energy with the maximum shortly before one cycle which is defining the cut-off energy. With a spectral filter only the high-energy part of the harmonic radiation is selected for the attosecond pulse generation resulting in an isolated attosecond pulse. This technique is later used in the experiments and described in more detail in Section 3.6. The ionization gating technique uses the complete depletion within the first few half cycles of the driving laser with a careful design of the interaction geometry in terms of gas pressure, position, and thickness of the gas cell [98]. The HHG spectra of the amplitude and ionization gating techniques illustrated in e) look similar.

The techniques of polarization gating (PG), double optical gating (DOG), and attosecond lighthouse effect depicted in c) and d) rely on circularly polarized light. The benefit of these techniques is the broad continuous harmonic spectrum that can be used in its whole bandwidth for the generation of attosecond pulses. Up to now, with DOG the shortest attosecond pulse was produced with a pulse duration of $67\,\mathrm{as}$ [30]. The DOG technique combines PG and two colour gating [99]. The PG technique uses two counter circularly polarized ultrashort light pulses that are slightly delayed such that in a short time window linearly polarized light is created. In this window the process of HHG is driven. The DOG technique adds a weak second harmonic light field to the PG field suppressing every second half cycle of the driving PG field, which enables longer driving pulse durations.

The attosecond lighthouse [100] disperses the incoming laser pulse into its spectral components and then spatially chirps by a tilted wedged glass. Then the dispersed beam is focused into a gas jet such that the high energy edge is located spatially and temporally separated from the low energy wavelength edge in the focus. The high harmonics are generated at different positions along the transverse axis of the beam and propagate angularly and temporally separated delivering a transverse pulse train of attosecond pulses with the highest intensity and photon energy in the center.

3.6. Attosecond pulses by amplitude gating

The generation of attosecond pulses by amplitude gating uses the high energy cut-off region of the harmonic spectrum. The noble gas used for the HHG process defines the maximum cut-off energy by its ponderomotive and ionization potential (3.20). Spectral filtering defines the central frequency and bandwidth of the harmonic beam. An optimization of the cut-off frequency and intensity is therefore mandatory. Figure 3.10 shows the principle of generating an isolated attosecond pulse from high harmonic radiation with two different waveforms.

The cosine waveform of the few-cycle driving laser provides only one half-cycle that is intensive enough to drive the HHG cut-off region to such high photon energies, that an attosecond pulse can be generated as illustrated in Figure 3.10 (a). Whereas, for the sine waveform two half-cycles can contribute and produce two bursts above the relevant photon energy illustrated in (b). In the cosine case, the electron can gain more energy due to the larger amplitude of the electric field which also results in a more trajectories with higher photon energies. This results in a more energetic, more intensive, and smoothly decreasing cut-off region. Spectral filtering as indicated with the dotted curve around $95\,\mathrm{eV}$ cuts out the continuous part of the spectrum. The spectral filtering is experimentally realised with a

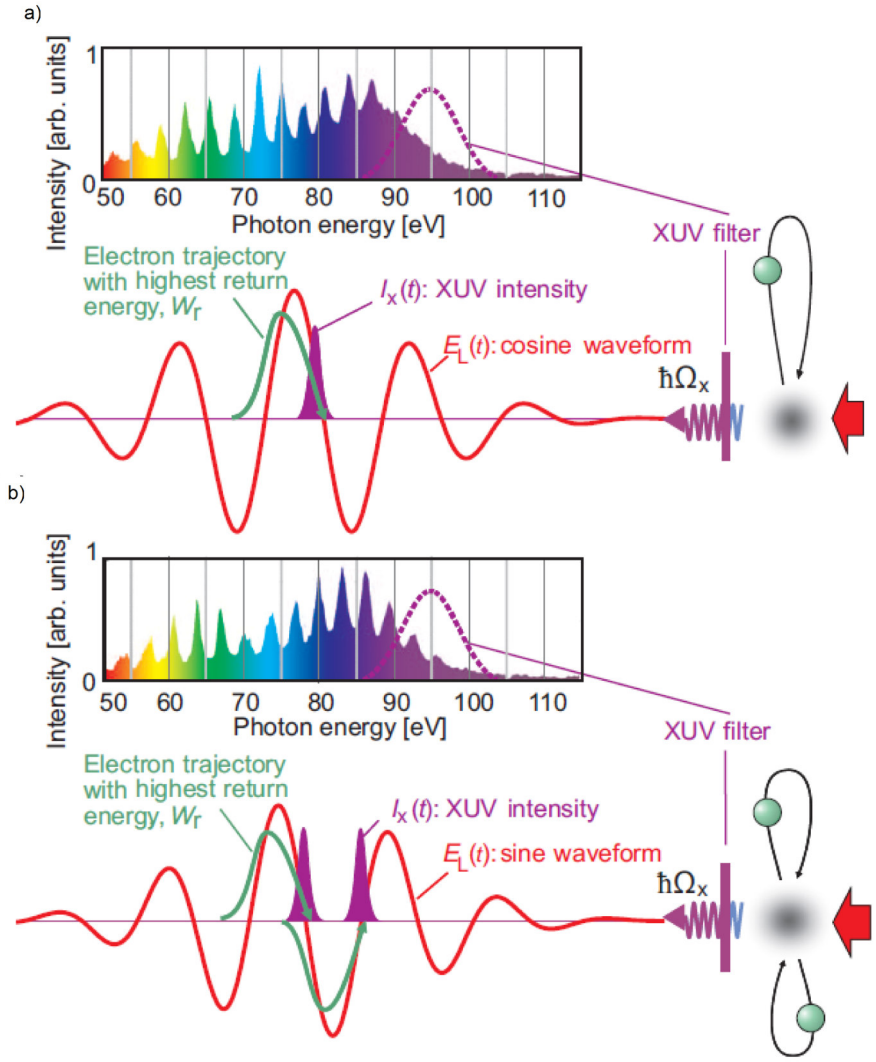

Figure 3.10.: Influence of the CEP to the HHG spectrum generated by a few cycle laser pulse for the generation of isolated attosecond pulses. The cut-off energy depends on the gas used in the HHG process as well. a) A cosine pulse form optimizes the cut-off region to a smoother spectrum. Spectral filtering selects the high energy part of the HHG spectrum which forms the attosecond pulse. b) A sine pulse creates two attosecond puses at lower photon energy. Reprinted figure with permission from [101] Copyright (2009) by the American Physical Society.

multilayer mirror. The multilayer thickness is designed that the peak reflectivity is in the cut-off region and covers its bandwidth. The central wavelength and bandwidth of the multilayer mirror defines the duration of the attosecond pulse with respect to its Fourier transform.

3.7. Photoelectron spectroscopy

3.7.1. Photoelectron transport

A general introduction in photoelectron spectroscopy (PES) is given by *Hüfner* [102]. Photoelectron spectroscopy in solid media differs from gaseous media. The final kinetic energy E_{kin} is given by:

$$E_{kin} = \hbar\omega - \Phi - |E_B| \tag{3.21}$$

with the light frequency ω, the work function Φ, and the binding energy E_B. In a solid the binding energy is referred to the Fermi-energy, which is the highest populated energy level in the ground state system ($E_B = 0$ at E_F). Whereas, in gaseous media the binding energy refers to the vacuum level, which is the energy of a free electron outside any material. The Fermi-level and the vacuum level are related by the work function:

$$\Phi = E_{vac} - E_F \tag{3.22}$$

Important for the investigation of solid samples with PES is the limited information depth. *Tougaard* gives an overview over scattering processes in photoelectron spectroscopy in [103]. Inelastic scattering of photoelectrons from core levels or valence states transfers energy to other electrons. This leads to energy losses of the photoelectrons during transport into vacuum and results in a linewidth broadening. Elastically scattered photoelectrons do not suffer from energy loss but the path length inside the solid becomes longer and therefore leads to a spread in emission times. The inelastic mean free path λ_{IMFP} of a material defines the distance a particle, more specific for this application an electron, propagates inside the material before it scatters elastically or inelastically.

The inelastic mean free path can be calculated using the Tanuma, Powell, and Penn (TPP2) formula [104].

$$\begin{aligned}
\lambda_{IMFP} &= E_{kin}/E_p^2\left[\beta\ln(\gamma E) - (C/E_{kin}) + (D/E_{kin}^2)\right] \\
\beta &= -0.10 + 0.944/(E_p^2 + E_g^2)^{0.5} + 0.069\rho^{0.1} \\
\gamma &= 0.191\rho^{-0.5} \\
C &= 1.97 - 0.91U \\
D &= 53.4 - 20.8U \\
U &= N_V\rho/M = E_p^2/829.4
\end{aligned} \tag{3.23}$$

where E_{kin} denotes the electron kinetic energy, ρ the density, and N_V the number of valence band electrons per atom, M the atomic weight. E_g is the band gap energy for nonconductors, and E_p is the free-electron bulk plasmon energy.

To interpret PES data, the three-step model of PES is useful. It describes the process of photoexcitation, the transport to the surface, and the penetration through the surface as three subsequent steps. An illustration of the model is given in Figure 3.11. The first step describes the photoexcitation of the electron where the photon energy $\hbar\omega$ is transferred to the bound electrons, e.g. valence band electrons, with an energy spread of ΔE_{VB}. The photoelectron energy at this step corresponds to the shifted valence band spread $\Delta E_{VB}+\hbar\omega$.

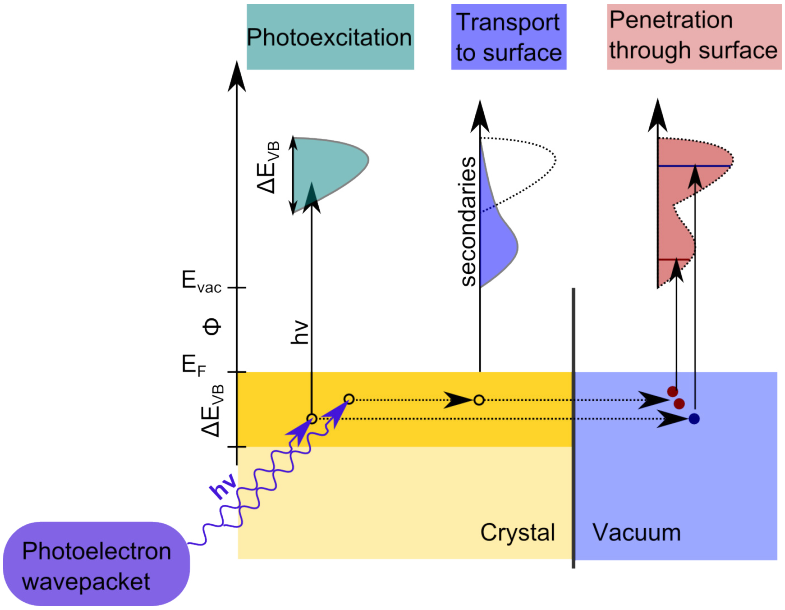

Figure 3.11.: Illustration of the three-step model of photoelectron spectroscopy. Adapted from [102].

The second step covers the transport to the surface where inelastic scattering processes occur, e.g. the creation of electron-hole pairs or plasmons. Within this step, energy is transferred leading to a redistribution to lower energies. Here also secondary electrons are created. The third step treats the penetration through the surface. Only those electrons can propagate into continuum that have enough kinetic energy to overcome the work function. The photoelectron spectrum is therefore determined by the non-scattered electrons having the highest energy, the inelastically scattered electrons at lower energies and secondary electrons that gained enough energy to overcome the work function.

3.7.2. Attosecond streaking in gases

The attosecond streak camera was first reported by *Itatani et al.* [29, 105] in 2002 to determine the duration and chirp of light pulses. An illustration of the principle can be found in Figure 3.12 together with the streaking trace of a few-cycle laser pulse. With the streak camera the kinetic energy spectrum of photoelectrons after quasi-instantaneous ionization with an attosecond XUV pulse in the presence of the laser electric field is measured. The energy spectrum strongly depends on the phase of the laser electric field oscillation. A positive amplitude leads to acceleration, whereas a negative amplitude decelerates the photoelectrons. By temporally delaying both pulses in subsequent measurements, all cycles of the electric laser field are scanned. The result is a series of energy spectra corresponding to the underlying electric laser field for many time delays between subsequent pulses. From the streaking trace one can extract the pulse duration. The chirp information is deduced from maximum number of photoelectrons either at the rising (positive chirp) or falling (negative

chirp) slope. The curve itself reveals information on the underlying streaking electric field. This way, *Goulielmakis et al.* were able to directly record the electric field of a light waves in 2004 for the first time [106].

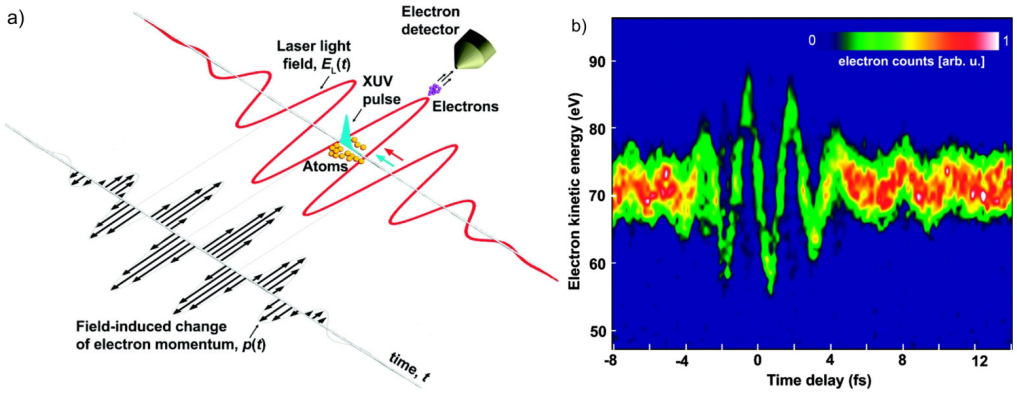

Figure 3.12.: Working principle of attosecond streaking a) and the streaking trace of a few cycle light pulse b): a few-cycle NIR laser pulse and an XUV attosecond pulse are focused into an atomic gas target. The XUV pulse photoionizes the gas quasi-instantaneously and generates electrons. The electrons undergo a momentum change by the NIR electric field (black arrows). This momentum change is measured with a time-of-flight electron detector. The final momentum of the photoelectrons depend on the ionization potential of the gas target, the energy of the XUV pulse, and the present phase of the NIR pulse. With subsequently changing the relative arrival time both pulses one can record a streaking trace and deduce directly the electric field of the laser. From [106]. Reprinted with permission from AAAS.

In the following the streaking theory is deduced. A constraint for attosecond streaking is that the duration of the XUV pulse is much shorter then the streaking NIR pulse: $\tau_{XUV} << \tau_{IR}$ [29]. For an infinitely short pump pulse the system response is described by the convolution of the function describing the dynamic behaviour and the intensity profile in the time domain and its Fourier transform:

$$R(t) = \int_{-\infty}^{\infty} I_{pump}(t-\delta t) f(t) dt \qquad \tilde{R}(\omega) = \tilde{I}_{pump}(\omega) F(\omega) \tag{3.24}$$

After the photo-ionization the electrons have a kinetic energy:

$$E_0 = \frac{1}{2} m_e v_0^2 = \hbar\omega_{XUV} - I_p \tag{3.25}$$

with the frequency of the XUV pulse ω_{XUV} and the ionization potential of the gaseous sample I_p. Assuming that the ponderomotive potential is much stronger than the photon energy of the NIR $U_p >> \hbar\omega_L$ and ionization potential of the gaseous sample is much smaller than the photon energy of the XUV pulse it is sufficient to treat the problem with classical

mechanics leading to a velocity of the photoelectron of:

$$\mathbf{v}(t) = -\frac{e}{m_e}\mathbf{A}(t) + \left[\mathbf{v}_0 + \frac{e}{m_e}\right]\mathbf{A}(t_i) \tag{3.26}$$

with the vector potential $\mathbf{A}(t)$, the initial velocity $\mathbf{v}_0$ and the time of ionization t_i . The first term represent the electron's quiver motion and the second the final drift velocity $\mathbf{v}_f = \mathbf{v}_0 + (em_e)\mathbf{A}(t_i)$. For linear laser polarization and detection in the propagation direction of the photo electrons one receives:

$$E_f = E_0 + 2U_p \sin^2\phi_i \pm \alpha\sqrt{8E_0U_p}\sin\phi_i \qquad \text{with } \alpha = \sqrt{1 - 2U_pE_0\sin^2\phi_i} \tag{3.27}$$

where ϕ_i denotes the optical phase of the streaking field, and α is a correction term when $U_p \simeq E_0^2$ (high intensity regime). This leads to a deflection of the photoelectrons considered with the negative sign. The broadening of the photo electron spectrum for a given phase is determined by the bandwidth and chirp of the XUV pulse and the variation of emission times occurring from the x-ray pulse duration.

3.7.3. Attosecond streaking in solids

The attosecond streak camera was proposed for time-domain investigations of attosecond electron dynamics of atoms and molecules [29]. It became also interesting for the investigation of solid samples. *Cavalieri et al.* were the first implementing attosecond streaking in 2007 on a solid tungsten sample [107]. *Neppl et al.* continued the investigation 2012 by studying the chemisorption of oxygen on tungsten. Moreover, they investigated Magnesium and did further studies on metal-metal interfaces (Mg on W) and dielectrics (Xe on W) [20, 108].

Dynamics in plasmonic nanostrucutred surfaces and nanostructures demonstrate a new sample type for attosecond streaking. *Stockman et al.* proposed the measured of the electric field of a plasmon directly in the time domain with attosecond streaking [73]. *Skopalova et al.* simulated attosecond streaking traces for plasmonic antenna structures with the finite-difference time domain (FDTD) method (see Section 4.1)[109]. The experimental setup for plasmon streaking is displayed together with the simulated results in Figure 3.13. The plasmonic antenna pair enables a strong field enhancement after excitation with the NIR pulse in the antenna gap. The XUV beam generates photoelectrons from the sample which are streaked in the superposed light and plasmonic electric field. Streaking curves from photoelectron at the edge of one gold antenna at a certain height and averaged over the total gap height are presented in bottom left and right, respectively. However, the field enhancement of the antenna structure is highest in the antenna gap parallel to the surface, and therefore not oriented in the direction to the time of flight detector. Also the number of photoelectrons originating from the antenna gap that contribute to the streaking signal is very low compared to the electrons from the antenna surface. This problem becomes already visible by comparing the modulation of the streaking traces that is stronger for the photoelectrons generated in the gap than averaged over the total height. Taking the electrons into account that will be generated from the surface, the signal from electrons inside the gap would be much lower than from the electrons on the surface.

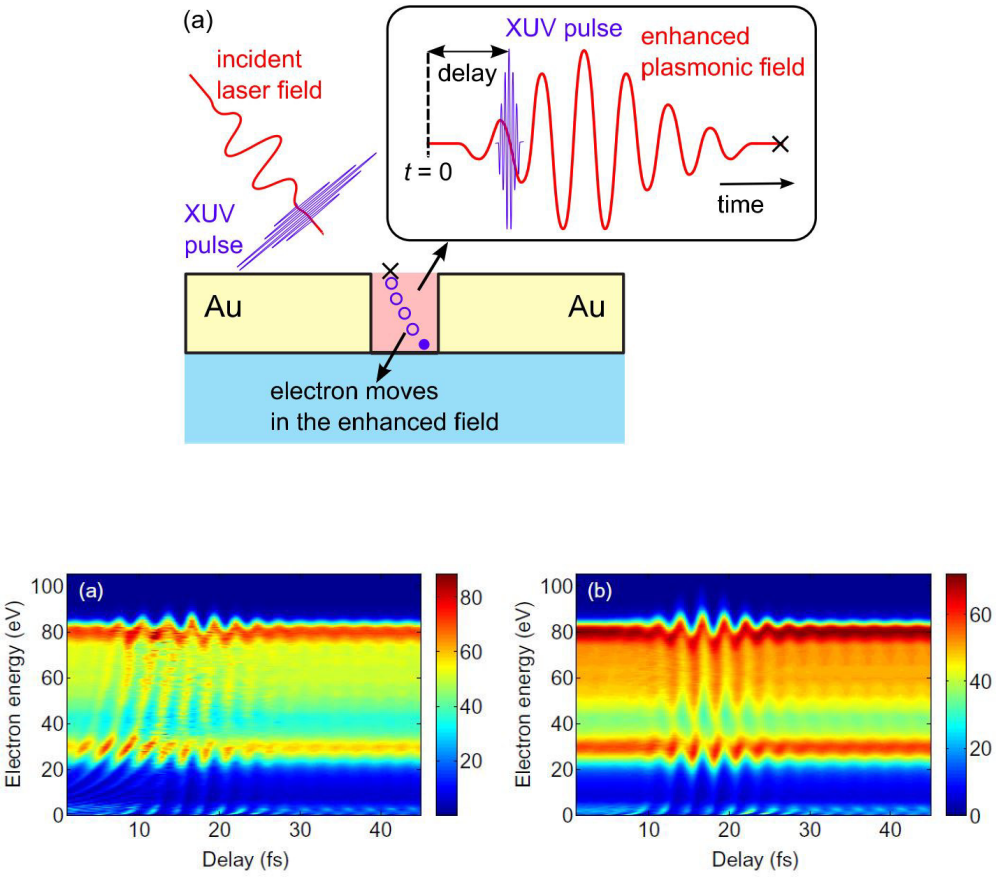

Figure 3.13.: Experimental setup (top) and simulated streaking traces (bottom) for attosecond streaking on coupled nanoplasmonic antennas for photoelectrons born at one position located at the edge of one antenna at a certain height inside the gap (bottom left) and averaged over the total gap height (bottom right). [109]

Kelkensberg et al. performed calculations on spherical plasmonic nanoparticles showing that streaking experiments are only sensitive to streaking fields that point into the detection direction [110]. Angular resolved measurements have to be done to access the other spatial components of the electric field. This confirms the difficulties in streaking experiments with plasmonic fields mainly aligned parallel to the surface as suggested by *Skopalova* and the need to find sample geometries supporting a vertical plasmonic field.

Attosecond spectroscopy gives direct access to the time domain of electron dynamics. However, for nanostructured plasmonic samples also spatial resolution would be beneficial. By combining attosecond spectroscopy with photoelectron emission microscopy (PEEM) as suggested by *Stockman et al.* and described in Section 2.9.2 one can get also spatial information of nanoplasmonic samples [73]. However, long exposure times make measurements difficult and might lead to sample destruction.

3.7.4. Attosecond photoscopy on plasmonic structures

The attosecond streaking camera was invented for light fields, atomic, and molecular dynamics. Streaking on surfaces reveals dynamics on the band structure of condensed matter. However, plasmonics reveal ultrafast dynamics below few hundreds of picoseconds down to few hundreds of attoseconds [9]. The investigation of plasmons in the energy domain, e.g. by reflection or transmission spectroscopy, allows the determination of the plasmon lifetime but does not give access to the electric field oscillations. This motivates the development of an experimental technique, which gives access to the electric field directly in the time domain. For these investigations, the scheme of the attosecond streak camera has to be adapted. The main challenge is to decouple the plasmonic field contribution from the streaking laser field. The electric field vector of a plasmon that is propagating on the surface points out perpendicular. The biggest contribution of the plasmonic field to the streaking field is achieved by placing the electron detector parallel to the plasmonic field vectors. To minimize the contribution of the laser field to the streaking field the detector has to be placed perpendicular to the light field vectors. This means the angle of incidence should ideally have the same direction as the detection angle, which is experimentally impossible. A technique developed for this specific requirements was proposed by *Lupetti et al.* and called attosecond photoscopy [111]. The attosecond photoscopy setup is a modification of the attosecond streak camera described in Section 3.7.2 and illustrated in Figure 3.14.

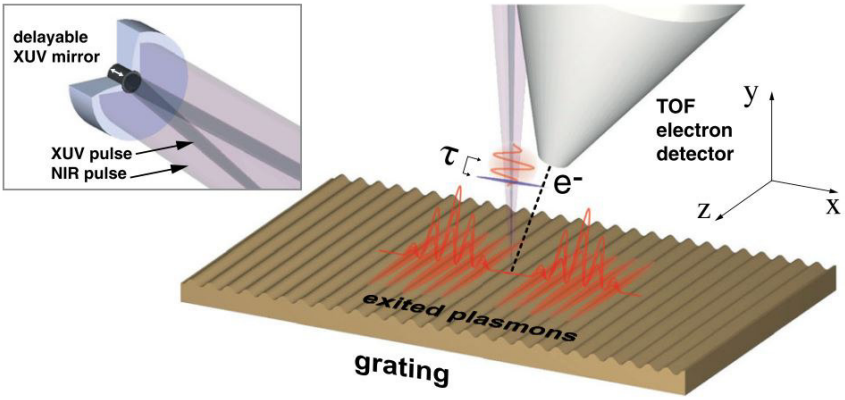

Figure 3.14.: Experimental setup of attosecond photoscopy: adaption of the attosecond streaking camera to the needs of the investigation of plasmonics. The incident laser field is polarized in the surface plane of the sample driving the electronic oscillation of a SPP. The detection angle is from the same direction as the incident pulse, that ideally only electrons experiencing the plasmonic field are detected. Reprinted figure with permission from [111]. Copyright (2014) by the American Physical Society.

The need of normal light incidence and a normal detection angle is realized by having near normal incidence of the XUV and NIR light and rotating the detector by a few degree so that the contribution of the laser electric field is still low. The XUV beam is generated by HHG

from a noble gas target resulting in two co-propagating beams. For time resolved experiments one of the pulse has to be delayed relative to the other. This is done with a two part mirror where the inner part is movable. The XUV multilayer mirror acts as a band pass filter for the high harmonic beam. At the sample surface, e.g. a gold grating, two counter propagating surface plasmon polaritons are launched by the NIR pulse. The delayed attosecond XUV pulse generates photoelectrons that are streaked in the plasmonic field. With the time-of-flight electron detector the kinetic energy of the photoelectrons accelerated by the plasmonic field are measured. The laser electric field accelerates electrons perpendicular to the detection axis and has only a small contribution. By sampling over a range of delays the plasmonic field can be temporally resolved. Note, that by simply rotating the detector parallel to the polarization of the light pulses, the contribution of the laser electric field can be retrieved additionally.

These kinetic energy spectra series are called photoscopic spectrograms. Spectrograms for perpendicular and parallel detection angles for the grating example of Figure 3.14 are presented in Figure 3.15 a) and b) respectively.

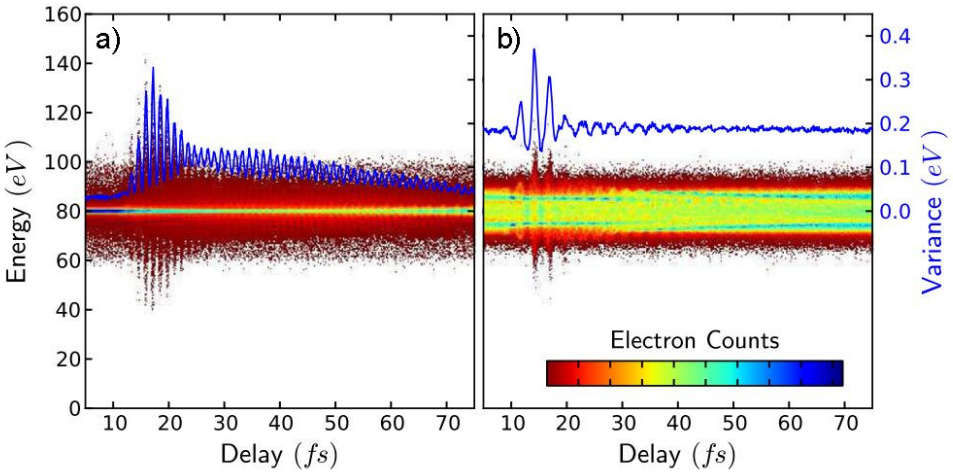

Figure 3.15.: Photoscopic spectrograms of a grating taken from perpendicular (left) and parallel (right) detection exhibiting the streaking trace of the plasmonic field and the light field, respectively. Reprinted figure with permission from [111]. Copyright (2014) by the American Physical Society.

The spectrogram in perpendicular orientation exhibits the information on the plasmonic field. The calculation of the variance clearly shows the plasmon build-up and dephasing of a bright and dark plasmon mode. The variance represents the vector potential $\mathbf{A}^2$ at the surface in the direction of the detector. The vector potential quadratically sums up the NIR laser field and the plasmonic field $|\mathbf{A}|^2 = \mathrm{A}_x^2 + \mathrm{A}_{SPP}^2$. The plasmonic field is assumed to have a Gaussian envelope:

$$\mathrm{A}_{SPP} = \exp\left(ik_{SPP}x - \omega_{SPP}t\right) \exp\left(-\frac{(k_{SPP}x - \omega_{SPP}t)^2}{2\omega_{SPP}^2 T^2}\right) \tag{3.28}$$

supporting two counter propagating surface plasmon polariton wave packets. It has a build-up and decay as a convolution of a Gaussian excitation with exponential decay for each bright and dark mode:

$$f(t) = \exp\left(-\frac{t}{2\tau_{d/b}}\right) \times \left(1 - \mathrm{erf}\left(\frac{\sigma_{d/b}^2 - 2\tau_{d/b}t}{2\sqrt{2}\sigma_{d/b}\tau_{d/b}}\right)\right) \tag{3.29}$$

with the carrier frequency $\omega_{d/b}$, build-up time $\xi_{d/b} = \sigma_{d/b}\sqrt{\ln 2}$, and lifetime $\tau_{d/b}$. Fitting this model to the calculated variance obtained from the streaking trace one receives the values for the fit parameters. Additionally one can extract the information in the same way as for conventional attosecond streaking.

Thus, with attosecond photoscopy it is possible to retrieve plasmonic characteristics with a similar setup as the established attosecond streaking camera.

4. Simulation of hybridization of nanodisk sandwiches

4.1. Simulation methods

For the investigation of the temporal dynamics in nanoplasmonic structures, the time evolution of the electric field is of interest. For the attosecond streaking experiments the orientation of the plasmonic field is important. Only the contribution towards the detector can be observed in streaking experiments. Therefore, the focus of the simulations here lies on a structure exhibiting the plasmonic field vector normal to the surface. The presented nanodisk sandwiches in the following sections provide the field enhancement normal to the surface. This makes the nanodisk resonators perfect structures for attosecond streaking experiments.

There are different methods to simulate the optical response of nanostructures [112]. Popular methods are *discrete-dipole approximation (DDA)* [113], *boundary element method (BEM)*[114, 115], and *finite difference time domain (FDTD)* [116]. These codes are designed to compute scattering properties of particles (DDA) or integrate differential equations in general, e.g. Maxwell's equations (BEM and FDTD). The simulation of the optical properties of nanostructure is only one application. Some implementations of these codes are available as open source, e.g. the Fortran code *DDSCAT* developed by *Draine* and *Flatau* [113], or the Matlab toolbox *MNPBEM* developed by *Hohenester* [117], and C/C++ code *MEEP* developed at MIT for FDTD calculations [118]. Another program is the commercial simulation software *CST Studio Suite* (Computer Simulation Technology (CST), Darmstadt, Germany) that is based on the *finite integration technique (FIT)* comparable to FDTD.

Each technique treats the interaction of electromagnetic fields with the nanostructure differently but without general limitations to its shape. Whereas *DDA* and *BEM* solve Maxwell's equations in the frequency domain and allow only static fields, *FDTD* and *FIT* work in the time domain and allow to investigate the dynamics of nanostructures. The DDA method uses a dipole lattice to represent the nanostructure in the simulation and models the interaction of the external field with the local electric field regarding influences of the other dipoles. The *BEM* method models only the surface of the nanostructure. The electromagnetic field of the structure is determined by the charges and surface currents. In *FDTD* and *FIT* the nanostructure is divided into smaller cells and the electric and magnetic fields are calculated by solving Maxwell's equations for each time-step in the differential form (*FDTD*) or integral form (*FIT*), respectively.

The time evolution of the electric field is only treated in the FDTD and FIT technique. Therefore in this work the *FIT* method is applied.

4.2. Simulation setup

Dmitriev et al. studied experimentally the hybridization [48], i.e. the interaction of plasmons originating from fundamental particle geometries with each other, in gold-silica-gold nanodisk sandwiches [52]. These sandwiches are composed of two gold disks with a height of $10\,\mathrm{nm}$, that are separated by a $10\,\mathrm{nm}$ silica disk. The diameter of the bottom disk is $108\,\mathrm{nm}$ and bigger than the diameter of the top disk with $88\,\mathrm{nm}$ as shown in Figure 4.1. By changing these geometrical dimensions, they found, that the aspect ratio of height to diameter of the smaller gold disk influences the hybridization of the system. In simulations and experiments

Figure 4.1.: Composition of the nanodisk sandwich. All dimension are given in nanometres.

two resonances in the extinction spectrum are clearly visible. In sandwich structures with thinner top disks the low energy resonance with anti-parallel orientation of dipole moments is much stronger. In sandwiches with thicker top disks the high energy resonance where dipole moments are aligned parallel becomes stronger. The coupling of the dipole moments is characteristic for resonator structures. The separated disks are linked across the spacing layer. The thickness of this spacing layer influences the coupling response whereas geometrical parameters of the metallic layers influence the resonance frequency.

The aim of my studies is the investigation of the influence of the confinement of bulk plasmons in a decreasing layer thickness in various triple layer nanodisk structures. A bulk plasmon needs a certain volume for its electronic oscillations. If the volume is reduced in one dimension by reducing the thickness, the electronic oscillations are perturbed and the response changes. The nanodisk structures that I model here are composed of a gold bulk layer covered by an insulating silica layer and a metallic thin top layer. The influence of the thickness of the thin layer is investigated. Another aspect in the response of a nanostructure is the diameter ratio of the bottom and the top disk. Therefore, the diameter of the bottom disk is the second variable. The program used for the simulations is *CST Studio Suite*. The simulation environment is tested by simulating the results from *Dmitriev et al.* [52] . The results are compared to the extinction spectra and electric near fields in the Appendix A.1.

In the following table an overview over the structures are given that have been used in the simulations.

Section	Layer thickness nm	Structure type	Diameters nm top; centre; bottom	Materials top - centre - bottom	Monitor
4.3	(1) to (3)	Single Disk	108	Au and Ag	Absorption cross section E-Field Temporal E-field
4.4.1	(10-10-1) to (10-10-3)	Sandwich	88; adaptive; 108	Au-SiO_2-Au	Absorption cross section E-Field
4.4.2	(10-10-1) and (10-10-3)	Sandwich	88 to 108; adaptive; 108	Au-SiO_2-Au	Absorption cross section
4.4.3	(10-10-1) and (10-10-3)	Sandwich	88 and 108; adaptive; 108	Au-SiO_2-Au	Temporal E-field
4.5.1	(10-10-1)	Sandwich	88; adaptive; 108	Au-SiO_2-Ag	Absorption cross section E-Field
4.5.2	(10-10-1)	Sandwich	88; adaptive; 108	Au-SiO_2-Ag	Temporal E-Field

In the beginning of this section the simulation of single gold and silver disks demonstrates the behaviour of such nanostructures. Then, the gold-silica-gold sandwiches are investigated. The simulation setup is shown in Figure 4.2. The sandwich is composed of two gold disks

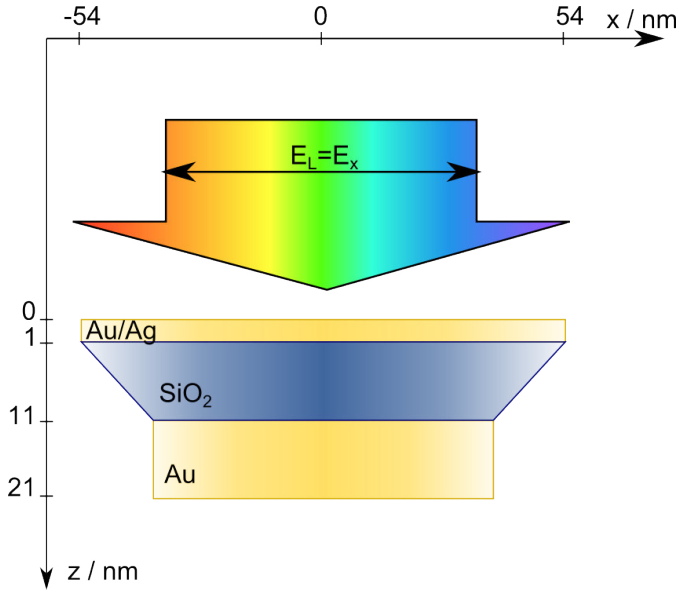

Figure 4.2.: Simulation setup: a gold-silica-gold/silver sandwich is illuminated from the top with a linearly polarized light pulse with a spectrum rainging from $550\,\mathrm{nm}$ to $1500\,\mathrm{nm}$. The disk diameters of the bottom and top disk $88\,\mathrm{nm}$ and $108\,\mathrm{nm}$, respectively. The spacing layer has an adaptive diameter from $88\,\mathrm{nm}$ to $108\,\mathrm{nm}$. The bottom and spacing disks have a thickness of $10\,\mathrm{nm}$, the covering disk of $1\,\mathrm{nm}$. To evaluate surface effects and the influence of the bulk the top disk layer thickness and the diameter of the bottom disk are varied in the simulations.

with $10\,\mathrm{nm}$ thickness (bottom layer) and $1\,\mathrm{nm}$ to $3\,\mathrm{nm}$ thickness (top layer, varied in first simulation) denominated as (10-10-1) to (10-10-3). The diameters are $88\,\mathrm{nm}$ to $108\,\mathrm{nm}$ (bottom disk, varied in second simulation) and $108\,\mathrm{nm}$ (top disk). Both disks are separated by a conical silicon dioxide spacer adapting the diameter of the metallic disks and a thickness of $10\,\mathrm{nm}$. With a unit cell size of $4.065\,\text{Å}$ for crystalline gold [119], a $1\,\mathrm{nm}$ gold layer is composed of approximately 2.5 monolayers and the $3\,\mathrm{nm}$ layer of approximately 7.5 monolayers.

In the (10-10-1) gold-silica-silver sandwich simulation the bottom disk has a thickness of $10\,\mathrm{nm}$ and a diameter of $88\,\mathrm{nm}$, the top silver disk has a thickness of $1\,\mathrm{nm}$ and a diameter of $108\,\mathrm{nm}$. The silver unit cell size has almost the same value as gold and is $4.079\,\text{Å}$ [119]. Therefore, the top silver disk is also formed by 2.5 monolayers. The silica disk again has a conical shape and a thickness of $10\,\mathrm{nm}$.

For the simulation of absorption spectra and electric near fields of the disk sandwich the sample is illuminated from above perpendicular to its surface by linearly polarized light as shown in Figure 4.2.

The nanodisk sandwiches are excited by temporally Fourier limited light pulses with a

spectral range of $550\,\mathrm{nm}$ to $1500\,\mathrm{nm}$. The spectrum and the temporal electric field are shown in Figure 4.3 a) and b), respectively. The electric field of the laser pulses has a carrier

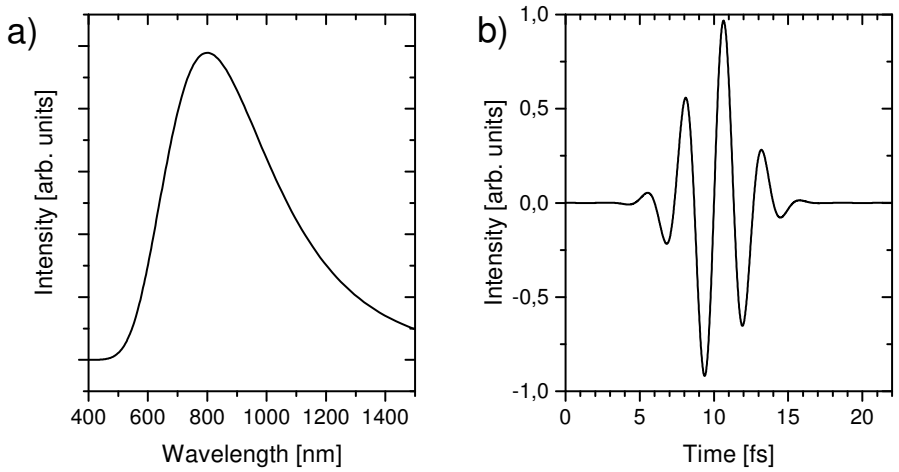

Figure 4.3.: Excitation pulses used in the nanodisk sandwich simulations. a) shows the spectrum b) the normalized temporal electric field.

envelope phase of $\pi/2$, corresponding to a sine-like electric field.

The simulation grid has a $1\,\mathrm{nm}$ spacing in x, y and z direction. The grid spacing is reduced in the region of the thin disk in z-direction perpendicular to the surface to $0.1\,\mathrm{nm}$. 'Open' boundary conditions are used adding space around the structure, where the electric field of the light pulse and from the structure itself are vanishing. This means, that the electric field of the pulse is absorbed at the edges of the simulation box, which is bigger than the simulated structure. Electric and magnetic symmetry planes are used in the case of the gold-silica-gold sandwich reducing the computing time.

4.3. Simulation of single gold and silver nanodisks

To investigate the behaviour of complex nanodisk sandwiches the response of the fundamental structure is important as mentioned out in the model of hybridisation in Section 2.7. The resonance in the absorption of a disk is mainly determined by its diameter [120]. A decreasing diameter results in a shift of the resonance to shorter wavelength and an increasing diameter shifts the resonance to longer wavelength. The simulation parameters are summarized in Figure 4.4 For very thin disks the absorption is shifted to shorter wavelength with increasing disk

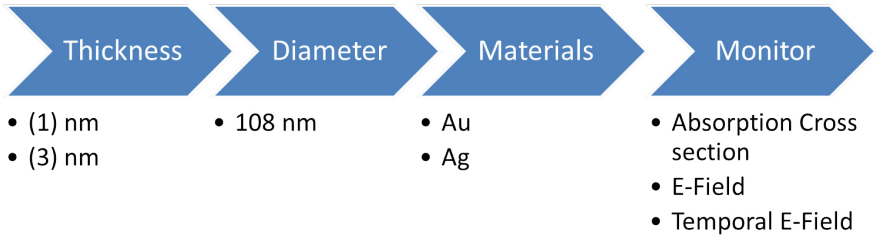

Figure 4.4.: Simulation parameter for single disk simulations.

diameter. The shift of the absorption cross section resulting from increasing the thickness in a gold and a silver disk are shown in Figure 4.5 a) and b), respectively. The disk diameter is $108\,\mathrm{nm}$ and the thickness is varied from $1\,\mathrm{nm}$ to $3\,\mathrm{nm}$. The resonance shift follows an

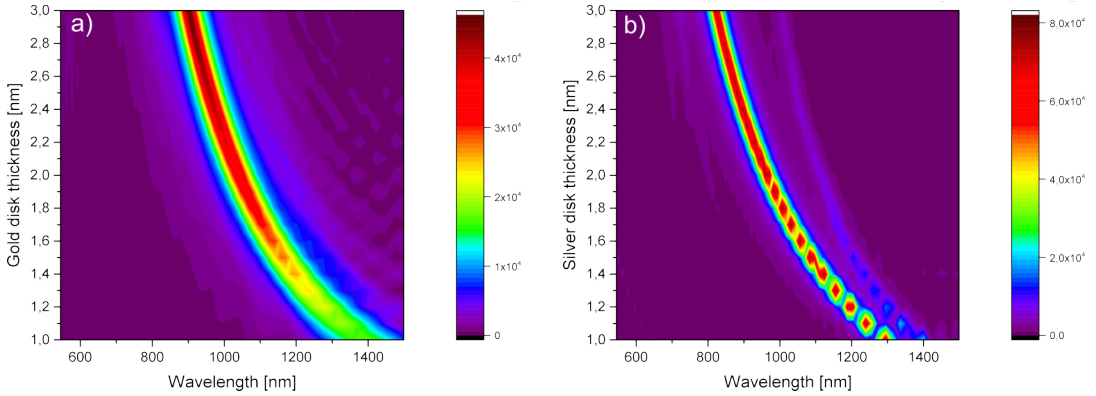

Figure 4.5.: False colour plot of the shift of the absorption resonance obtained from simulations of the absorption cross section of disks with increasing thickness for gold a) and silver b).

exponential shift corresponding to the aspect ratio. Therefore, the shift decreases with increasing the thickness. In case of the gold disk only one resonance is observed, whereas the silver disk shows satellite resonances with a low intensityat higher and lower photon energies.

The resonance of the silver disk is located at shorter wavelength around $820\,\mathrm{nm}$ compared to the gold disk resonance around $900\,\mathrm{nm}$. The dotting observed in the resonance shift of especially the silver disk results from a finite step size used in the simulations.

The benefit of *CST Studio Suite* is, that one can simulate also the electric near field at the sample surface. The electric field at the surface of the gold disk is induced by the excitation with monochromatic light at the resonance wavelength and is shown in Figure 4.6 a). The

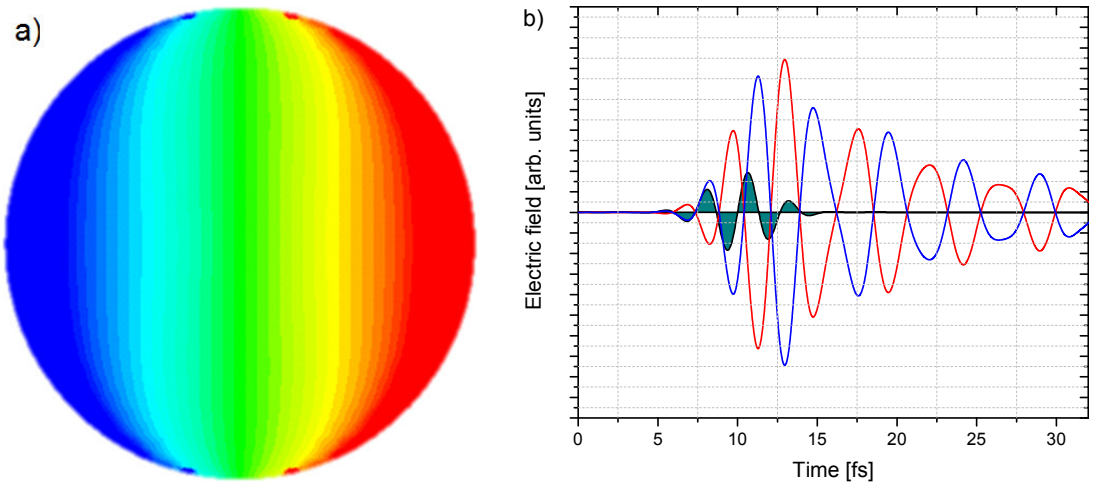

Figure 4.6.: Electric near field at the surface of a $1\,\mathrm{nm}$ thick gold disk excited with monochromatic light at $1390\,\mathrm{nm}$ a) and the temporal evolution of the integrated field of the left and right half disk b) (red and blue) after excitation with a broadband excitation pulse (blue shaded).

near field shows a dipole structure with the light polarisation axis as the symmetry axis. One half of the disk is negatively charged, the other positively with a smooth transition. The temporal evolution of the integrated field of the two half disks together with the excitation signal is shown in b). The driving light field induces a dipolar field that with a different phase, slower than the driving field. In one plasmonic field cycle the electric field builds up, then decreases and reverses to opposite polarity. After one cycle the field returns to the initial polarisation. During the plasmon built up, the electric field strength grows. The duration of the plasmon built up is almost as long as the driving laser pulse: the maximum of the excitation signal is reached around $10\,\mathrm{fs}$, whereas the plasmonic field still builds up, and reaches its maximum at around $13\,\mathrm{fs}$. At this time the laser field has almost vanished. After the plasmon built up, the electric field oscillates on the disk and is damped over time. The plasmon dephasing takes $32\,\mathrm{fs}$ until the plasmonic field reduced its field strength of $1/e^2$. For the plasmonic response of a single disk the resonance shifts with decreasing diameter and increasing thickness to shorter wavelength, and the plasmonic field on the disk surface is represented by one dipole.

4.4. Surface plasmon modes in gold-silica-gold nanosandwiches

4.4.1. Influence of the top disk thickness

In the following section the formation of surface plasmon modes in (10-10-1) gold-silica-gold nanodisk sandwiches is investigated. The simulation parameters are summarized in Figure 4.7. The initial sandwich structure is composed of $10\,\mathrm{nm}$ and $1\,\mathrm{nm}$ gold disks separated by

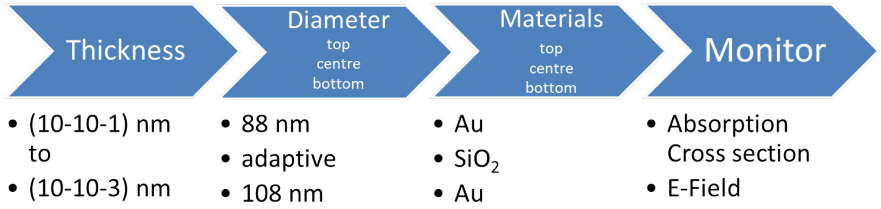

Figure 4.7.: Simulation parameter for investigating the influence of the top disk thickness.

$10\,\mathrm{nm}$ silica. The initial diameters of the disks are $88\,\mathrm{nm}$ and $108\,\mathrm{nm}$ of the bottom and the top disk, respectively. The top disk thickness is varied from $1\,\mathrm{nm}$ to $3\,\mathrm{nm}$ and absorption spectra are calculated. The corresponding spectra are given in Figure 4.8 a) as a false colour plot indicating shifts of the resonance wavelength. In b) the cross-sections are plotted in $0.5\,\mathrm{nm}$ steps. Four resonance peaks are observed for $1\,\mathrm{nm}$ top disk thickness located at:

$$\lambda_1 = 662\,\mathrm{nm} \qquad \lambda_2 = 709\,\mathrm{nm}$$
$$\lambda_3 = 802\,\mathrm{nm} \qquad \lambda_4 = 1021\,\mathrm{nm}$$

Starting with these four resonances, the peaks are merging with increasing thickness to finally two modes for $3\,\mathrm{nm}$:

$$\lambda_1^* = 650\,\mathrm{nm} \qquad \lambda_2^* = 720\,\mathrm{nm}$$

The electric near field at the surface of each sandwich is simulated with monochromatic excitation for all resonance wavelengths. The electric field changes with the phase of the excitation wave. The electric fields shown next to the peak are averaged over the total phase from 0 to π. For the four resonances of the (10-10-1) sandwich the electric field differs in the number of maxima with up to eight separated maxima within the three long wavelength resonances. The short wavelength resonance obtains six maxima, where the two banana form maxima are likely formed by three merged individual maxima. These patterns are described using the spherical transversal electro-magnetic modes (TEM) as TEM 11 to TEM 31. The TEM 11 appears at λ_4, with the higher modes 21-31 at the shorter wavelengths λ_3 to λ_2. The resonance located at λ_1 is likely represented by the TEM 41. By doubling the thickness

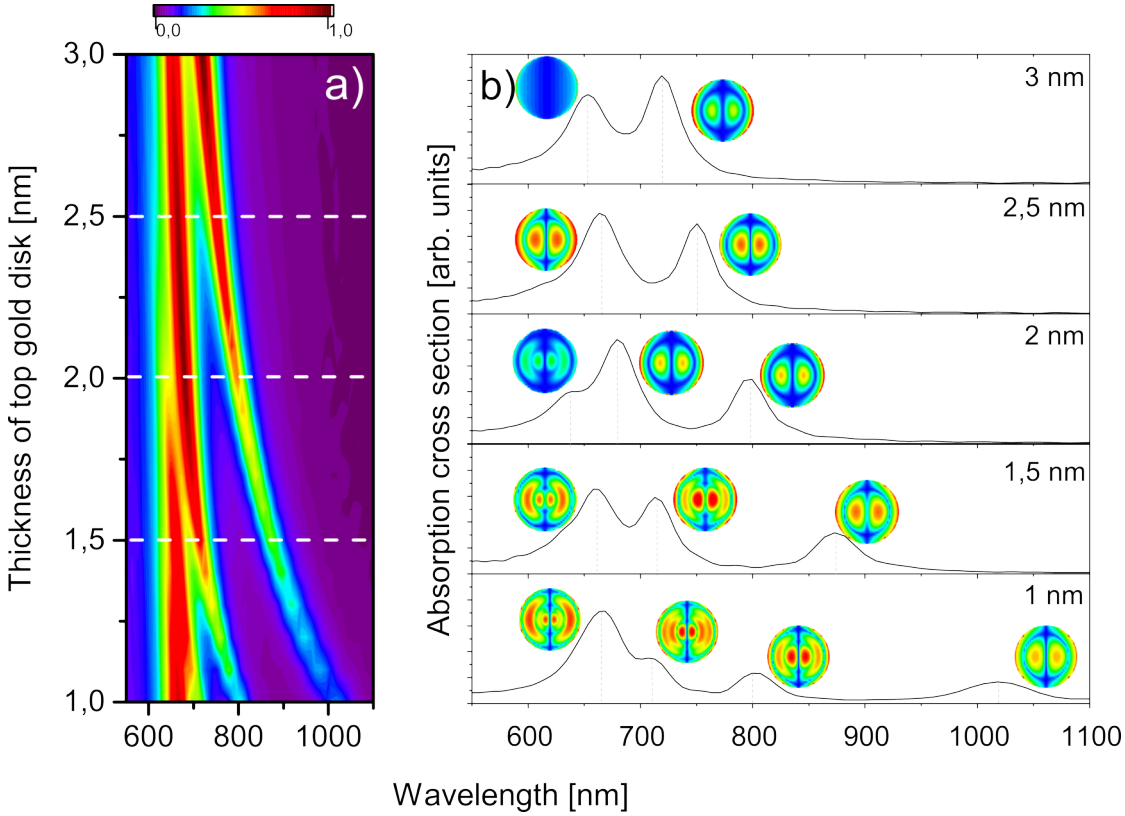

Figure 4.8.: False colour plot of the absorption cross sections of (10-10-1) to (10-10-3) sandwich systems a), and spectra at different distinct thickness b) together with electric near field excited with the resonance wavelength.

to $2\,\mathrm{nm}$ the TEM 41 already vanishes and the TEM 31, TEM 21, and TEM 11 shifted and decreased their amplitude. This can be seen in the electric near field representation. When the thickness is increased further up to $2.5\,\mathrm{nm}$ only two modes are found, which were observed in the studies by *Dmitriev*, too. The electric field on the surface has changed in the λ_1^* resonance to the dipole structure found for single disks. Whereas, in the λ_2^* resonance the TEM 11 structure is observed. The dipolar resonance shows no special surface structure and is therefore identified as a volume mode. Looking at the resonance shift the resonances of the two short wavelengths modes at λ_1 and λ_2 are only slightly shifted before they are merging and vanishing. The two long wavelengths modes at λ_3 and λ_4 are strongly shifted by approximately $150\,\mathrm{nm}$ and $200\,\mathrm{nm}$, respectively.

4.4.2. Influence of the bottom disk diameter

In the next step, the influence of the ratio of the top and bottom disk diameters is investigated for the (10-10-1) and (10-10-3) geometries. An overview of the simulation parameters is given in Figure 4.9. Starting from a diameter of $88\,\mathrm{nm}$ the radius of the bottom gold disk

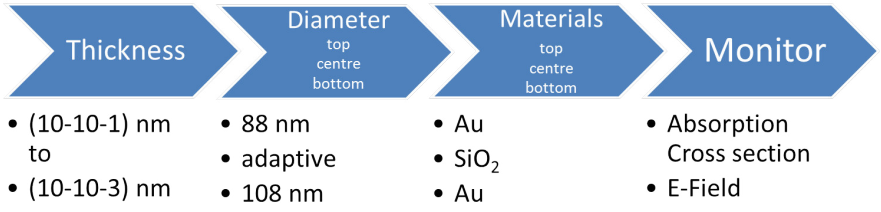

Figure 4.9.: Simulation parameter for investigating the influence of the bottom disk diameter.

is increased up to $108\,\mathrm{nm}$ with $2\,\mathrm{nm}$ steps until the diameters of both disks are equal. The simulated absorption cross sections are shown as false colour plot as a function of the radius of the thick gold disk in Figure 4.10 for the (10-10-1) geometry in a) and the (10-10-3) geometry in b). In c) and d) the absorption cross section spectra are shown at a diameter of $92\,\mathrm{nm}$. The main difference in the absorption of the two systems is the number of modes, which was found out already in the simulations varying the top disk thickness. The (10-10-1) system obtains four modes with the smallest diameter of the bottom disk. With increasing diameter, the three long wavelength modes at $1021\,\mathrm{nm}$, $802\,\mathrm{nm}$ and $709\,\mathrm{nm}$ are smearing out and vanish at equal diameters of top and bottom disk. The remaining mode is the short wavelength mode in contrast to the thickness variation. Whereas, the (10-10-3) system features only two modes in the beginning. Here, the short wavelength mode is remaining and the long wavelength mode is vanishing. In both systems the remaining mode is located around $700\,\mathrm{nm}$. As shown in the first simulation the different wavelength modes originate from surface modes. The remaining λ_1^* resonance became a bulk mode. Here, with equalizing diameters, the low order TEMs disappear and the remaining bulk mode is created from the high order TEM. Therefore, the excitation of the surface modes requires an asymmetry in the top and bottom disk diameter, otherwise only one bulk mode builds up from the cross talking of the both metal disks. Also, the formation of parallel and anti-parallel dipole arrangements found for the asymmetric disk diameters in the (10-10-3) sandwich requires this asymmetry.

4.4.3. Temporal evolution

In the following, the temporal evolution of the electric field of the (10-10-1) system with asymmetric $88\,\mathrm{nm}$ and symmetric $108\,\mathrm{nm}$ bottom disk diameter is investigated. The resulting electric field is a superposition of the excited TEMs shown in Section Kap:AuSiO2AuThickness. Even though they are simultaneously excited by a coherent Fourier

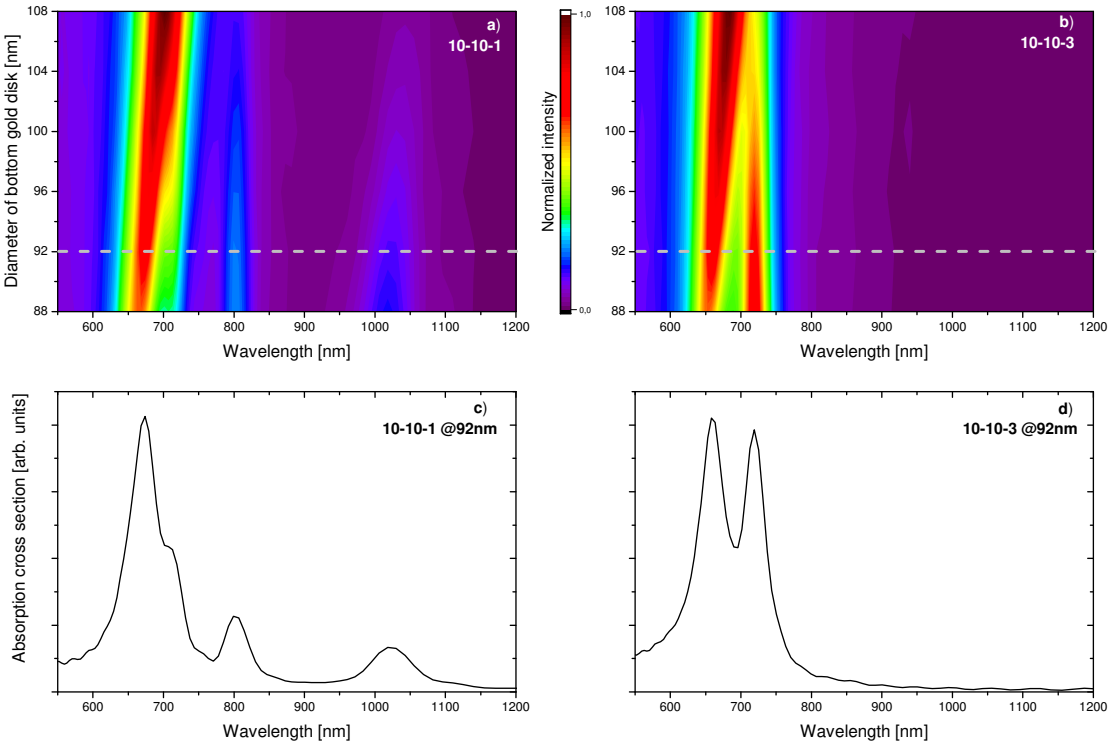

Figure 4.10.: False colour plot of the evolution of the absorption cross section with variation of the bottom disk diameter for a top disk thickness of a) $1\,\mathrm{nm}$ and b) $3\,\mathrm{nm}$ and absorption cross section spectra for a distinct diameter of $92\,\mathrm{nm}$ for $1\,\mathrm{nm}$ thickness c) and $3\,\mathrm{nm}$ thickness d).

limited pulse their temporal appearance is not synchronised. Therefore the total electric field is expected to oscillate with a complex structure. The simulation parameters are summarised in Figure 4.11. The electric near field is simulated with $0.2\,\mathrm{fs}$ steps until the amplitude drops

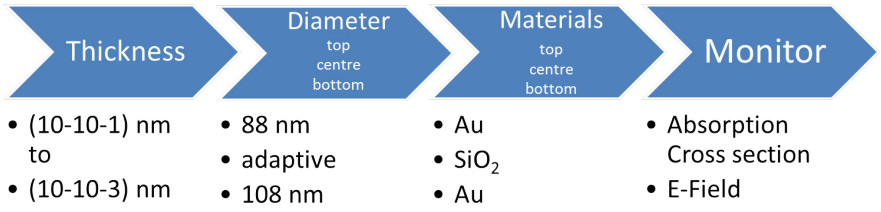

Figure 4.11.: Simulation parameter for investigating the temporal electric field influenced by the top disk thickness.

below $1/e^2$ of its maximum value. The field is monitored along the centre line at two different positions on the surface, and inside the sandwich parallel to the polarization of light . The results are presented as false colour plots in Figure 4.12 in a)-c) and in d)-f), respectively . In a) and d) the electric field directly at the top surface of the sandwich is shown. Local minima and maxima indicated by the red and blue areas are separated by white lines. Therefore, a dipole mode is represented by a vertical red and blue area separated by a white line. The next higher mode is composed by two minimum/maximum pairs separated by white lines. In the $88\,\mathrm{nm}$ sandwich first a dipolar mode structure appears in the centre but around $18\,\mathrm{fs}$ a surface mode with two minimum/maximum pairs is pronounced . Another splitting happens around $20\,\mathrm{fs}$, where the outer minimum/maximum pair splits up ending in total in four modes. In the $108\,\mathrm{nm}$ sandwich the first split happens at almost the same time, but the splitting starts earlier around $25\,\mathrm{fs}$. The minima/maxima in a) are propagating first from the outside to the center of the disk. This can be seen from the bending of the vertical aligned maxima/minima. A bending to the right refers to a propagation from outside to the inside, and a bending to the left shows the propagation from inside to outside. At $32\,\mathrm{fs}$ there is a change of their propagation direction, further denominated as phase variation. Afterwards the minima/maxima are travelling from the disk center to the outside. Around $40\,\mathrm{fs}$ and $48\,\mathrm{fs}$ there appear two more phase variations, where the minima/maxima change their direction. Comparing a) and d), the minima/maxima change their propagation direction more pronounced in the asymmetric sandwich. The modes appearing in the symmetric sandwich are oscillating more statically over the full time range at the same position. The first and second phase variation appear roughly $3\,\mathrm{fs}$ later in the $108\,\mathrm{nm}$ system, whereas the third phase variation appears delayed with $6\,\mathrm{fs}$.

The phase variation process is determined in the center of the insulator SiO_2 in b) and e). These positions are only accessible in the simulations but not in experiments. The number of appearing modes differs at this position as well. The field strength is increased

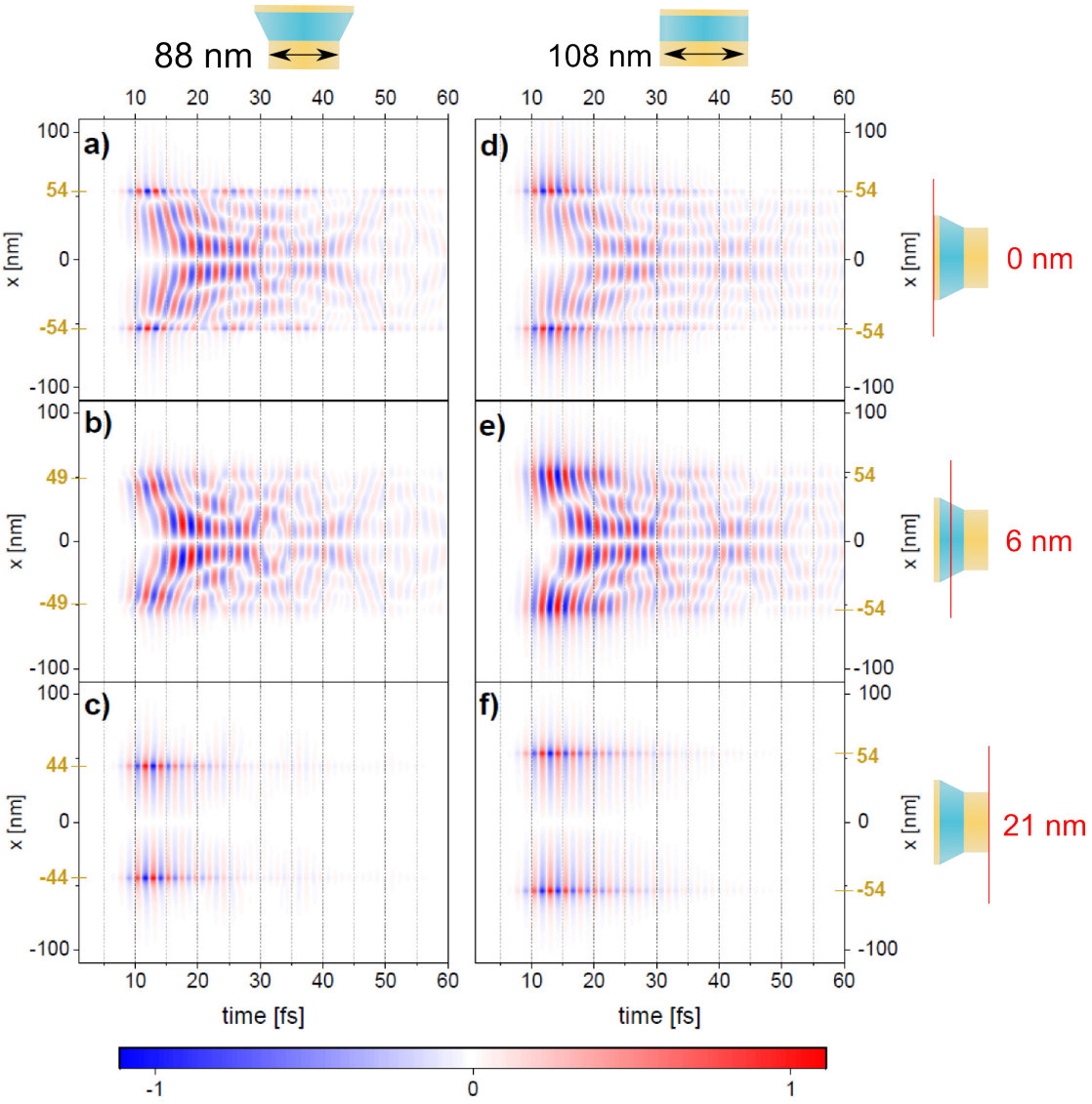

Figure 4.12.: Plot of the electric near field evaluated along the centre line for asymmetric (left column) and symmetric (right column) sandwiches on the top surface a) and d), in the dielectric layer b) and e), and the bottom surface c) and f), respectively. The observation line is parallel to the incident field.

compared to the top of the surface, because of the separation by the dielectric. The temporal evolution of the electric field shown in c) and f) refers to the bottom surface.There is only a small influence of the surface modes to the bulk plasmon in the lower gold disk resulting in a stronger amplitude of the near field and a small temporal variation of the width in the asymmetric sandwich after $30\,\mathrm{fs}$.

In an attosecond streaking experiment one would obtain the temporal evolution of the field on the surface of a nanodisk from the streaking trace. The acceleration and deceleration of the photoelectrons depend on the emission position and the range of the electic field. For simulating the streaking trace and to study the lifetime of the surface modes, the electric near field is integrated on the top surface over the left and right half disk. The results for $88\,\mathrm{nm}$ and$108\,\mathrm{nm}$ are shown in Figure 4.13 in a) and b), respectively. In a) one observes

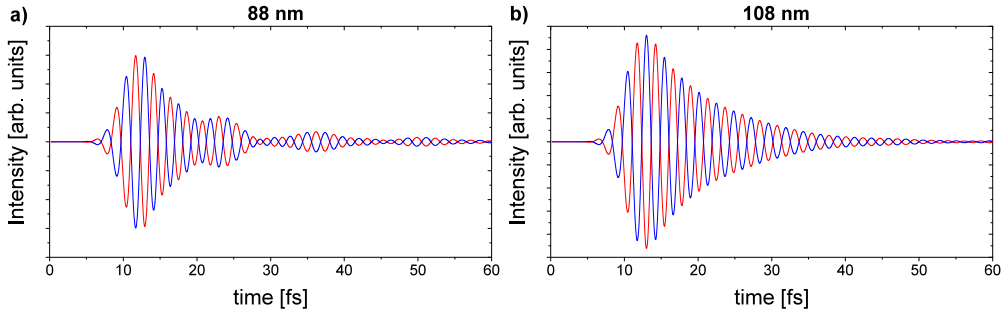

Figure 4.13.: Temporal evaluation of the electric field integrated over the right and left half sandwich surface in the asymmetric $88\,\mathrm{nm}$ a) and symmetric $108\,\mathrm{nm}$ b) sandwich.

that the integrated field oscillates with a high frequency resulting from the plasmonic field superposed with a low frequency. The low frequency oscillation results from different times of the appearance of the modes. The electric near field first builds up, has its maximum around $12\,\mathrm{fs}$, and then decreases. After some time the field increases again with a temporal delay of approximately $12\,\mathrm{fs}$ relative to the first mode. A third mode has its maximum around $36\,\mathrm{fs}$ and a fourth mode around $52\,\mathrm{fs}$. In b) only the high frequency oscillation is visible. The build-up time for the first (temporal) mode is similar for both sample geometries. Significant differences are found in the dephasing times. Whereas, the $108\,\mathrm{nm}$ system is dephasing in only one mode, the $88\,\mathrm{nm}$ system shows the build-up and dephasing of four modes with specific build-up- and lifetimes. These temporal modes are not directly related to the appearance of the surface modes, but show different temporal regimes of the total field strength. To obtain spatial information on the surface modes, one has to change the monitoring geometry. These simulations are performed in the following.

Finally, the surface modes are probed in a similar configuration as attosecond photoscopy but on much smaller lenght scales within one disk. The electric field is evaluated at two positions at $10\,\mathrm{nm}$ (blue line) and $22\,\mathrm{nm}$ (red line) on the $y = 0$ axis perpendicular to the propagation of the modes. In their temporal evolution the modes are travelling through the field monitor giving information about the relative intensity with respect to each other and the temporal evolution of the fields relative to each other. The results are shown in Figure

4.14. a) shows the evaluation for the asymmetric $88\,\mathrm{nm}$ and b) for the symmetric $108\,\mathrm{nm}$

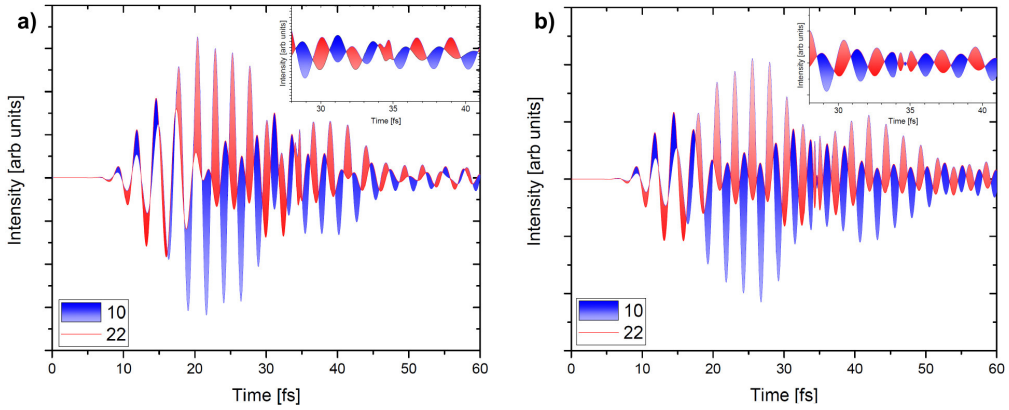

Figure 4.14.: Electric field at the surface monitored in two positions on the $y = 0$ axis at 10 and $22\,\mathrm{nm}$ of the asymmetric a) and symmetric b) disk sandwich.

sandwich. The areas with top blue and bottom red shades indicate the times where the field at $10\,\mathrm{nm}$ is stronger than the field at $22\,\mathrm{nm}$. At the phase variation around $18\,\mathrm{fs}$ the shaded colours are switching in the top region from blue to red , indicating that the mode in the outer part has now a stronger electric field than the mode in the inner part. The insets shows the region around $35\,\mathrm{fs}$ where in the $108\,\mathrm{nm}$ case a symmetrical phase variation appears whereas in the $88\,\mathrm{nm}$ the phase variation is anti-symmetrical. Both phase variations happen on a very short time scale within several hundreds of attoseconds and the intermediate phase lasts less than $500\,\mathrm{as}$. Symmetrical shapes show the regions where the fields at both positions are oscillating with the same phase relation. An anti-symmetrical shape indicates that the field at one position oscillates faster than at the other position. The more unstable the oscillation is, the more anti-symmetrical shapes appear. Thus, the symmetrical shapes in b) correspond to the locally stable modes figured out in Figure 4.12.

Summarizing the results, for the build-up of surface plasmon modes two criteria have to be fulfilled: the resonator has to be composed of two disks with unequal diameters and the bigger one has to be a very thin disk composed of a few monolayers . Fulfilling these conditions, surface modes can be launched. The superposition of the modes is complex and leads to a non-regular pattern of the electric field changing with time. The phase variations representing a change of the propagation direction happen on attosecond time-scale. The surface modes appear at different times in the plasmon propagation and have characteristic build-up and dephasing times on a sub-femto-second time-scale. With two measurement geometries attosecond streaking and attosecond photoscopy are modelled. The results show, that in principle for spatial investigation of plasmon propagation the attosecond photoscopy reveals more information than attosecond streaking.

4.5. Ultrafast plasmon modes in gold-silica-silver sandwiches

4.5.1. Surfaces modes

In the following simulations launching surface modes in gold-silica-silver sandwiches is investigated with the parameters summarized in 4.15. The sandwich is composed of a bulk

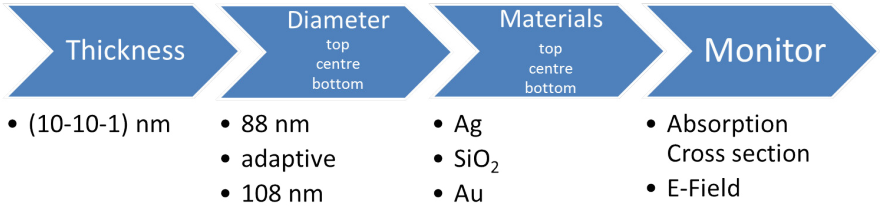

Figure 4.15.: Simulation parameter for the investigation of surface plasmon modes in gold-silica-silver sandwiches.

gold disk with $10\,\mathrm{nm}$ thickness and $88\,\mathrm{nm}$ diameter and a silver disk with $1\,\mathrm{nm}$ thickness and $108\,\mathrm{nm}$ diameter. Both disks are separated by a $10\,\mathrm{nm}$ silica layer with adaptive diameter. The simulated absorption cross-section of the system is shown in Figure 4.16 a). The

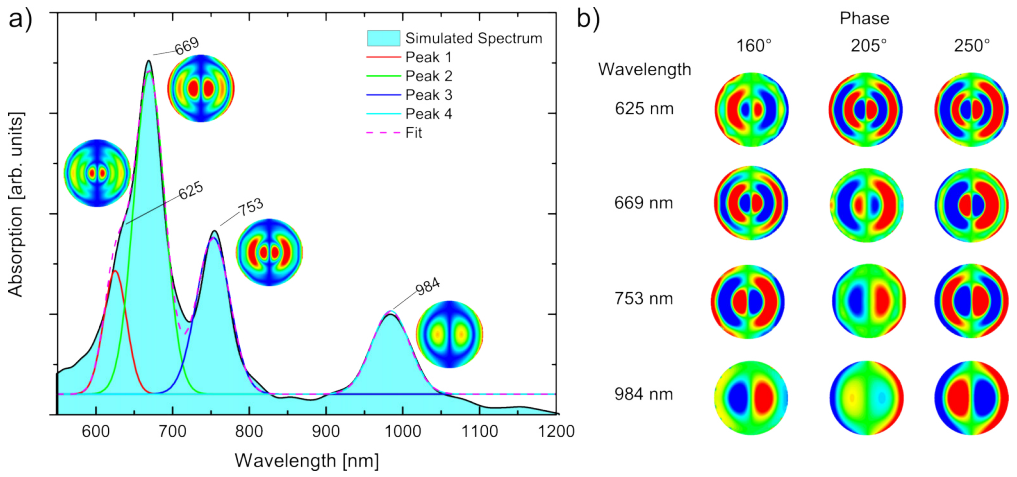

Figure 4.16.: Excitation of surface modes in a gold-silica-silver sandwich. a) shows the absorption spectrum with the time averaged electric near field by monochromatic excitation. b) shows the evolution of the electric near field for different phase values.

absorption shows several resonance peaks that can be attributed to different electric field

modes, similar to the modes in the gold-silica-gold sandwich. The time averaged electric field of the modes are shown next to the absorption peaks. The modes can also be attributed to TEM 11 - TEM 41 modes. In the time average the modes look similar to the modes enhanced in the top gold disk as shown above. By evaluating the modes for monochromatic excitation at different phases (e.g. the maximum, zero crossing, or minimum) as shown in b) one observes a different behaviour. The resonance located at $625\,\mathrm{nm}$ is composed at $160°$ of a minimum/maximum (min/max) pair with opposite sign with respect to the center and outer min/max pair. A phase shift of $45°$ shows four alternating min/max pairs. This pattern does not change significantly within another phase shift of $45°$. Only the amplitudes change. The second resonance at $669\,\mathrm{nm}$ obtains four min/max pairs only at a phase of $160°$. A phase shift of $45°$ leads to a reduction to only two clear modes in the center of the disk. In the outer part alternating min/max spots become visible resulting in a built up of a ring mode in the oscillator. Another phase shift of $45°$ leads to a vanishing of the ring mode with three remaining min/max pairs with opposite sign of the center pair. The third resonance at $753\,\mathrm{nm}$ composed of three alternating min/max pairs reverses within a phase shift of $90°$ instead of $180°$. In the intermediate state only two min/max pairs with the same sign appear. The outer min/max pair exhibits a circular modulation but without sign changes, too. The fourth resonance at $984\,\mathrm{nm}$ features only two min/max pairs that change their sign.

4.5.2. Temporal evolution of E-Field

In the following the appearance of the circular modulation and the formation of ring modes are investigated in more detail. The simulation is summarized in Figure 4.17 When the electric

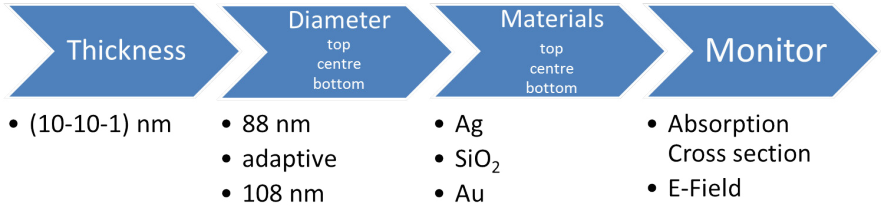

Figure 4.17.: Simulation parameter for the investigation of the temporal E-field on the gold-silica-silver sandwich surface.

field at the top disk surface is evaluated along a concentric half circle, as shown in Figure 4.18 in a) and b) for radii of 22 and $48\,\mathrm{nm}$, respectively, one observes significant differences in the mode pattern. In the central ring in a) only a regular dipole mode is visible arising with the excitation and changing its sign consecutively with a sinusoidal superposition resulting in more intense regions and less intense regions. The dipole oscillation is decaying exponentially within $60\,\mathrm{fs}$ to $1/e^2$. The symmetry axis is the $90°$ line, that is the line perpendicular to

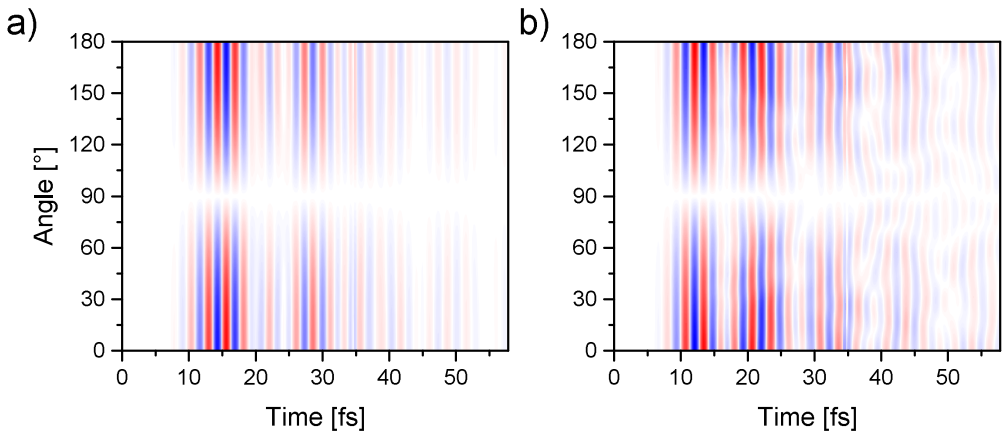

Figure 4.18.: Evolution of the electric field on the sandwich surface along a ring with radius 22 a) and $48\,\mathrm{nm}$ b) showing the volume mode in the inside and the ring modes in the outside appearing after around $35\,\mathrm{fs}$.

the light polarization vector. Whereas in the outer ring close to the edge of the disk after excitation also a dipole mode dominates but after $40\,\mathrm{fs}$ an asymmetric circular ring mode emerges. The circular mode can be figured out by the changing polarity along the line at a constant time step close to $40\,\mathrm{fs}$ and $50\,\mathrm{fs}$. Up to eight poles are appearing. These ring modes lead to the built up of a ring current in the disk sandwich resonator, which is usually excited with the resonant coupling of a propagating plasmon from a wave guide to a ring resonator. Here, a small asymmetry of the electric field of the excitation pulse induces the built up of an asymmetric charge distribution.

The evaluation of the electric field on the top disk surface along the $y = 0$ axis is shown in Figure 4.19 a). The electric field evolution at two specific positions ($10\,\mathrm{nm}$ and $22\,\mathrm{nm}$) are selected in b). In a) the bending of the minima and maxima determines the propagation direction, again. In the beginning the propagation direction is from outside to inside up to $25\,\mathrm{fs}$ since the minima and maxima are bent to the right. Here a phase variation happens. Afterwards the propagation direction switches and the modes are travelling from inside to outside up to $30\,\mathrm{fs}$, where the direction changes again. This switching repeats for several times. The temporal evolution along the line shows a splitting of the outer minimum/maximum pair that happens constantly over the whole time window. The splitting of the minimum/maximum pair of the inner dipole mode into two pairs corresponding to a surface mode happens around $18\,\mathrm{fs}$. The splitting lasts for about $8\,\mathrm{fs}$ until the minimum/maximum pair merges again. Afterwards the splittings are more irregular. Around $28\,\mathrm{fs}$ the inner minimum/maximum pair splits again but at a position more outside and the two pairs are only slightly shifted with respect to each other. The outer of the two pair is merging around $37\,\mathrm{fs}$ with the outermost mode. After the phase variation at $30\,\mathrm{fs}$ there happens another splitting of the inner pair with only a slight shift. Both pairs exist over the whole time window but the splitting position oscillates locally between $19\,\mathrm{nm}$ and $27\,\mathrm{nm}$.

In b) the electric field intensity at the position of the volume mode at $10\,\mathrm{nm}$ (blue line)

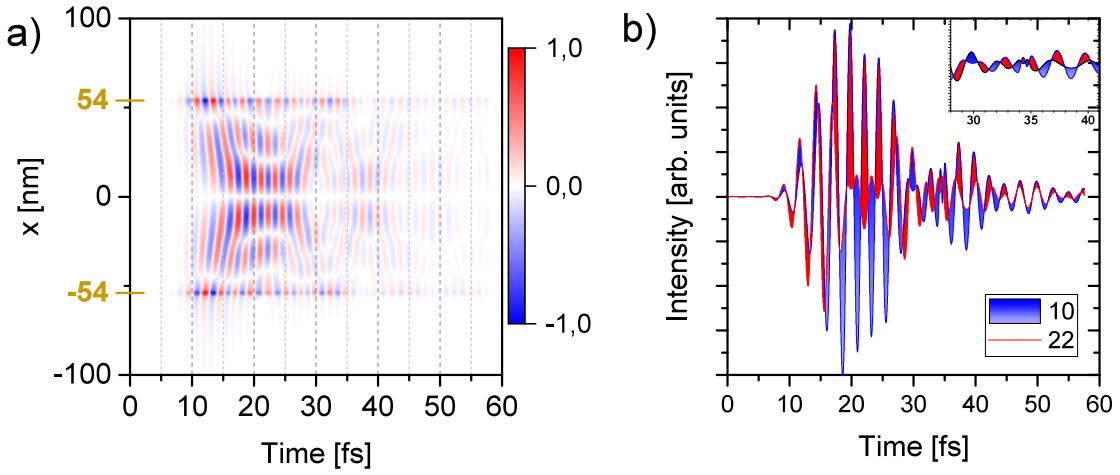

Figure 4.19.: Electric field along a line on the surface a) and the field on two positions at 10 and $22\,\mathrm{nm}$ b). The observed line is parallel to the incident field.

and the surface mode at $22\,\mathrm{nm}$ (red line) are shown. The top blue and bottom red shaded areas correspond, as in the gold-silica-gold sandwich, to the regions where the field at $22\,\mathrm{nm}$ is stronger than the field at $10\,\mathrm{nm}$ and the other way around. The asymmetry of the area corresponds to different phase velocities. In the region $< 15\,\mathrm{fs}$ the intensity of the volume mode is stronger in the outer part of the mode than in the inner part. After $15\,\mathrm{fs}$ a surface mode determines the intensity profile and the intensity becomes stronger at the $10\,\mathrm{nm}$ position compared to $22\,\mathrm{nm}$. This lasts up to $30\,\mathrm{fs}$. With increasing times the intensity ratio switches again several times indicated by the colour switching from top to bottom. In the gold-silica-silver sandwich a phase variation happens on the attosecond time-scale as well.

To summarize the results of the gold-silica-silver sandwich, the surface modes in the top silver disk have a circular asymmetry in contrast to the top gold disk leading to the build up of ring modes (whispering gallery mode [121]) and the formation of a ring current. This results from the asymmetry of the electric field within the excitation pulse. These ring mode formation should be investigated in more detail with different pulse forms simulating a CEP scan.The ring modes are refined to the outer part of the disk, whereas in the inner part surface and volume modes dominate. The temporal structure shows phase variation features on the attosecond time-scale again.

5. Attostreaking on gold and tungsten trioxide surfaces

5.1. Overview

The first report on attosecond spectroscopy experiments in condensed matter is the streaking on a single crystalline tungsten surface by *Cavalieri et al.* [107] . *Neppl et al.* extended this initial approach by streaking on single crystalline magnesium [20, 108]. The control of optically induced currents in dielectrics were investigated with attosecond light pulses as well [56, 57]. In the framework of a research collaboration we could demonstrate the extension to poly-crystalline gold and amorphous tungsten trioxide without prior surface preparation techniques as sputtering or annealing [122]. The streaking experiments were performed in a collaboration with the group of J. Tisch at Imperial College mainly by W. Okell (Imperial College, London) and are published in [22] and [123]. The attosecond beamline is described in Section 5.2. The aim of the attosecond streaking studies on gold and tungsten is the investigation of electronic processes on the sample surface. Transport effects like inelastic scattering from relaxed or excited electrons influences the broadening of the electron wavepacket. Also plasmonic excitations from a surface plasmon or inter- and intraband plasmons influence the photoelectron energy and their flight time. In case of streaking experiments on nanostructured surfaces, it is necessary to find cleaning techniques which do not destroy the surface as it happens with e.g. annealing leading to melting of nanostructures and sputtering leading to removing the structure. In Section 5.3.2 , the electron transport from the bulk of a gold sample into vacuum is investigated. The evidence of a plasmonic contribution to the streaking is discussed in Section 5.3.3. The electron transport time from the bulk to the surface is investigated for the tungsten trioxide sample in Section 5.4.2.

5.2. Attosecond streaking beamline @ Imperial College

For the attosecond streaking experiments a femtosecond laser system (Femtopower HE CEP, Femtolasers) with an output of $28\,\mathrm{fs}$ pulse duration, up to $1\,\mathrm{mJ}$ pulse energy with a repetition rate of $1\,\mathrm{kHz}$ is used. A hollow core fibre setup temporally compresses the pulses to $0.4\,\mathrm{mJ}$ pulses with sub-$4\,\mathrm{fs}$ pulse duration with a stabilized CEP [124]. The output pulses of the hollow core fibre compressor are sent into the attosecond beamline similar to the setup described in 3.7.2 starting with high harmonic generation in neon, spectral and spatial filtering by a Kapton/Zr filter and an iris aperture, a refocussing two part mirror and an electron time-of-flight (TOF) spectrometer [125]. The high harmonic spectrum is characterised with a grating-spectrometer. The samples, the two part mirror, and the time of flight spectrometer

are mounted in an experimental chamber, providing ultra-high vacuum conditions (base pressure $< 3 \times 10^9\,\mathrm{mbar}$). For refocusing with the two-part mirror, similar to the one described in [15], a Molybdenum-Silicon (MoSi) multilayer mirror with $8\,\mathrm{eV}$ bandwidth at a peak reflectivity at $93\,\mathrm{eV}$ is used together with a NIR mirror in the outer part. With this setup isolated attosecond pulses with a duration of $(248 \pm 15)\,\mathrm{as}$ are achieved. The intensity in the focus is attenuated to $6 \times 10^9\,\mathrm{W/cm^2}$ for the gold measurements and to $1.3 \times 10^{10}\,\mathrm{W/cm^2}$ for the tungsten measurements to prevent sample damage due to melting [126]. In this intensity regime photoemission of the XUV pulse is much stronger than above threshold photoemission from the NIR pulse. The time delay between the two pulses is introduced with a piezo stage (P-753 LISA Piezo NanoAutomation Stage, Physik Instrumente) with $10\,\mathrm{as}$ resolution. The photoelectrons are collected with a TOF spectrometer with a collection angle of $4.8°$ and an energy resolution of $\delta E/E \simeq 0.004$ similar to [127].

5.3. Photoelectron transport in gold

5.3.1. Sample characterisation

For the streaking experiments, a thin gold film of $52\,\mathrm{nm}$ is deposited on a silicon (100) substrate by D. Lei (The Hong Kong Polytechnic University, Hong Kong). After preparation the sample was stored and transported under ambient conditions until the characterisation and the streaking experiments were performed.

The samples were characterised for their surface contamination and chemical composition by X-ray photoelectron spectroscopy (XPS) (SPECS Mg Kα X-ray source, Phoibos 150 hemispherical analyser), crystalline structure by X-ray diffraction (XRD)(Rigaku SmartLab), and surface topology by atomic force microscopy (AFM) (Veeco Dimension Icon). The XPS, and XRD measurements have been performed in coorporation with S. Stakov, A. Seiler, and S. Ibrahimkutty (Karlsruhe Institute of Technology). AFM measurements in collaboration with M. Barthelmess (DESY/CFEL, Hamburg). The data analysis was performed with CasaXPS (Casa Software Ltd.) and Gwyddion (D. Necas and Petr Klapetek, Departement of Nanometrology, Czech Republic: [128]).

The characterisations by XPS and XRD are shown in Figure 5.1. The XPS spectrum is calibrated using the position of the $C\,1s$ peak located at $285\,\mathrm{eV}$ [65]. An overview together with the elementary peak positions proves the presence of metallic gold with unshifted peaks of $Au\,4p$, $Au\,4d$, $Au\,4f$ and $Au\,3p$. The peaks of oxygen $O\,1s$ and carbon $C\,1s$ are attributed to surface contamination proving the chemical impureness. The XRD measurement shows the diffraction peaks from the single-crystalline silicon substrate and several diffraction peaks of different crystal orientations of gold, meaning that the gold film is poly-crystalline. Peaks of different crystalline orientations of gold are found with a dominant Au(111) orientation but also (200), (220) and (311) peaks are present. The broadening of the peaks is another indicator for the poly-crystalline structure. The sharp Si (200) and (400) peaks are resulting from the single crystalline substrate. The sample is characterised by AFM to investigate the surface topology and roughness of the sample. The measurements show that during growth small discs were formed. In Figure 5.2 a $1\,\mu\mathrm{m}^2$ area of the gold film is shown together with an analysis of the small discs (marked with blue lines). An individual analysis of several discs

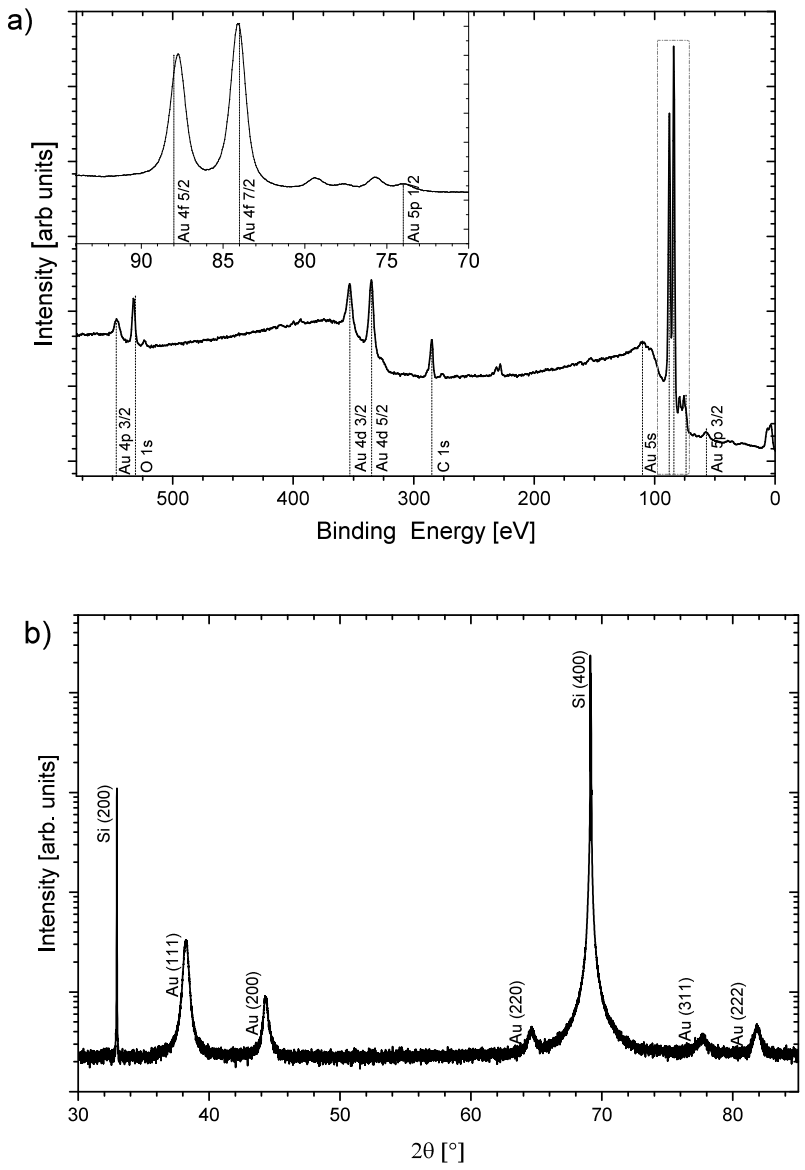

Figure 5.1.: XPS a) and XRD b) of $52\,\mathrm{nm}$ thin gold film on silicon (100) substrate. [22]

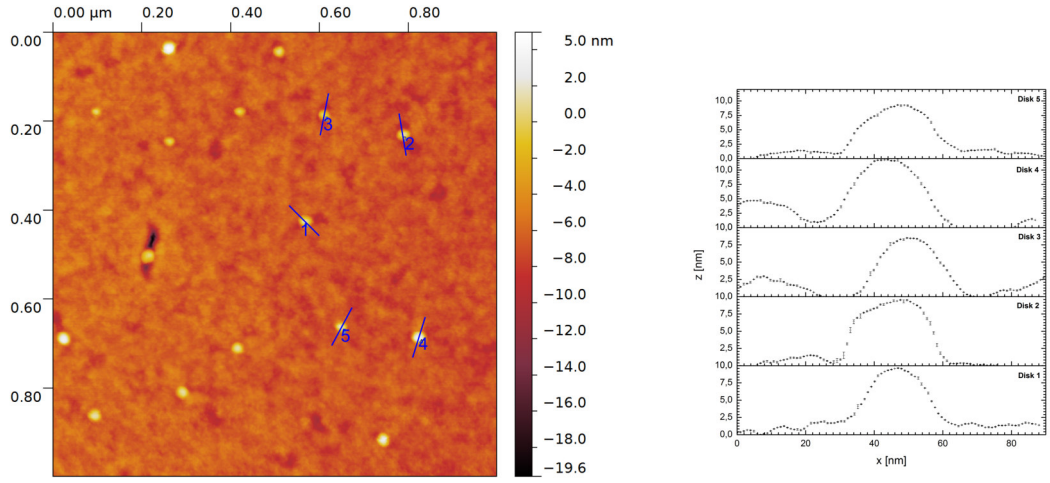

Figure 5.2.: AFM of $52\,\mathrm{nm}$ thin gold film on silicon (100) substrate with line scans of disks. [22]

leads to diameters of $20\,\mathrm{nm}$ to $30\,\mathrm{nm}$ and heights of $5\,\mathrm{nm}$ to $10\,\mathrm{nm}$. The average surface roughness is calculated with the open source program Gwyddion [128] and is $(0.7 \pm 0.2)\,\mathrm{nm}$. The spacing of the discs is $150\,\mathrm{nm}$ to $300\,\mathrm{nm}$. In the measurement range of $1\,\mu\mathrm{m} \times 1\,\mu\mathrm{m}$ we foundnd 16 discs. An XUV beam focus with a typical focus size of $1\,\mu\mathrm{m}$ to $2\,\mu\mathrm{m}$ would cover 50 to 100 discs. On the basis of the characterizations above we conclude, that the sample is a surface contaminated poly-crystalline metallic film with randomly distributed gold discs resulting from film growth.

5.3.2. Attosecond streaking on gold

The attosecond streaking was performed with sub-$4\,\mathrm{fs}$ NIR pulses with an intensity of $6 \times 10^9\,\mathrm{W/cm^2}$ and XUV attosecond pulses with a duration of $(248 \pm 15)\,\mathrm{as}$ centred around $93\,\mathrm{eV}$ as described in 5.2. The results of the streaking experiments are shown in Figure 5.3. In (a) the valence band photoelectron spectrum generated with the HHG XUV pulse of Au is displayed. The raw data of the Au valence band are outlined in black. Fourier filtering smooths the spectrum by suppressing frequency components resulting from the background (red line). The secondary electron background (see Section 3.7.1) is corrected by subtracting a Shirley background [129] (dashed black line). The final spectrum is shown in blue. After correction and filtering the valence band spectrum is clearly visible bearing a peak around $83\,\mathrm{eV}$. The attosecond streaking trace in (b) is acquired with delay steps of $300\,\mathrm{as}$ and an integration time of $40\,\mathrm{s}$ corresponding to 4×10^4 laser pulses and subsequent filtering and background subtraction. The time delay range is longer than the streaking NIR pulse duration and resolves the oscillation of the electric field in the pulse. Applying the FROG-CRAB (frequency resolved optical gating for complete reconstruction of attosecond bursts) technique [130] and performing a principal components generalized projections algorithm (PCGPA) [131] one can retrieve the photoelectron wavepacket in c). Since the signal-to-noise ratio

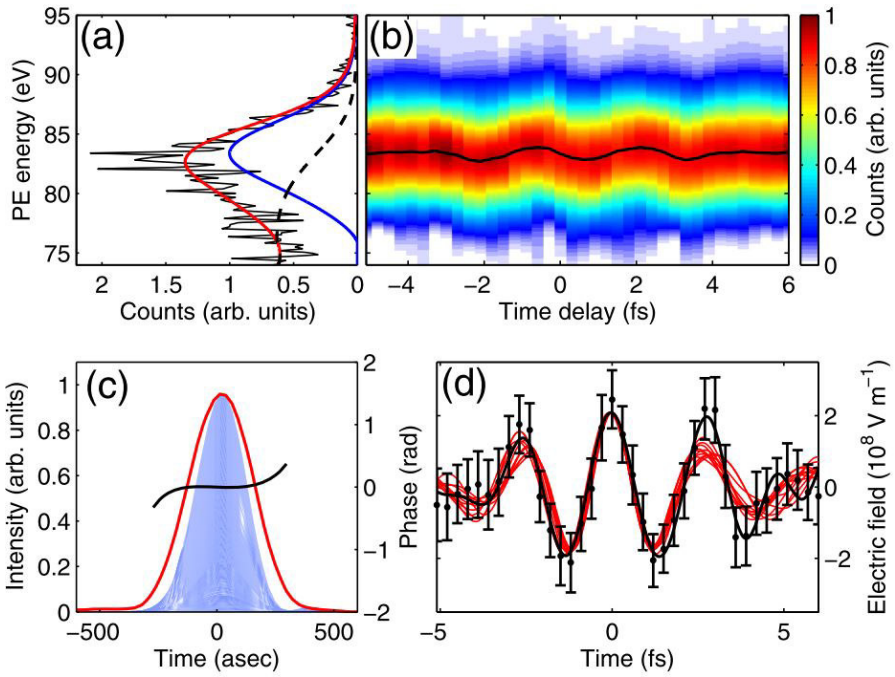

Figure 5.3.: Attosecond streaking results on gold film: (a) shows the raw data (black line), Fourier filtered signal (red line), a Shirlay background (black dashed line), and the Fourier filtered and background corrected data (blue line). The filtered and background corrected streaking trace is displayed with time steps of $300\,\mathrm{as}$. In (c) the temporal amplitude and phase are presented resulting in a temporal broadening of the photoelectron wavepacket to $319^{+43}_{-37}\,\mathrm{as}$. The retrieved electric field at the sample surface (black line) is shown in (d) together with previous gas phase measurements (red line). [22]

is lowest in the extrema, the regions around were used for the analysis. For the analysis, different window sizes around these maxima were used for the retrieval resulting in slightly different wavepacket durations. The median of the retrieved values was taken as overall duration. The error is estimated from the spread of the retrieved values. The amplitude and phase of the retrieved photoelectron wavepacket are plotted in red and black, respectively. The amplitude is broadened in comparison to the Fourier limited wavepacket (shaded area) resulting from the higher order phase distortion. The duration of the photoelectron wavepacket is $319^{+43}_{-37}\,\mathrm{as}$.

For retrieving the central energy E_{COM} and its error of the Fourier filtered and background subtracted streaking trace a center of mass analysis is performed as described in [107]. The energy shift of $\Delta E = E_{COM} - E_i$ with the initial photoelectron energy W_i is correlated to the instantaneous vector potential $\mathbf{A}$ of the streaking field by [29]

$$\mathbf{A} = \sqrt{\frac{m_e}{2E_i}}\frac{\Delta E}{\cos\theta}\mathbf{A}_L \tag{5.1}$$

with the polarization vector $\mathbf{A}_L$ of the streaking field and the angle θ between the polarization vector and the initial photoelectron velocity. From the vector potential $\mathbf{A}$ the electric field can be calculated with the relation $\mathbf{E} = \partial\mathbf{A}/\partial t$. The retrieved electric field at the sample surface is presented in (d) together with several neon gas phase experiments. The curve of the gold streaking (black line) and the gas phase streaking experiments in neon (red lines) are in good agreement within the errorbars.

5.3.3. Plasmonic evidence in streaking trace

The streaking measurement data of the sample presented in Section 5.3.2 is analysed further in the region outside the XUV-NIR overlap. Figure 5.4 depicts the electric field of the streaking trace extended to time delays much longer than the NIR pulse duration $-10\,\mathrm{fs}$ to $25\,\mathrm{fs}$. The red and shaded curve represent the electric field as retrieved from the streaking trace (line) with its errors (shaded area). The dashed blue line depicts a comparable gas phase streaking measurement in neon. For comparison, the gas phase streaking amplitude is scaled to the Gold sample peak streaking amplitude. The error bar of the retrieved electric field from the gas phase streaking is shown at the first data point. In the region of 'XUV first' (negative time delay) both retrieved fields are overlapping. In the overlapping region the two field curves are almost identical. Focusing on the region of $5\,\mathrm{fs}$ to $10\,\mathrm{fs}$ where the NIR pulse arrives first at the sample followed by the XUV pulse, one observes a significant deviation of the two curves. The field amplitude in gas phase streaking has reduced since the streaking field of the NIR pulse not present in the interaction area. In the gold sample, the retrieved field rises again. Additionally, the amplitude increases with a delay of $20\,\mathrm{fs}$ after time zero. This remarkable deviation of the two measurements are a possible evidence of plasmonic contributions to attosecond streaking. However, the differentiation between the electric field of a surface plasmon and the incident laser field is difficult. For this sample category the adapted setup of attosecond photoscopy, as described in section 3.7.4 would be beneficial and allows the distinction between laser and plasmonic field contributions.

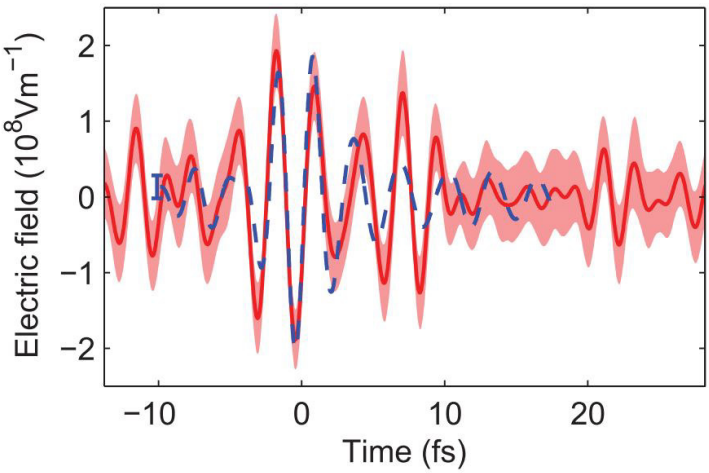

Figure 5.4.: Streaking of the gold sample for very long time delays between the XUV and NIR pulses showing a significant deviation from gas phase measurements (dottet line) at delays longer than $10\,\mathrm{fs}$. [123]

5.4. Photoelectron transport in tungsten trioxide

5.4.1. Sample Characterisation

The tungsten sample is produced by sputtering $20\,\mathrm{nm}$ of tungsten onto a silicon (100) substrate by J. Overbuschmann (CAESAR, Bonn). After preparation the sample is stored under ambient conditions and the upper layers oxidise naturally to WO_3. The sample is characterised with the same methods as the gold sample above. The XPS and XRD characterisations are presented in Figure 5.5. The XPS spectrum in a) is calibrated using the position of the $C\,1s$ peak located at $285\,\mathrm{eV}$ again [65]. The tungsten peaks of $W\,4p$, $W\,4d$, and $W\,4f$ are indicated together with the $C\,1s$, and $O\,1s$ peaks [65]. The $C\,1s$, and $O\,1s$ peaks are originating from surface contamination as on the gold sample. Focusing on the $W\,4f$ peak region in detail in the inset, one finds two prominent peaks and a substructure. The two prominent peaks are shifted with $4.7\,\mathrm{eV}$ from $31.7\,\mathrm{eV}$ to $36.4\,\mathrm{eV}$ in perfect agreement with the chemical shift expected by oxidation to WO_3 [65]. The minor peaks in the region of $30.5\,\mathrm{eV}$ to $31.5\,\mathrm{eV}$ BE belong to pure tungsten. *Carlson et al.* studied the peak intensity ratio of the $4f$ peaks for WO_3 films of different thickness on W [132]. An overview over the photoelectron spectra for different thickness of WO_3 and a relation between the peak intensity ratios of the $4f\,7/2$ and the WO_3 film thickness is illustrated in Figure 5.6. Comparing the peak intensity ratios after subtracting a Shirley background (calculated with of CasaXPS) one can estimate the thickness of the WO_3 layer to $8.5\,\mathrm{nm}$ [132]:

$$A_{W4f}/A_{WO_34f} = 450/7570 = 0.059 \widehat{=} 8.5\,\mathrm{nm} \tag{5.2}$$

The XRD measurements of the WO_3 film are shown in Figure 5.5 b) together with the measurement of the pure substrate. Both measurements show narrow peaks originating from the single crystalline silicon (100) substrate. No characteristic peaks from WO_3 or W are present. The inset of $23° < 2\theta < 26°$ displays the region where WO_3 peaks should appear [133] proving that the sample is amorphous without any crystalline order. The surface topology is shown with AFM in Figure 5.7. The average roughness of the sample surface is calculated to $6.5\,\mathrm{nm}$ corresponding to several monolayers of WO_3 (lattice parameters of monoclinic WO_3: $a = 5.3\,\text{Å}$, $b = 7.2\,\text{Å}$, $c = 7.7\,\text{Å}$). Concluding, the sample consists of an $8.5\,\mathrm{nm}$ rough amorphous WO_3 layer on an amorphous tungsten layer.

5.4.2. Attosecond streaking on tungsten trioxide

The attosecond streaking was performed with sub-$4\,\mathrm{fs}$ NIR pulses with an intensity of $1.3 \times 10^{10}\,\mathrm{W/cm^2}$ and and high harmonic generated attosecond pulses with a duration of $(248 \pm 15)\,\mathrm{as}$ centred around $93\,\mathrm{eV}$ as described in 5.2. The attosecond streaking results are presented in Figure 5.8. First the photoelectron spectrum of the film is measured of the electrons emitted from the XUV pulse (a). The raw data (black line) is Fourier filtered (red line) and a Shirley background (black dashed line) is subtracted (blue line). After data processing the spectrum is smooth and resolves clearly the valence band peak located at $84\,\mathrm{eV}$. (b) shows the filtered and background subtracted streaking trace with the modulation of the streaking NIR field for a relative time delay of more than $\pm 5\,\mathrm{fs}$ covering the full NIR

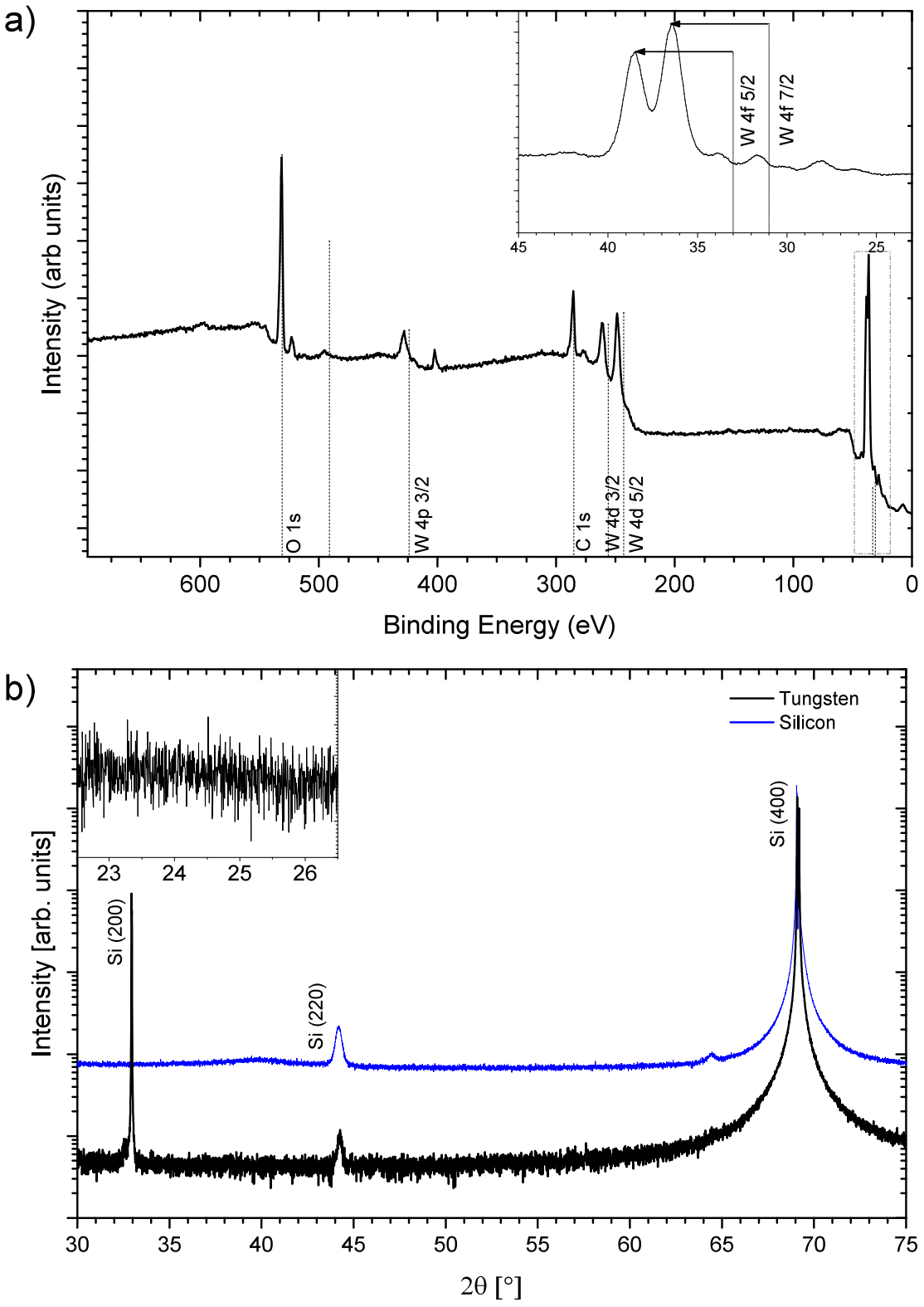

Figure 5.5.: XPS a) and XRD b) of $20\,\mathrm{nm}$ oxidized tungsten film on a silicon (100) substrate. [22]

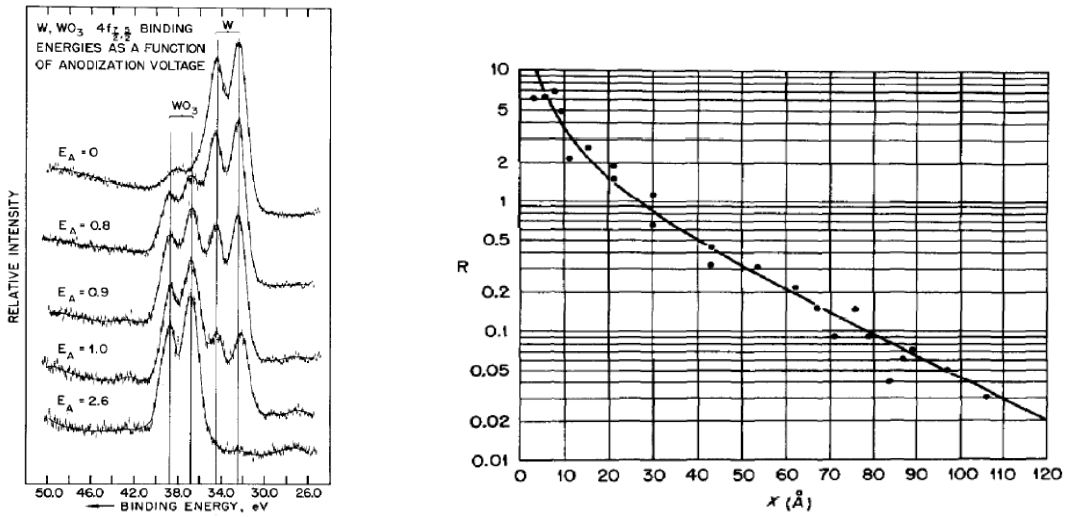

Figure 5.6.: Photoelectron spectra of different thickness of WO_3 on W (left) and correlation of peak area ratio of $W\,4f\,7/2$ and $WO_3\,4f\,7/2$. [132]

streaking pulse duration. The retrieved photoelectron wavepacket from FROG-CRAB and PCGPA (described in more detail in Section 5.3) is illustrated in (c) together with a Fourier limited wavepacket. The phase of the photoelectron wavepacket is symmetrically changing leading to a symmetric temporal broadening. The photoelectron wavepacket duration is determined to be $359^{+42}_{-25}\,\mathrm{as}$. (d) presents the retrieved streaking field in comparison to gas phase measurements. A good agreement within the errorbars is observed.

5.5. Origin of the temporal broadening

The first attosecond streaking experiment on a solid was done on a tungsten crystal [107]. They found an arrival delay in the emission of photoelectrons from the $4f$ and the valence band of $(110 \pm 70)\,\mathrm{as}$. Experiments on bulk magnesium (30 monolayers) [20] surprisingly show, that the $2p$ and the valence band electrons are emitted almost at the same time without any delay. The influence of crystalline adlayers of magnesium on crystalline tungsten to the time delay between the instantaneous $2p$ magnesium photoelectrons and $4f$ tungsten electrons was investigated [21]. The delay depends on the number of monolayers deposited on the tungsten crystal and raises from $80\,\mathrm{as}$ for one monolayer to more than $200\,\mathrm{as}$ for four monolayers. Also the time delay of the magnesium $2s$ and the conduction band electrons is investigated in this study. The delay first rises with the number of monolayers reaching a maximum of $60\,\mathrm{as}$ at three monolayers and then decreases to simultaneous emission. The results from these studies were explained recently [12]. Close to energy gaps an excited photoelectron wavepacket propagate faster than the group velocity because their spectrum still evolves. This process is determined by inelastic scattering processes. The consequence of this is, that photoelectron wavepackets originating from deeper layers over-

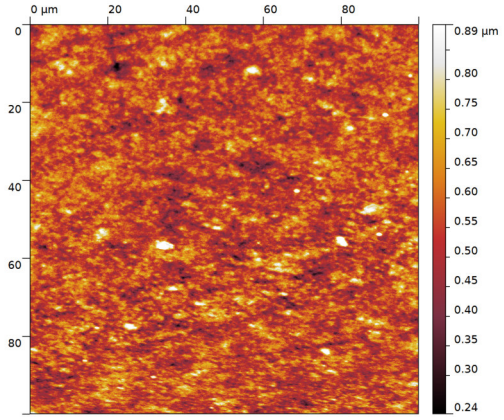

Figure 5.7.: AFM of $20\,\mathrm{nm}$ thin WO_3 on W film on silicon (100) substrate. [22]

take the photoelectron wavepackets originating from top layers. The energy band where the photoelectron wavepacket originates from influences the group velocity of the propagating electron wavepacket. This leads to the temporal delay of the $4f$ and valence band electrons in photoemission in the tungsten case. Whereas, in the magnesium case, it leads to simultaneous emission of the core level $2p$ and valence band electrons.

The experiments presented above on gold and tungsten trioxide surface reveal photoelectron wavepacket durations of $319^{+43}_{-37}\,\mathrm{as}$ for the gold $4f$ emission and $359^{+42}_{-25}\,\mathrm{as}$ for the tungsten valence band. If one compares the photoelectron wavepacket durations and the XUV pulse duration of $(248 \pm 15)\,\mathrm{as}$ in the streaking experiments described above significant deviations in both samples are found. These are resulting from the origin of the photoelectrons within the inelastic mean free path [13].

$$\Delta\tau = \lambda\sqrt{m_e/2E} \tag{5.3}$$

with the mean free path λ, and the photoelectron energy E. The mean photoelectron energy in this experiment is $84\,\mathrm{eV}$ and the mean free path can be calculated to $3.9\,\text{Å}$ by using the Tanuma, Powell, and Penn (TPP-2M) formula from Equation 3.23. With Equation 5.3 the resulting broadening of the photoelectron wavepacket for gold is calculated to $71^{+58}_{-54}\,\mathrm{as}$. This calculation satisfies the broadening of the photoelectron wavepacket of gold of $71\,\mathrm{as}$. The mean free path in tungsten trioxide is calculated to $4.9\,\text{Å}$ and the temporal spread of emission time according to Equation 5.3 of tungsten trioxide is calculated to be $90\,\mathrm{as}$. Comparing the measured broadening of $111^{+57}_{-40}\,\mathrm{as}$ and the calculated broadening one finds an agreement within the experimental error.

The physical processes explaining the broadening have different origins. The streaking method itself causes an intrinsic broadening due to the photoemission with an electric quasi-dc field from the NIR laser pulse [29, 105]. At the inflexion points the vector potential equals zero. Therefore the electron wavepacket is not influenced and the wavepacket corresponds to the field-free case. When the NIR field reaches a maximum or minimum, the vector potential is also maximised. Then the streaking amplitude is broadened. Since the FROG-

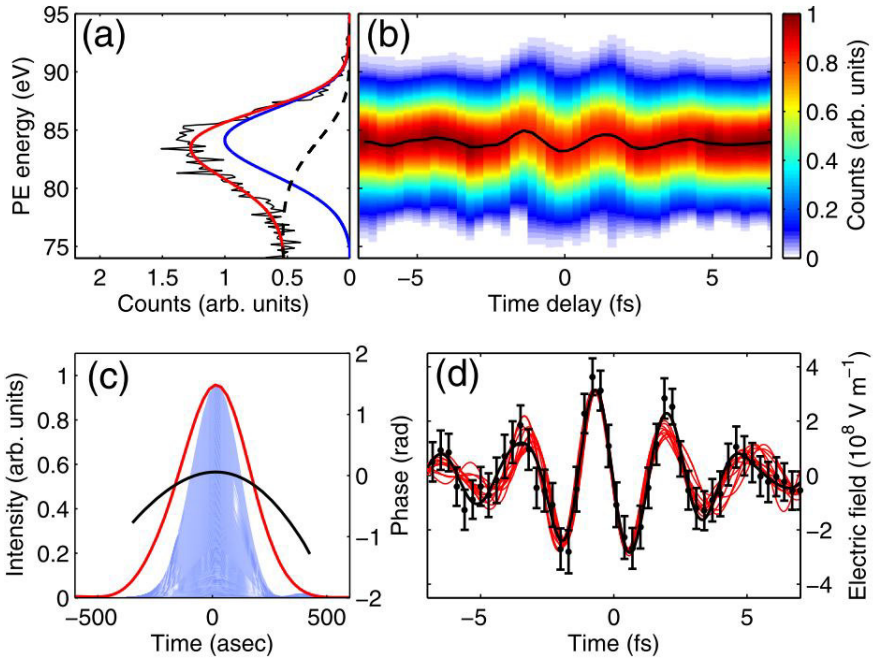

Figure 5.8.: Results of WO_3 Streaking: (a) XUV photoelectron spectrum, (b) full streaking trace of the conduction band, (c) FROG-CRAB and PCGPA retrieved wavepacket, (d) comparison with gas phase streaking. [22]

Crap analysis was performed at these extrema, this significantly influences the wavepacket duration.

The screening of the NIR laser pulse at the sample is a problem that arose with the investigation of solid samples with attosecond streaking. In the gold and tungsten experiments we assumed that photoelectrons feel the electric field only after their propagation to the surface, i.e. the NIR field is perfectly screened at the surface. However, in reality the light field penetrates the sample, since the incidence angle usually is chosen to equal the Brewster angle to reach total absorption and avoid standing surface waves. Furthermore, parts of the reflected light would interfere with the incident light and complicate the streaking field. When the electric field is absorbed by the sample, the photoelectrons experience the field already inside the sample and not only after leaving the surface. When it is assumed, that the field is not screened at the surface all photoelectrons independently from their emission depth experience the same light field. On the other hand, as in our case, a perfectly screened electric field on the surface leads to different streaking fields for the photoelectrons depending on their emission depth. Electrons emitted deeper have a longer propagation time: electrons with $80\,\mathrm{eV}$ from a $10\,\text{Å}$ depth need about $200\,\mathrm{as}$ to leave the surface. During this time the electric laser field changes: one optical cycle of a $5\,\mathrm{fs}$ few cycle pulse needs about $2\,\mathrm{fs}$. A $200\,\mathrm{as}$ emission time window depicts a tenth of a cycle. This can either lead to a compression (emission on rising slope), an extension (emission on falling slope), or a symmetric broadening (extrema).

Neppl et al. investigated the effect of screening on several monolayers of magnesium on a tungsten single crystal [21] finding out that the streaking delay of the $W\,4f$ band rises for a growing number of the covering magnesium monolayers. The longer penetration depth of the NIR field equalizes the absolute time when photoelectrons experience the laser electric field. The screening depth therefore influences the broadening of photoelectron wavepackets due to different emission depths. The deeper the NIR field penetrates the surface the less the photoelectron wavepacket gets broadened from the quasi-dc field. The interaction of the photoelectron wavepacket with the crystal structure or electron correlations can result in additional broadening of the wavepacket. More effects the photoelectron wavepacket is affected to during the transport to the surface are interband transitions, scattering from defects, steps, or phonons.

Another effect that results in a broadening is the specific group velocity depending on the energy band and the emission position inside the crystal as reported from the experiments on tungsten and magnesium above [12, 20, 21, 107]. Here, the gold sample was polycrystalline, but within its crystalline zones the same effects on the group velocities occur. However, different crystalline orientations lead to a perturbation and stretch the window of escape times. The tungsten trioxide sample was amorphous. Therefore, the escape time window is even more stretched which leads to a further broadening of the photoelectron wavepacket.

Plasmonic effects as inter- and intraband plasmons or the enhancement of a surface plasmon are another reason for a broadening of the photoelectron wavepacket [14]. The emitted photoelectron leaves a hole in the electronic structure. Subsequently the environment will react to refill the hole. This rearrangement of charges happens on the attosecond time scale up to some $10\,\mathrm{fs}$ (Auger processes) or even longer (radiative decay). This processes are strongly dependent from the band structure of the sample. The system reacting to the created hole excites surface plasmon modes or interband plasmons that affect the photoelectrons that are still propagating in the material and leave later than initially created electrons. The creation of surface plasmon modes in the investigated gold sample is likely to appear. In the tungsten trioxide sample interband transitions are likely to appear. The inter- and intraband transitions in WO_3 and W were investigated by *Dietz et al.* already in 1978 [53]. Whereas intraband transitions in the conduction band occur on single crystalline W(100) surface, they are not existing on WO_3 surfaces, but interband transitions from the valence band are persisting in the WO_3 case. The energy loss resulting from the interband transitions is higher compared to intraband transitions. The appearance of intraband plasmons depends strongly from the electron density, that is lower in the oxidized film and rises during reduction. The sample we investigated has an oxidation layer on metallic tungsten. Therefore, the electron density is lower in the oxidation layer than in the underlying metal film. This results only in interband transitions occuring within the measurement range of the mean free path. Thus, further broadening of the photoelectron wavepacket emitted by the attosecond XUV pulse is dominated by interband transition in WO_3 with a lifetime of $1.9\,\mathrm{fs}$ [53].

5.6. Cleaning strategy for nanostructured surfaces

Although it has been demonstrated in Section 5.3, that streaking from contaminated surfaces is possible, UHV prepared samples would improve the photoelectron signal especially for nanostructures, since the sample to background ratio is very weak due to the small sample area compared to the substrate background. For the development of a cleaning strategy a sample is prepared by self-assembling of $8\,\mathrm{nm}$ gold spheres in solution at the liquid-air interface and the deposition on a silicon substrate (sample preparation by Peter Siffalovic, Bratislava). After preparation the sample was transferred under ambient conditions for characterisation and UHV preparation of a clean surface. The sample is characterised before to the cleaning procedure in terms of surface morphology by AFM, previous, during and after the cleaning in terms of the chemical composition by XPS, after the cleaning procedure it is analysed by SEM to investigate the surface morphology.

The AFM image in Figure 5.9 is taken before the cleaning procedure and illustrates the surface in more detail. A line scan through four spheres arranged in a line shows the close-packing of the spheres with a distance of $8.1\,\mathrm{nm}$.

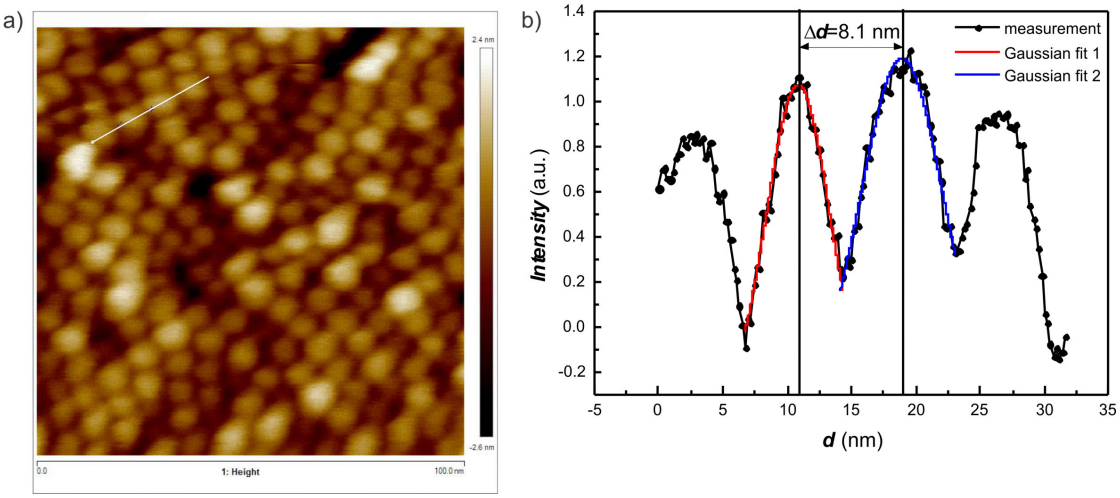

Figure 5.9.: AFM (a) and line scan (b) before the cleaning procedure to characterise the surface topology.

The nanosphere sample is then cleaned under UV-Ozone atmosphere with a commercial UV-Ozone Cleaner (ProCleaner, Bioforce Nanoscience) in two cycles of $30\,\mathrm{min}$ each. After both cleaning cycles and after some relaxation time of $100\,\mathrm{hrs}$ the surface chemical purity is investigated with XPS. The spectra are shown in 5.10.

By analysing three peak regions, $Au\,4f$, $C\,1s$ and $O\,1s$ we deduce from the presence of metallic gold, the existence of surface contamination, and of higher oxidation states. Before the cleaning procedure we find pronounced $Au\,4f$ and $C\,1s$ peaks resulting from the metallic gold spheres and surface contamination and a small contribution of oxygen. Then the sample is cleaned and afterwards the $Au\,4f$ and $O\,1s$ peaks sharpen and increase, whereas the $C\,1s$ peak decreases. This behaviour is an indication for the removal of organic contamination of

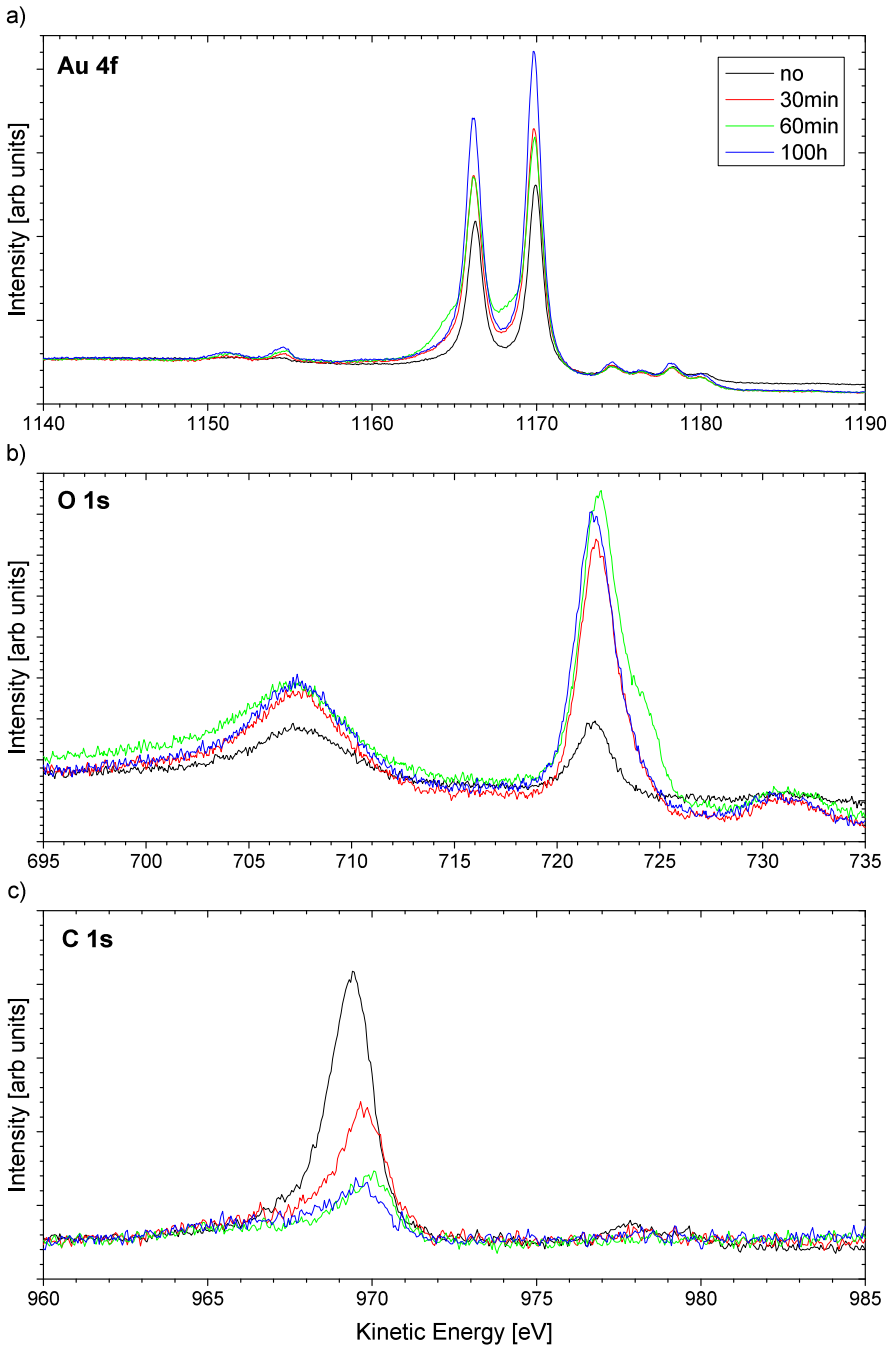

Figure 5.10.: XPS spectra in three peak regions $Au\,4f$, $C\,1s$ and $O\,1s$ before, during, directly after the two cleaning steps and after some relaxation time.

the surface leading to a clearer and more intense gold signal. The adsorption of O^* during the cleaning procedure leads to a pronounced oxygen peak. Applying a second cleaning cycle of another $30\,\mathrm{min}$ leads to further decrease of the $C\,1$ peak demonstrating further cleaning of the sample surface. The rising shoulder of the metal gold and oxygen peak resulting from the higher oxidation state proves the oxidation of the metal gold (investigated in more detail in [134]) that reverses after some relaxation time of $100\,\mathrm{h}$ resulting in an even more pronounced metal gold peak. The XPS studies demonstrate the successful application of UV-Ozone cleaning as a structure preserving cleaning technique proven by the SEM measurements after the cleaning is verified.

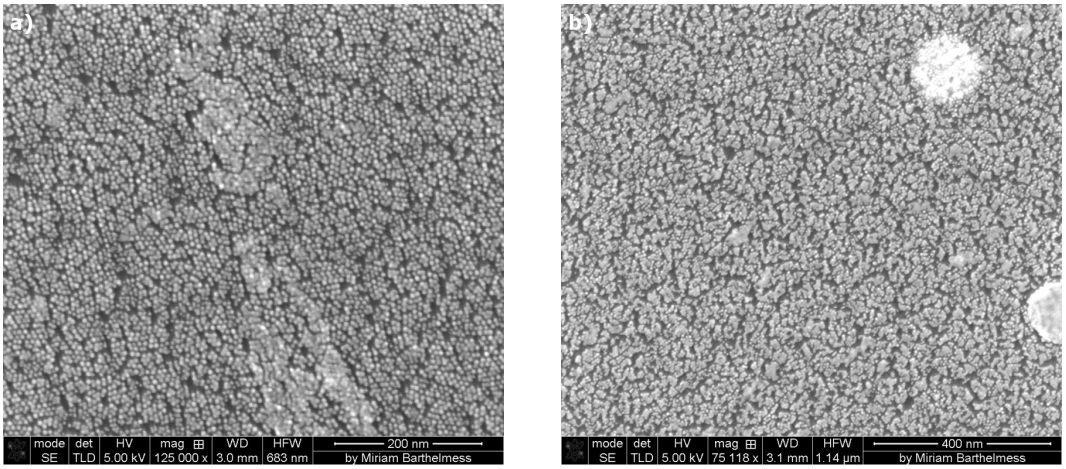

Figure 5.11.: SEM images taken after the UV-Ozone cleaning procedure (left) and after heating the sample to $50\,^{\circ}\mathrm{C}$.

After the cleaning procedure and the relaxation time a SEM image were taken (illustrated in Fig 5.11) and reveal the present close-pack assembly of the gold nanospheres in agglomerates. An analysis of the agglomerates show a diameter of approximately $95\,\mathrm{nm}$. In a close-packed sphere spacing one agglomerate hosts approximately 100 nanoparticles.

To prove that heating as a traditional surface cleaning technique is no alternative the sample is heated up under vacuum atmosphere to $50\,^{\circ}\mathrm{C}$ and cooled down at room temperature. Afterwards the surface is imaged in b), which illustrates the melting of the single spheres to a branching pattern even at moderate temperatures increasing preferably the surface mobility.

6. Scattering of broadband laser pulses at triple layer samples

6.1. Sample preparation and characterisation

Triple layer thin film samples as the basis to manufacture nano sandwich resonators described in Section 4 were produced by sputter coating thin gold and tungsten layers on single crystalline silicon wafers with different gold layer thicknesses (F. Segerink, University of Twente, The Netherlands). In a second step a top coating layer of different materials is sputtered (Leica EM ACE6009). In Table 6.1 an overview of the triple layer films is given.

Sample No	Layer 1	Layer 2	Layer 3
1	10 nm Au	15 nm SiO2	10 nm Au
2	20 nm Au	15 nm SiO2	10 nm Au
3	30 nm Au	15 nm SiO2	10 nm Au
4	50 nm Au	15 nm SiO2	10 nm Au
5	10 nm Au	15 nm SiO2	10 nm 80% Au/20% Pd
6	20 nm Au	15 nm SiO2	10 nm 80% Au/20% Pd
7	30 nm Au	15 nm SiO2	10 nm 80% Au/20% Pd
8	50 nm Au	15 nm SiO2	10 nm 80% Au/20% Pd
9	10 nm Au	15 nm SiO2	10 nm W
10	20 nm Au	15 nm SiO2	10 nm W
11	30 nm Au	15 nm SiO2	10 nm W
12	50 nm Au	15 nm SiO2	10 nm W

Table 6.1.: Triple layer film samples of gold, silica base layers on silicon substrate with additional coating of gold, gold and palladium (80% Au/20% Pd)and tungsten layers.

Prior to scattering measurements the thin films are characterised with AFM and XPS.

The XPS characterisations are conducted for one of each of the top layer materials exemplarily in Figure 6.1. The XPS spectra of the Au and AuPd samples (Sampe 2 and Sample 6) in a) and b), respectively, exhibit peaks at elementary gold and gold and palladium positions. Several spectral lines originating from degenerated energy levels of different gold states are found in both cases. In the AuPd case, spectral lines from palladium are found as expected. The presence of carbon and oxygen surface contaminations is proven by the carbon and oxygen peaks located at $284\,\mathrm{eV}$ and $531\,\mathrm{eV}$, respectively. The spectrum of the tungsten sample (Sample 10) is displayed in c). The tungsten peaks are shifted relative to the elementary

peaks by $4.5\,\mathrm{eV}$. But the elementary peaks are still visible. This shift is in perfect agreement with oxidized tungsten (WO_3) as demonstrated in Section 5.4.1. Also here, from the peak intensity ratio between the oxidized and the elementary peak the thickness of the oxidized layer is estimated. The result for the tungsten sample is, that the tungsten layer is almost fully oxidized.

The roughness of the sample surfaces is characterised by AFM. Images for each sample class are presented in Figure 6.2 together with a roughness analysis. A polynomial background is subtracted and lines are corrected by matching the median height. The RMS roughnesses are calculated several times along a line to extract a mean error. The surface quality is very high with a roughness in the range from $0.06\,\mathrm{nm}$ to $0.17\,\mathrm{nm}$ per sample. The high surface quality is reliable and does not result from a bad quality of the tip, since very small structures can be resolved clearly, which would not be the case for a bad tip. The surface of the gold sample (Sample 1) appears grained in contrast to the palladium (Sample 5) and the tungsten (Sample 9) surface. On the surface of the tungsten sample bigger grains can be found on a smooth background. The grains have a height in the range of $60\,\mathrm{nm}$ to $70\,\mathrm{nm}$. The diameter cannot be determined exactly due to the triangular shape resulting from the convolution of the small particle shape and the tip size leading to the projection of the tip.

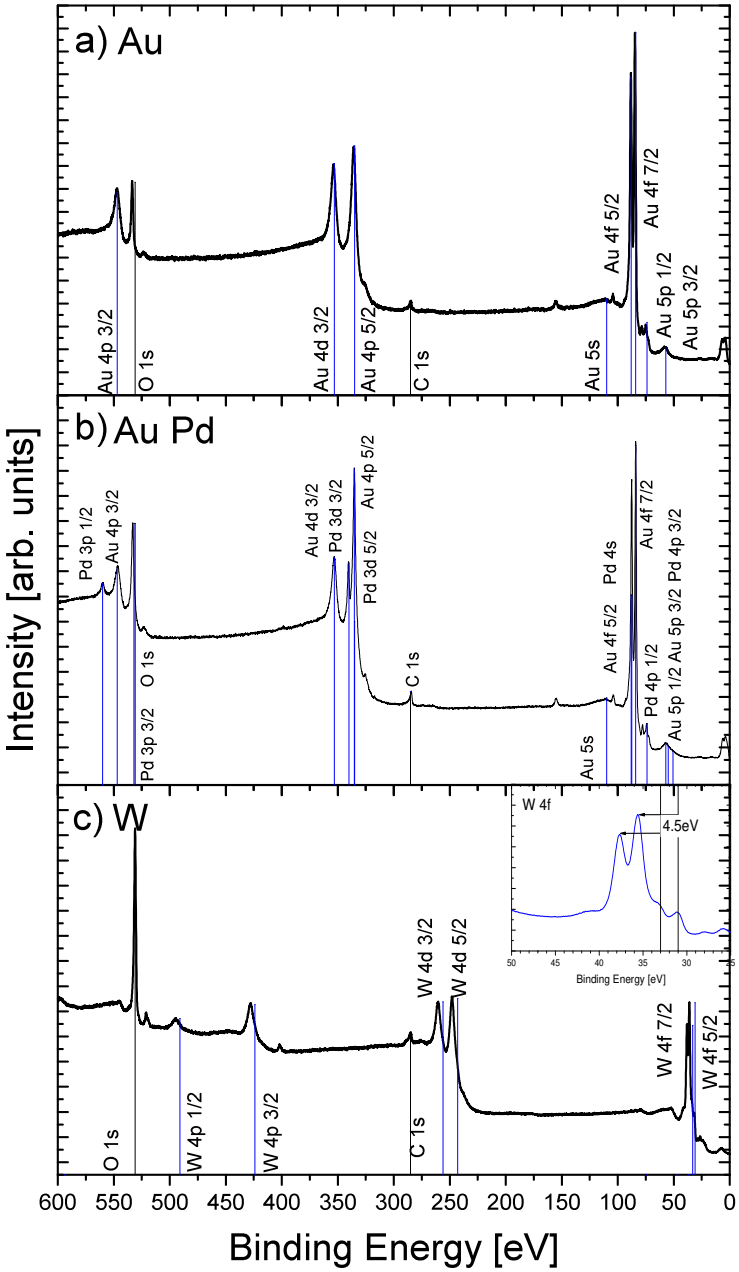

Figure 6.1.: XPS characterisation exemplary for each top layer material: a) Sample 2: Au, b) Sample 6: AuPd, and c) Sample: 10:W.

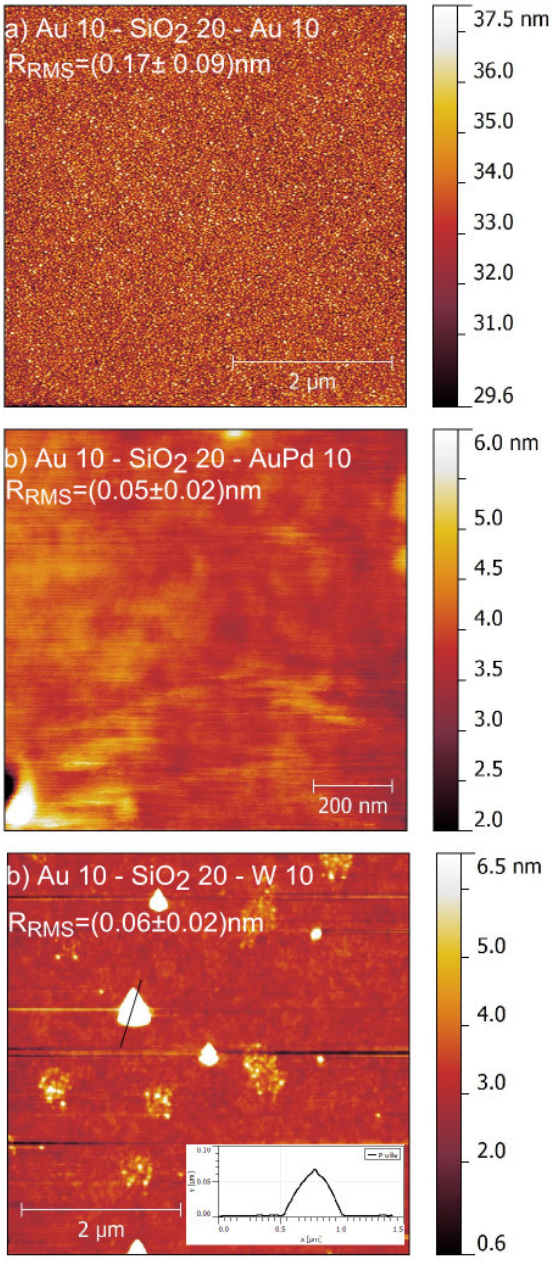

Figure 6.2.: AFM characterisation exemplary for each top layer material: a) Sample 1: Au , b) Sample 5: AuPd, and c) Sample 9: W.

6.2. Scattering experiments

To measure the angular dependent scattering of the thin film samples the setup presented in Figure 6.3 is used. The sample is illuminated with broadband light pulses of the oscillator described in Chapter 7.2 (λ =600 nm to 1000 nm) with an angle of $45°$. The scattered light is collected for different angles with an optical fibre (FC-UVIR400-1, Avantes BV, The Netherlands) and measured with a spectrometer (AvaSpec-ULS2048XL, Avantes BV, The Netherlands). The fibre tip is rotatable around the sample by a rotation stage.

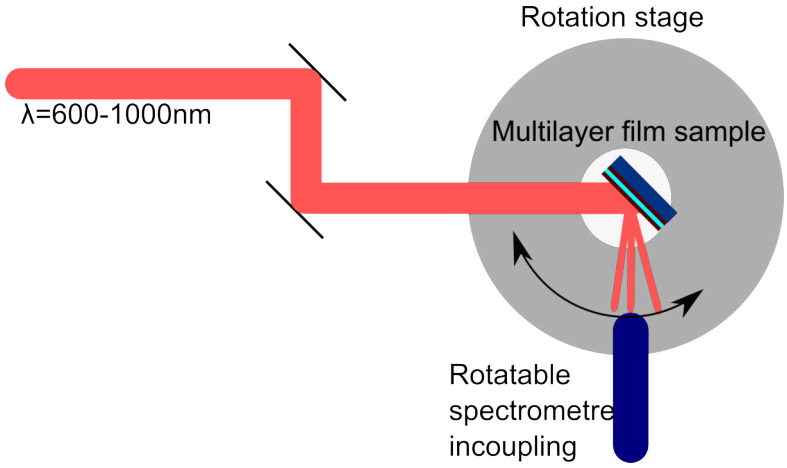

Figure 6.3.: Setup for measuring the scattered spectrum of triple layer film samples.

In a first reflectivity spectra of the directly reflected beam are measured. In Figure 6.4 a) the Fourier filtered spectrum of a single 10 nm gold layer reference is shown. The reflected beam shows the strong modulated oscillator spectrum. The reflectivity of Sample 1, Sample 2, Sample 5 and Sample 10 are normalised to the reference spectrum and Fourier filtered. The plots are presented in b). The reflectivity curves of the four samples look very similar. Small variations can be found in the reflectivity at short wavelength 600 nm to 750 nm where the gold top layer samples have a higher reflectivity compared to the tungsten and gold-palladium top layers. In the long wavelength region from 900 nm to 1000 nm, the samples with 20 nm base layer have a higher reflectivity compared to the samples with 10 nm base layer.

In Figure 6.5 the scattering spectrum of a 10 nm gold film layer used as reference is shown in a). The normalised scattering spectra of four samples are plotted in b). The curves are Fourier filtered additionally. Two samples are of the (10-15-10) run with a top layer of gold-palladium and gold. The other two samples represent the (20-15-10) run with gold and tungsten as top layers. Both samples with a 10 nm bottom layer enhance the scattering relative to the gold layer in contrast to the samples with 20 nm bottom layer. This asymmetry is pronounced at the 640 nm and 720 nm peaks. Furthermore, the structure in the long wavelength region from 800 nm to 900 nm is modulated stronger in the 10 nm bottom layer samples.

Comparing the results from the reflectivity measurements and the scattering measurements, one can conclude that the region of enhanced scattering into $60°$ does not correspond

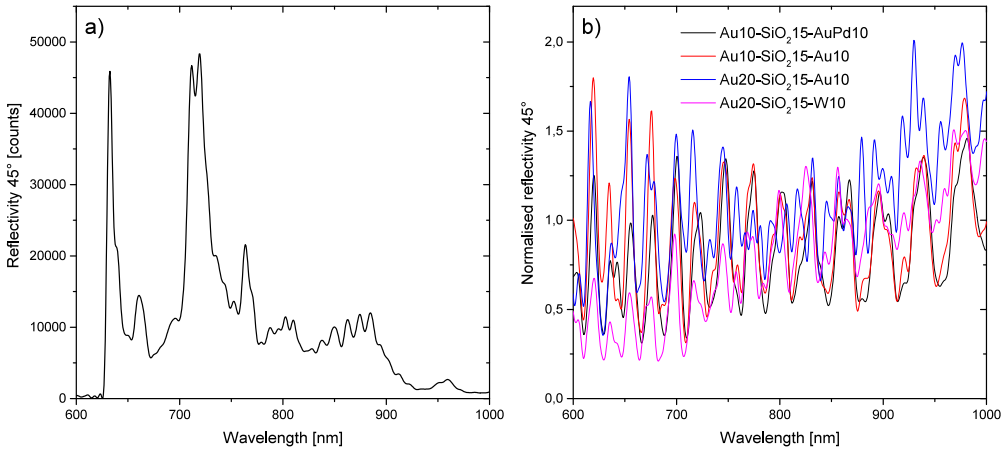

Figure 6.4.: Reflectivity at 45° incidence of a single $10\,\mathrm{nm}$ gold layer as reference a) and normalised reflectivity spectra relative to the gold single layer reference of Sample 1 (Au 10-SiO2 15-Au 10), Sample 2 (Au 20-SiO2 15-Au), Sample 5 (Au 10-SiO2 15-AuPd 10) and Sample 10 (Au 20-SiO2 15-W 10).

to an enhancement in the reflectivity. A weak reflectivity at $710\,\mathrm{nm}$ in the $10\,\mathrm{nm}$ bottom layer Samples 1 and 5 could be attributed to absorption and excitation of a surface plasmon resulting in a enhanced scattering at slightly lower energies explaining the scattering enhancement.

Both plots show very recent results and only a preliminary first characterization to see substantial differences in the optical properties of this type of systems.Further data analysis is ongoing. In the next step the films will be used as base layers for manufacturing disk structures.

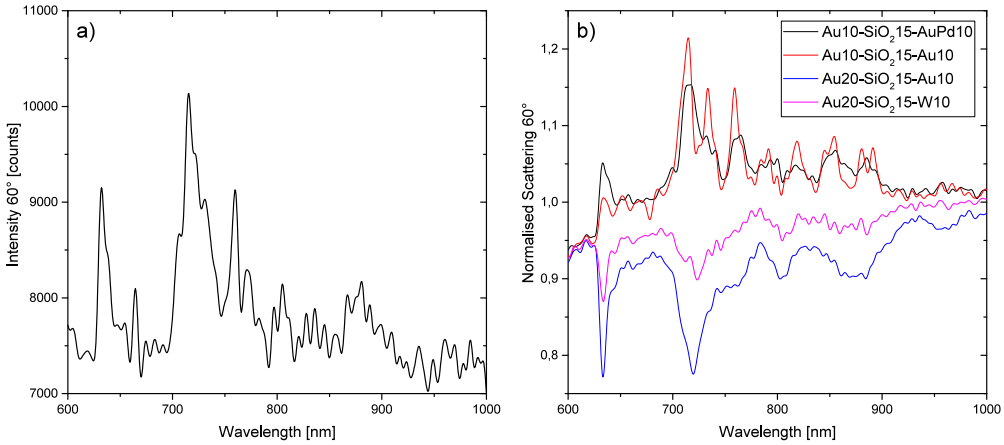

Figure 6.5.: Scattering into $60°$ relative to the surface normal of a single $10\,\mathrm{nm}$ gold layer as reference a) and normalised spectra relative to the gold single layer reference of Sample 1 (Au 10-SiO2 15-Au 10), Sample 2 (Au 20-SiO2 15-Au), Sample 5 (Au 10-SiO2 15-AuPd 10) and Sample 10 (Au 20-SiO2 15-W 10).

7. Beamline

7.1. General

To investigate the plasmonic behaviour of nanostructures with attosecond time resolution a special beamline dedicated for experiments with a high harmonic generation light source on solid samples was built in the framework of this thesis. The general setup is illustrated in Figure 7.1

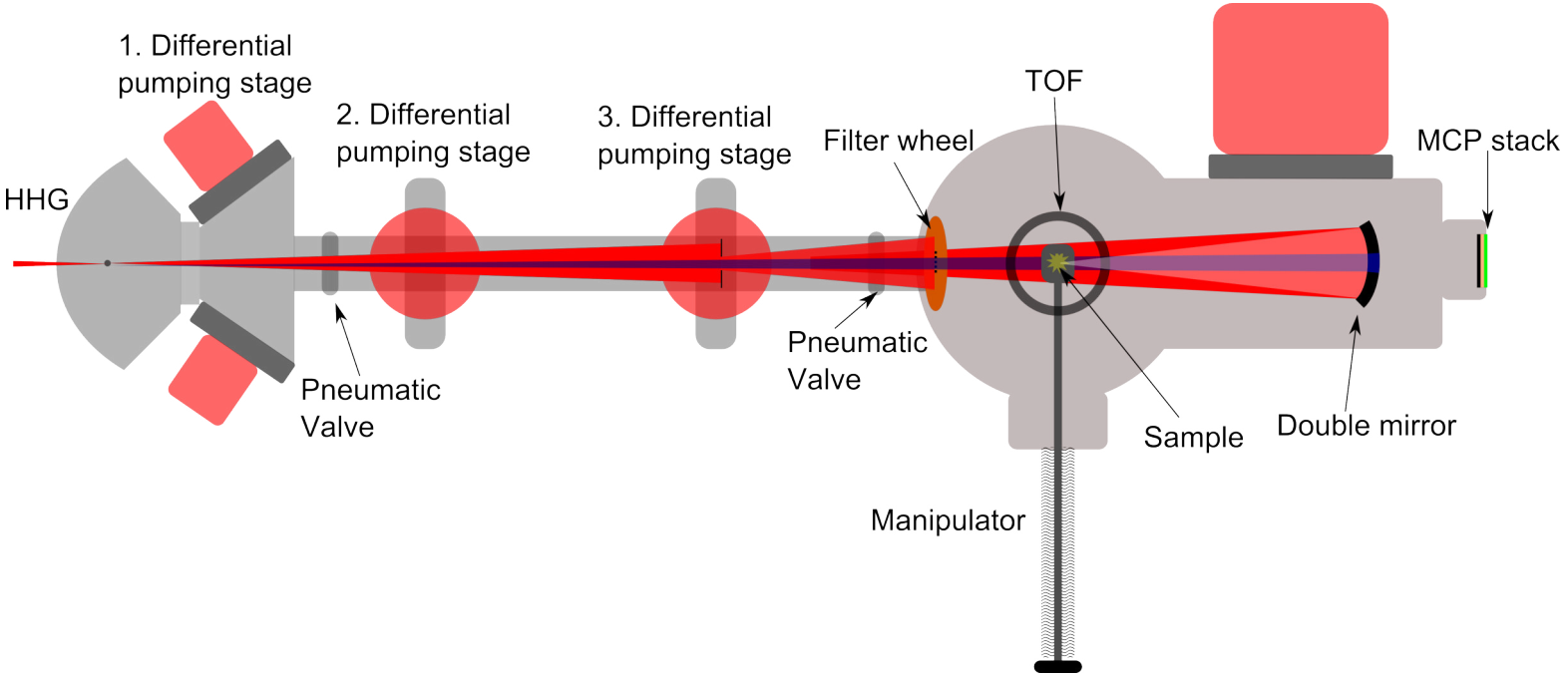

Figure 7.1.: Overview of the attosecond beamline.

and consists of a HHG chamber for the conversion of NIR femtosecond laser pulses to XUV radiation. An experimental chamber consists of the sample holder, a refocusing mirror, some filters, and several detectors for the final experimental requirements. Both chambers need to be connected with vacuum tubes to avoid reabsorption of the XUV radiation in air. Another important requirement is the isolation of the optical parts and the sample from environmental vibrations, resulting e.g. from the vacuum pumps attached to the chamber. For high harmonic generation in the HHG chamber there is a permanent gas flow leading to poor vacuum conditions (pressure approximately $> 10^{-3}\,\mathrm{mbar}$). This can cause reabsorption of the HHG radiation on the one hand and lead to sample contamination on the other hand. Therefore, once the sample is cleaned it needs to be stored permanently under ultra-high vacuum (UHV) conditions. In Section 7.5 the vacuum system of the beamline is described in more detail. The optical devices needed for the generation of attosecond pulses and the realisation of an XUV-IR pump probe setup are described in Section 7.6. For the characterisation of the HHG radiation and the sample itself, several detectors are installed in the systems. These detectors are explained in Section 7.7.

7.2. Laser systems

There are two CEP stabilized femtosecond light sources that can be used for high harmonic generation and plasmon excitation in the beamline. One laser system is a Femtopower CEP 3 system (Spectra Physics, Wien) consisting of a rainbow oscillator and a multipass amplifier. The second laser system is an Aurora CEP 1kHz (Amplitude, Pessac, France).

The Aurora laser system is shown in Figure 7.2. The oscillator (Venteon Laser Technologies GmbH, Garbsen) delivers CEP stable light pulses with the parameters:

Repetition rate	$80\,\mathrm{MHz}$
Central wavelength	$784\,\mathrm{nm}$
Spectral bandwith	$> 420\,\mathrm{nm}$
Pulse duration	$< 4.9\,\mathrm{fs}$
Mode-locked output power	$> 240\,\mathrm{mW}$

The CEP stabilization is realised by a $f-2f$ interferometer and is the fast feedback loop for the total CEP stabilization of the laser system. These pulses are used as seed pulses for amplification. The pulses are stretched to longer pulse durations in the stretcher to avoid damages on optical elements due to high peak intensities. An acousto-optic programmable dispersive filter (AOPDF) is used for additional pulse shaping. The pulses are preamplified with a regenerative amplifier (Regen) reducing the repetition rate to $1\,\mathrm{kHz}$ by two Pockel's cells at the same time. An acousto-optic programmable gain filter (AOPGF) controls the spectral gain of the Regen. Without a AOPGF, the spectrum would be amplified preferably in the central region due to gain narrowing. This would lead to a loss of bandwidth and therefore to a temporal broadening of the pulse. With the AOPGF the amplification gain in the central region is damped, whereas the gain in the edges is intensified. The first multipass (MP) amplification stage is built in the Regen box and amplifies the pulses to $1.5\,\mathrm{mJ}$. After a second multipass amplifier the pulses have an energy of $8\,\mathrm{mJ}$. In a double pass grating

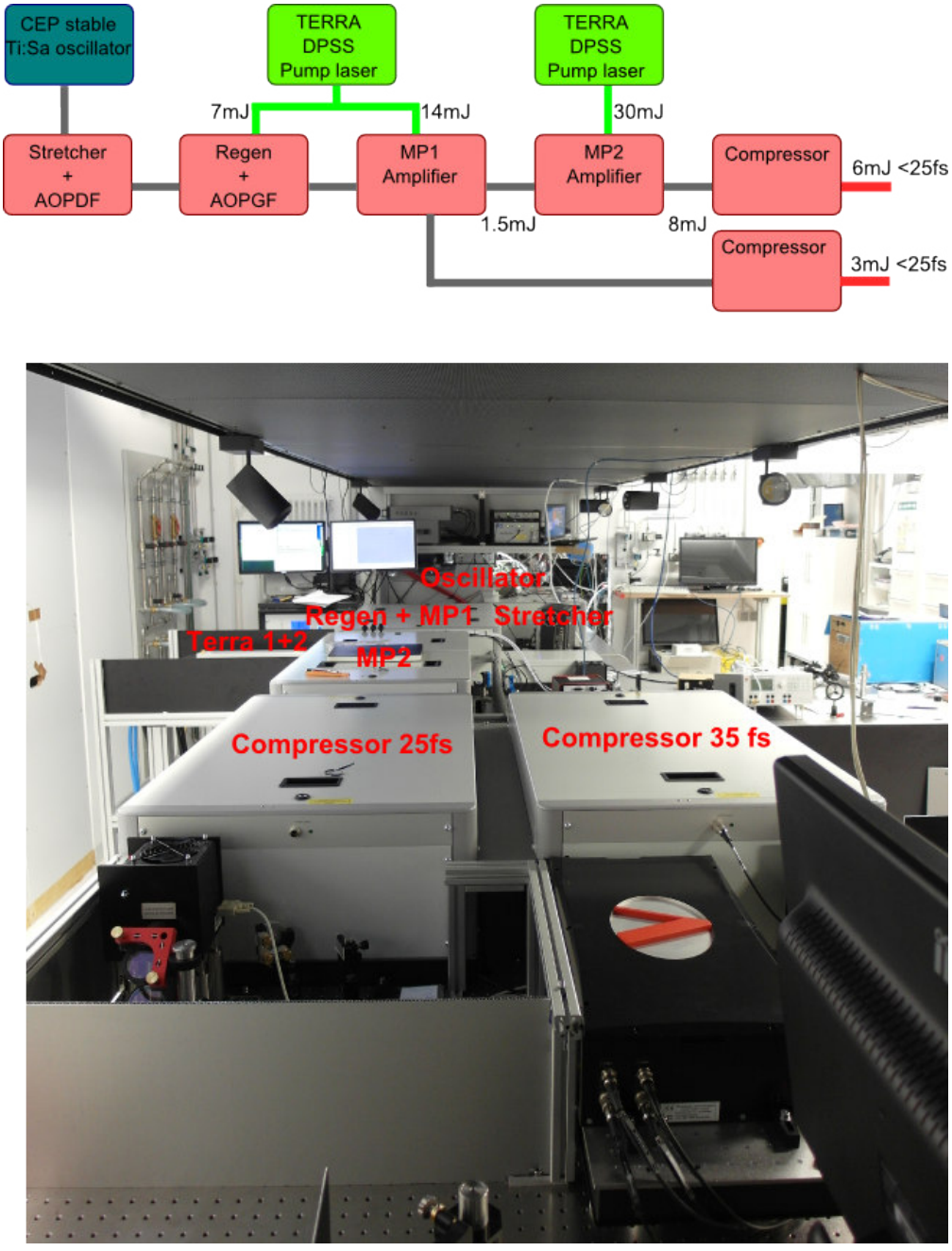

Figure 7.2.: System overview of the Aurora CEP $1\,\mathrm{kHz}$ Lasersystem.

compressor the pulses are recompressed to $35\,\mathrm{fs}$ at $6\,\mathrm{mJ}$. At the exit of the $6\,\mathrm{mJ}$ branch the CEP of the amplified pulses is stabilized in the slow loop with a BIRD (Amplitude, Pessac, France). The BIRD operation principle is similar to $f-2f$-interferometry described in Section 3.3. The pulses are spectrally broadened with white light generation and afterwards frequency doubled. The fundamental and the doubled spectral regions are spatially separated with a grating and then recorded with two photomultiplier.

Behind the amplification and compression stages the pulse has the following parameters:

Repetition rate	$1\,\mathrm{kHz}$
Central Wavelength	$800\,\mathrm{nm}$
Pulse duration	$< 35\,\mathrm{fs}$
Pulse energy	$> 6\,\mathrm{mJ}$
M^2	< 1.2

The CEP is monitored in a long term stability measurement over $9\,\mathrm{h}$ with a ten shot average. Figure 7.3 displays the measurement together with a histogram of the frequency of the single phase values. From the normal distribution of the histogram values the RMS

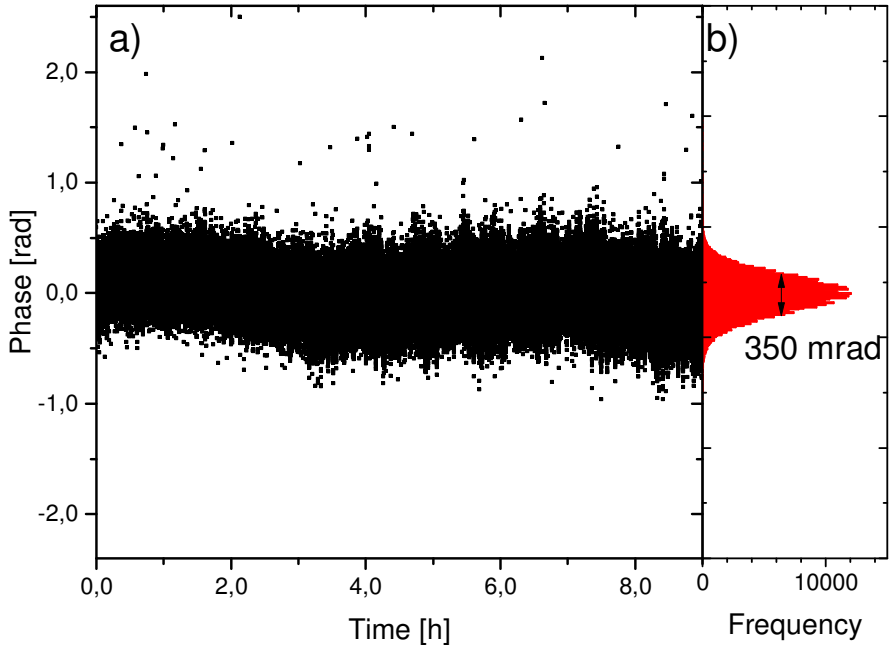

Figure 7.3.: Long time measurement of the CEP stability over $9\,\mathrm{h}$.

deviation of the phase is calculated:

$$\sigma_{\phi_{CEP}} = (175 \pm 1)\,\mathrm{mrad} \tag{7.1}$$

Behind the laser system the beam is split twice into two replica that can be used in three experiments independently. The pulses used in my experiment have a pulse energy of

$1.5\,\mathrm{mJ}$. A typical spectrum of the laser pulses is given in Figure 7.4. A central wavelength at approximately $800\,\mathrm{nm}$ with a spectral bandwidth of $45\,\mathrm{nm}$ FWHM are general conditions.

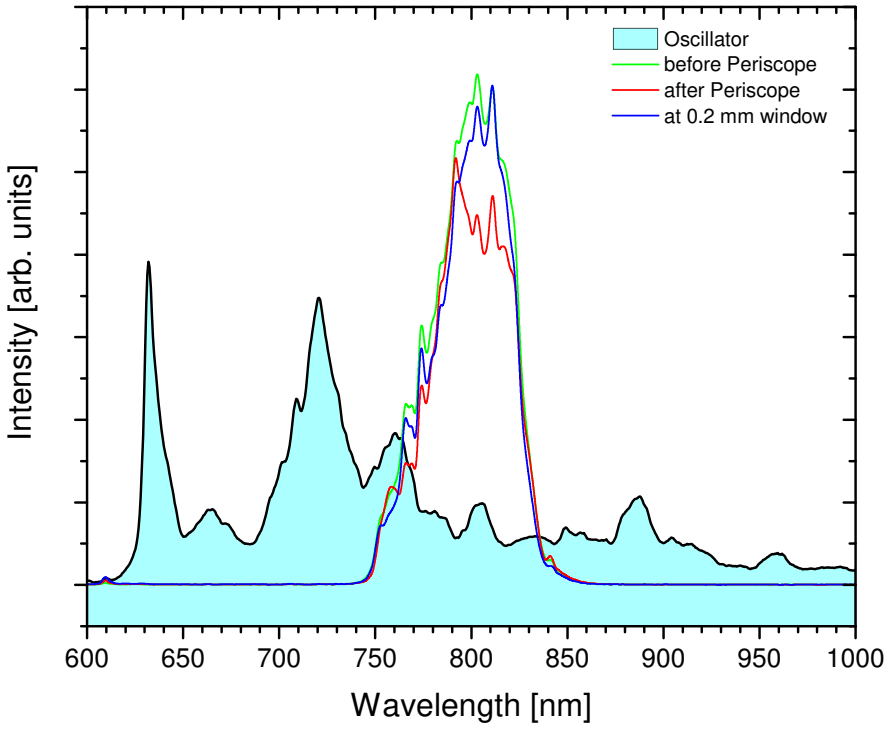

Figure 7.4.: Spectrum of the laser pulses used in the experiment.

The pulse duration is measured with a Wizzler (Fastlite, Valbonne Sophia Antipolis, France) after propagation through air for $6.5\,\mathrm{m}$ to the entrance window of the beamline. After this position, the beam has a propagation distance of approximately $1.5\,\mathrm{m}$ in air and $200\,\mu\mathrm{m}$ in fused silica glass (entrance window). The retrieved intensity is displayed in Figure 7.5 together with the phase resulting in a pulse duration of :

$$\tau = 29.7(12)fs \tag{7.2}$$

with a slight negative chirp.

The Fourier limited pulse duration is retrieved from the spectrum and is $(25.0 \pm 1.2)\,\mathrm{fs}$. During propagation to and through the entrance window the pulse gets further compressed and reaches its shortest duration in the HHG target (optimization with HHG intensity above $70\,\mathrm{eV}$).

Then the laser pulses propagate to the HHG chamber over an overall distance of $8\,\mathrm{m}$. For further compression a hollow fibre compressor will be integrated soon for spectral broadening and further pulse compression down to $5\,\mathrm{fs}$. Before the beam enters the fiber it is propagating over $3\,\mathrm{m}$ in vacuum. The fibre has a length of $3.5\,\mathrm{m}$. The rest of the propagation length is in air.

For Gaussian laser pulse with a duration of $5\,\mathrm{fs}$ and a central wavelength of $800\,\mathrm{nm}$ the pulse duration (FWHM) due to broadening is estimated for a propagation length of $1.5\,\mathrm{m}$ with the software ToptiCalc (Toptica, Gräfelfing):

$$\tau(1.5\,\mathrm{m}) = 18\,\mathrm{fs} \tag{7.3}$$

At the entrance of the HHG vacuum chamber the laser pulse propagates through a fused silica window with a thickness of $200\,\mu\mathrm{m}$ introducing a pulse broadening leading to a pulse duration of an initially Fourier limited pulse:

$$\tau(200\,\mu\mathrm{m}) = 6.4\,\mathrm{fs} \tag{7.4}$$

This broadening has to be compensated with a chirped mirror compressor.

The pulse broadening at the focus position caused by the propagation in air and glass can be minimized by optimizing the compressor of the laser system, such that the shortest pulses are located in the HHG interaction volume by optimizing the HHG signal.

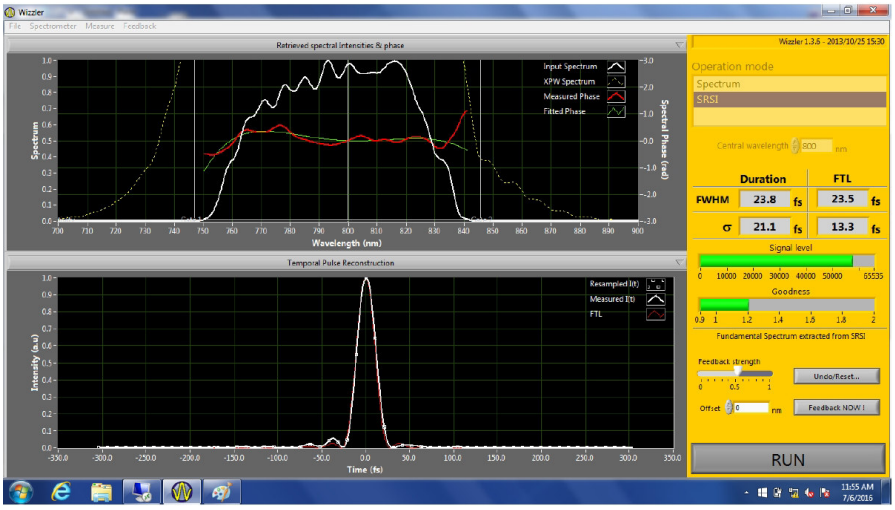

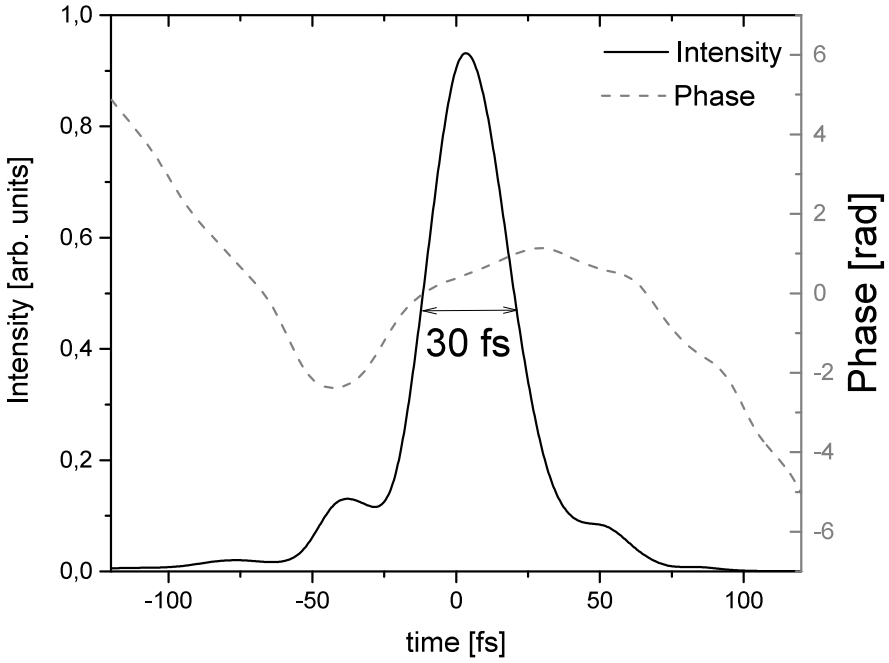

Figure 7.5.: Retrieved pulse duration and phase of the laser pulses measured with a Wizzler directly after the amplifier (On site acceptance test report, Courtesy of Amplitude Technologies S.A.) (top) and close to the beamline incoupling.

7.3. Focusing and incoupling of the NIR laser beam

The driving laser beam is coupled into the vacuum system for the high harmonic generation with a periscope and several ultrafast mirrors through a fused silica window. The path of the laser beam is simulated with the optic simulation software OSLO (Lambda research) for optimising the focus size and to minimize abberations from tilted mirrors. For the simulation a central wavelength of $790\,\mathrm{nm}$ is assumed. The design is shown in Figure 7.6

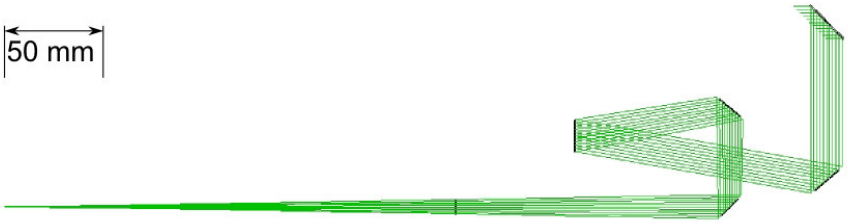

Figure 7.6.: Setup for the incoupling of the laser beam into the HHG chamber. Exact values for the distances and angles can be found in the appendix C.

The input beam diameter is reduced after the periscope with an iris aperture to a maximum of $16\,\mathrm{mm}$. The beam is then reflected by two mirrors before focussing. For minimizing the astigmatism the angle of incidence to the focusing mirror should be as small as possible. The focussing mirror has a focal length of $500\,\mathrm{mm}$. Behind the focusing mirror the beam is reflected twice to enter the HHG chamber through a fused silica window. The distance from the entrance window to the HHG gas target is $230\,\mathrm{mm}$. The exact values of distances and tilting of the mirrors are given in the appendix C. Finding the best position of the focus inside the gas target, the target can be positioned manually *in-situ*. A spot size analysis is demonstrated in Figure 7.7. The diffraction limited focus radius for an input beam of $780\,\mathrm{nm}$ beam is shown by the airy disk that is $29\,\mu\mathrm{m}$. The aberrations resulting from the mirror tilt of the focusing mirror enhance the expected focus radius. Here it is determined by the geometrical spot size radius that is $87\,\mu\mathrm{m}$. In Figure 7.8 the focus is traced over a defocusing range of $2\,\mathrm{mm}$ before and behind the minimum spot size. The astigmatism introduced by the tilted focusing mirror can be seen by the deviation of the horizontal and vertical dimension and the flip of orientation of the longer dimension from vertical to horizontal when moving through the focus position. The focus size of the NIR beam determines the source size of the HHG, that is identified in Section 7.9

7.4. Setup of the attosecond beamline

For the investigation of condensed matter samples with attosecond time resolution a beamline is designed. The attosecond pulse generation follows the traditional HHG conversion and filtering scheme described in Section 3.7.3. For the HHG pulse generation a stainless steal vacuum chamber is developed that enables the feed through of a noble gas, and allows manual positioning of the gas tube along the beam. The gas tube support is illustrated in Figure 7.9.

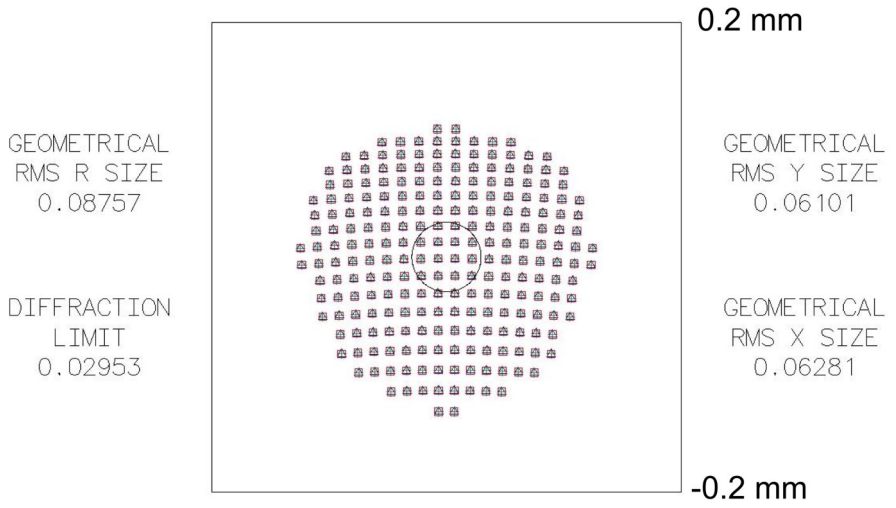

Figure 7.7.: Spot diagram generated with $780\,\mathrm{nm}$ central wavelength in the focus position showing an asymmetric geometrical RMS focus with radii of $61\,\mu\mathrm{m}$ and $63\,\mu\mathrm{m}$ in vertical and horizontal direction, respectively.

The gas enters the vacuum chamber through a pressure controller and a standard gas feedthrough of a welded stainless steel tube on a CF16 flange. The tube is connected with the stainless steel gas target body via a teflon hose and standard Swagelok connectors. The body of the target contains and delivers the gas to the target tube. The target tube is connected to the top hole with a pressing nut and pressure sealed by squeezing a viton o-ring. When the laser beam hits the HHG target tube for the first time it drills a hole, that forms the interaction path for the HHG process. With time the hole becomes bigger and the gas flow becomes to high. Then the tube needs to be replaced.

Behind the HHG chamber a first differential pumping stage is located. The design of the chamber is illustrated in Figure 7.10.

This chamber is directly connected via a CF63 flange to the HHG chamber and is used to pump both chambers. Inside the first differential pumping chamber the open diameter in the beam propagation direction is reduced with a conical hole. A second cone with a smaller hole in the peak can be put inside the conical hole such that the gas transport is impeded. Two turbo pumps can be connected via two CF63 flanges. The flanges are arranged such that the gas flow is split in propagation direction of the beam and reflected into the turbo pumps.

Behind the first differential pumping stage a first valve separates the HHG vacuum system from the rest of the beamline. Also the tubing diameter is reduced from CF40 to CF16 to reduce conduction of the gas.

A following vacuum tube is mounted in two spherical heads (shown in Figure 7.11) allowing for tube positioning together with two translation stages perpendicular to the beam. The tube is mechanically isolated by two membrane bellows such that positioning can be done without moving the HHG and experimental chamber.

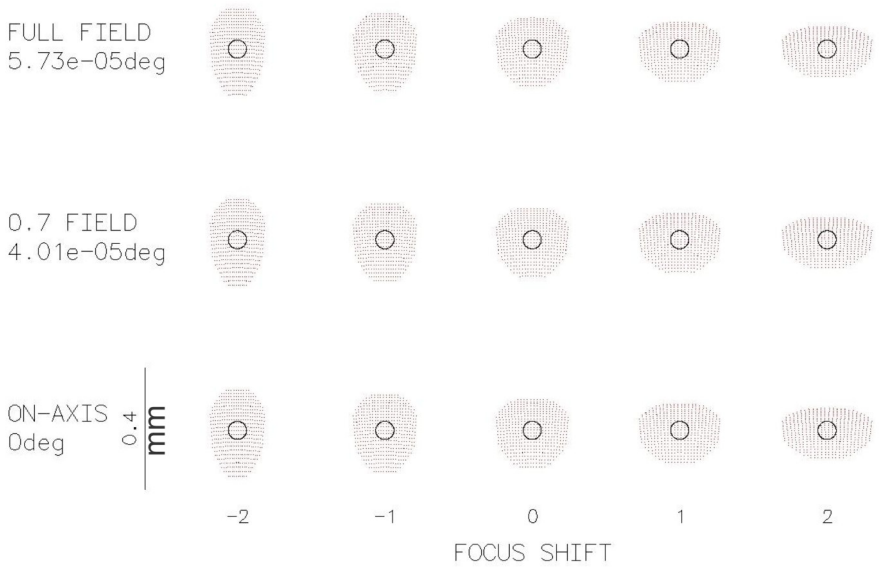

Figure 7.8.: Spot diagrams at positions $\pm 2\,\mathrm{mm}$ shift from the focus position.

Figure 7.9.: Flange carrying the setup for the HHG. The gastube is built on slides and can be positioned along the NIR beam with a manipulator. The gas is provided via a gas feed through and a hose connecting the feed through and the tube holder.

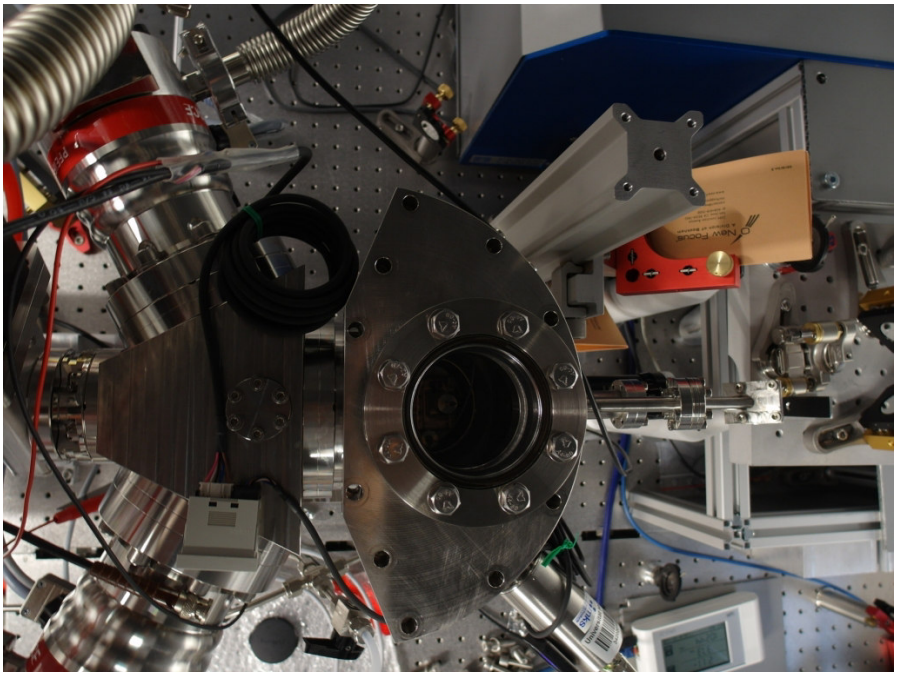

Figure 7.10.: Photograph of the first differential pumping stage

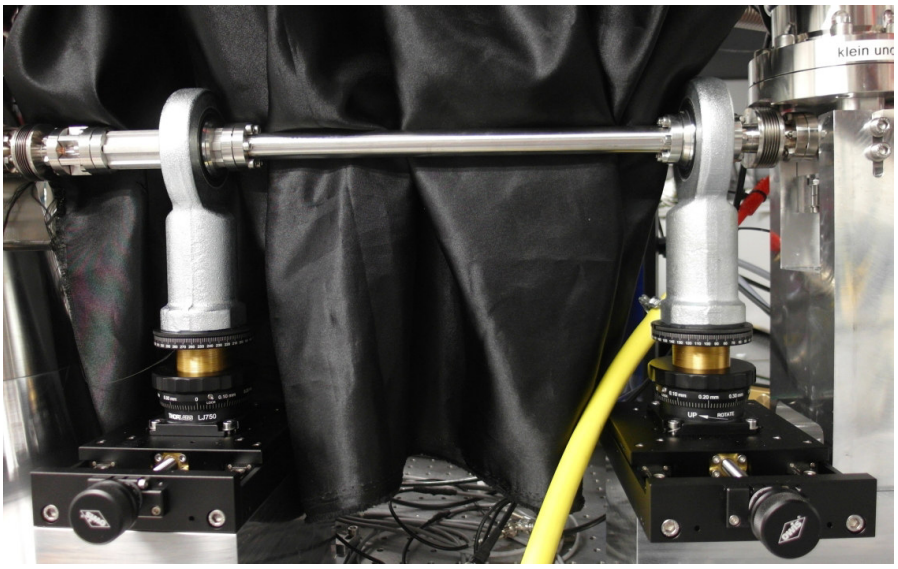

Figure 7.11.: Beam positioning setup with two translation stages with spherical heads.

Behind the tube positioning system another valve separates the tubing system from the following experimental chamber. The design of the experimental chamber provides a section for sample positioning in a spherical surrounding such that everything that is connected to the different ports points at the center of the chamber where the sample is located. At the chamber entrance flange a filter wheel is attached. The filter wheel is described in more detail in Section 7.6. The most important implementation is the manipulator that allows sample positioning with three translation degrees of freedoms and two rotational degrees of freedom, rotation along the manipulator axis and in the sample surface. A time of flight spectrometer (described in Section 7.7) is mounted from top to collect the photoelectrons with an alignment bellow for rough alignment of the attached device with three screws. For imaging the sample surface a standard CCD camera with a zooming objective is mounted on a viewport from the top. The rear part of the chamber is cylindrical providing ports for mounting the double mirror, and MCP detector (as part of a grating spectrometer for the HHG beam characterisation) and other flanges. The double mirror is described in more detail in Section 7.6 and the grating spectrometer in Section 7.7.

The attention of the beamline design is focused on vibration isolation. Attosecond experiments require a very high stability on nanometer scale (an $200\,\mathrm{as}$ light pulse has spatial length of $60\,\mathrm{nm}$). Vibrations generated e.g. by vacuum pumps attached to the chamber therefore lead to a distortion on this scale. The vibration isolation therefore has a high impact on experimental conditions. The isolation for the double mirror and the sample manipulator is most critical. The sample head of the manipulator is isolated from the experimental chamber with a highly flexible membrane bellow . The double mirror is isolated by positioning on a stand attached to the optical table and decoupled from the experimental chamber with another membrane bellow. All other chambers are mounted on heavy and stable stands enabling a solid stand on the optical table with low vibrational guiding to the optical table.

7.5. Vacuum technics of the beamline

The vacuum technical setup of the beamline is depicted in Figure 7.12. The two main chambers are the chamber for high harmonic generation (HHG) and the experimental chamber (EXP). To the experimental chamber an electron time-of-flight (TOF)spectrometre is connected. Both chambers and the TOF are pumped with turbomolecular pumps (HHG: two Pfeiffer HighPace 80, and EXP: one Pfeiffer HighPace 300). To reach UHV conditions in the experimental chamber a getter pump (SAES Capacitorr) can be activated. The high harmonic generation takes place in a small tube, through which the laser beam drills a hole to interact with the gas. The radiation can pass through the drilled hole but there is also a jet expansion from the tube. This leakage leads to a drop of vacuum pressure to about $10^{-2}\,\mathrm{mbar}$. In order to reach UHV conditions in the experimental chambers it is necessary to incorporate differential pumping stages in the beamline. A differential pumping stage is designed to prevent gasflow from one side to another. There are different approaches to realise differential pumping. In this beamline two concepts are realised. The first differential pumping stage directly connected to the HHG chamber is realised by a small aperture enabling beam propagation but prohibiting gas flow. The second and third differential pumping

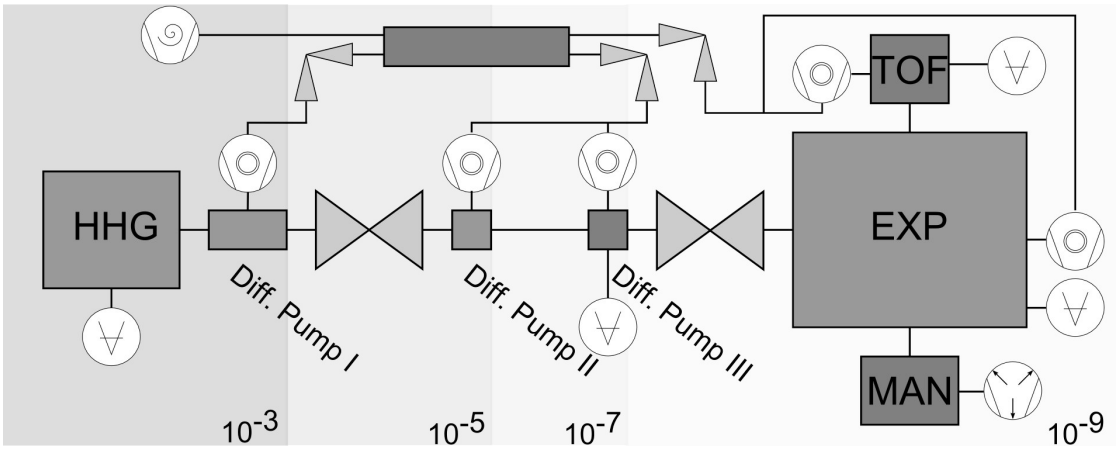

Figure 7.12.: Technical design of the vacuum system of the beamline.

stages consists of very small vacuum chambers which are pumped additionally with a turbo pump (Pfeiffer HighPace 80). With each differential pumping one to two orders of magnitude in pressure are gained. How the system reacts to gas flow of nitrogen in the HHG chamber is shown in Figure 7.13. For this test nitrogen is used, because the turbo pumps are designed for efficient pumping of this gas. Therefore, with this test the best performance of the system is found.

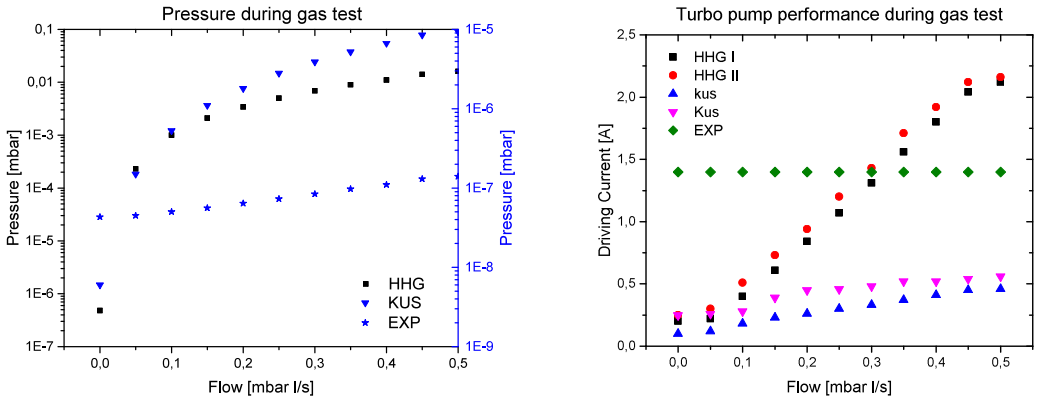

Figure 7.13.: Gas test in the beamline. A controlled permanent gas flow can enter the vacuum system through the laser drilled hole in the HHG tube. The pressure a) is measured in the HHG chamber itself, the third differential pumping stage and the experimental chamber. Also the turbo pump driving current is measured b).

The gas flow is controlled with an absolute pressure controller (MKS 640A, power supply/readout PR400B) and can be set in $0.001\,\mathrm{mbarl/s}$ steps at minimum. For the gas test the gas flow is increased in $0.05\,\mathrm{mbarl/s}$ step. Each step contains $2\,\mathrm{min}$ gas flow, then read-

ing out the pressures of the main vacuum chambers (high harmonic chamber HHG, third differential pumping stage 'Klein Und Süß' (KUS), and experimental chamber EXP)and the driving currents of the attached turbo pumps (HHGI and II at first differential pumping chamber on the HHG side, kus and KUS at second and third differential pumping stages, and EXP at experimental chamber). With a gas flow increasing from $0.05\,\mathrm{mbarl/s}$ to the upper design limit of $0.5\,\mathrm{mbarl/s}$, the pressure in the HHG chamber raises from $10^{-4}\,\mathrm{mbar}$ to $10^{-2}\,\mathrm{mbar}$. The pressure at the third differential pumping stage reaches $1 \times 10^{-6}\,\mathrm{mbar}$ and the pressure in the experimental chamber increases from a base pressure of $4 \times 10^{-8}\,\mathrm{mbar}$ to $1 \times 10^{-7}\,\mathrm{mbar}$. So the differential pumping stages can finally realise a pressure difference of $10^{-5}\,\mathrm{mbar}$.

The beamline is divided in three sections by two pneumatic valves. The first valve divides the HHG section from the second and third pumping stage, the second valve divides the pumping stages from the experimental chamber. All turbomolecular pumps installed in the beamline are connected to a distributing tube with angle valves. The tube is prepumped either with a scroll pump (Edwars nXDS15, base pressure $< 1 \times 10^{-1}\,\mathrm{mbar}$) or can be connected to the laboratory prevacuum line (Leybold DRYVAC, base pressure $< 1 \times 10^{-3}\,\mathrm{mbar}$) via an additional valve.

7.6. Optical elements in the beamline

The optical setup of the beamline starts with the high harmonic generation in the HHG chamber as illustrated in Figure 7.9.

For this process there is a small tube installed where the gas for the interaction is provided. The gas flow is controlled outside of the vacuum system with an absolute pressure controller (MKS 640B Absolute Pressure Controller). Via a Swagelok feedthrough on a CF16 flange the gas is delivered into the gas tube inside the vacuum system. The gas tube is mounted on a sliding base that can be positioned along the NIR beam direction with a one axis manipulator to optimize the HHG signal by relative positioning to the focus.

After the HHG tube the XUV and the NIR beams are co-propagating. The creation of isolated attosecond pulses from XUV pulse requires spectral filtering. Also other filters have to be installed in the vacuum system to transmit only spectrally separated beams. Therefore a filter wheel is designed containing all required filters and a hole for the unfiltered beam. The manually rotatable filter wheel is pictured in Figure 7.14. The filter wheel, directly attached to the experimental chamber, offers five slots for filters and a clear hole for the unfiltered beam. Three slots can hold ring mounted filters, which are attached to a mounting ring. With a zirconium filter only the high energy part ($10\,\mathrm{nm}$ to $20\,\mathrm{nm}$) of the XUV beam can be transmitted, with an aluminum filter longer wavelength of the XUV are transmitted ($20\,\mathrm{nm}$ to $60\,\mathrm{nm}$). The transmission curves of the zirconium and the aluminum filter are displayed in Figure 7.15. The other two slots are for two part filters mounted on a pellicle transmitting the high energy part of the XUV beam only in the inner part and the NIR radiation only in the outer part. Additionally an iris aperture is attached to the filter wheel to control the transmitted NIR intensity by controlling the beam size. The iris aperture can be positioned with a sliding x-y unit driven by two picomotors (Newport 8301-UHV). Another picomotor

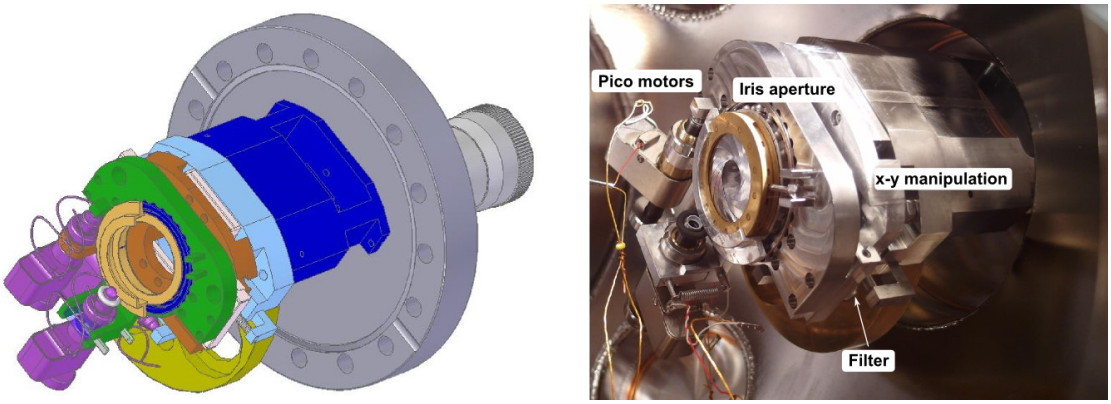

Figure 7.14.: Illustration of the filter wheel with iris aperture mounted on a flange directly attached to the experimental chamber.

controls the open diameter of the iris aperture.

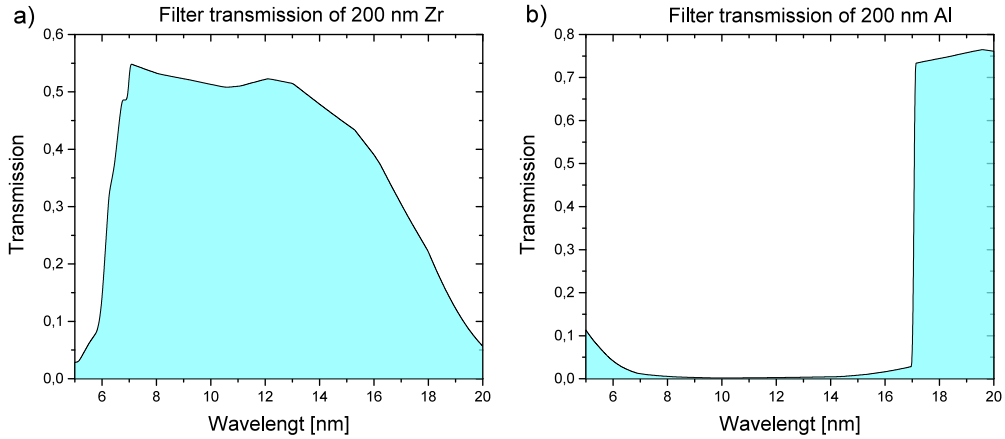

Figure 7.15.: Transmission curves of zirconium a) and aluminium b) filter.

The refocussing of the two beams spatially and temporally separated to the sample surface is realized with a two part mirror that is composed with a holy outer mirror for the NIR beam and an inner core for the XUV beam. The mirror mount setup is shown in Figure 7.16. The mirror pair can be moved in or out of the beam with a motorized translation stage (Attocube ECS3080). The mirror stack can also be rotated with a motorized rotator (Attocube ECR5050). With several ultrafine adjustment screws (Thorlabs 3/16"-100 Ultra-Fine Hex Adjusters) it is possible to align the mirror pair and their focus on the sample surface and the position of both mirrors relatively to each other. The outer NIR mirror is mounted on a motorized mirror mount (Mechonics MT.025.0090)and can be positioned electronically independent from the inner part. The delay between the inner and outer mirror is realized with a nanometer positioning stage (Physik Instrumente PIHera 621.1) that moves the inner mirror decoupled from the outer mirror. The maximum delay is $100\,\mu\mathrm{m}$ with a repeatability

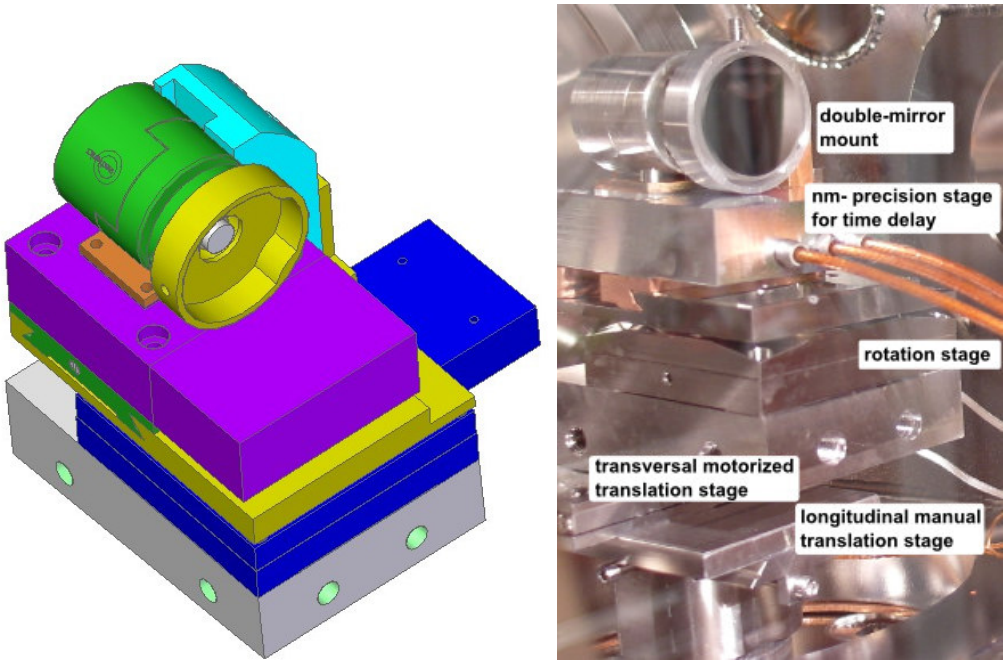

Figure 7.16.: Illustration of the mirror mount setup for the double mirror. The focus can be aligned on the sample surface and the two pulses can be temporally delayed.

of $\pm 1\,\mathrm{nm}$. To decouple the mirror from external vibrations, a stand has been designed that is decoupled from the vacuum chamber by a bellow and filled with quartz sand for an even higher stability.

For commissioning with an argon gas target for HHG a mirror centred around $79\,\mathrm{eV}$ is used. Later, for experiments with HHG from neon a mirror centred around $90\,\mathrm{eV}$ will be used. Both reflectivity curves are given in the Appendix B.

To the baseplate of the double mirror mount a grating spectrometer can be mounted, which is described in more detail in Section 7.7.1.

7.7. Detectors

7.7.1. Grating spectrometer

To measure the HHG spectrum a grating spectrometer is built inside the experimental chamber. The grating is mounted on a special holder connected to the double mirror setup and can be positioned in the beam with the translation stage moving the double mirror. The grating deflects the high harmonic beam. The beam is dispersed and the first order reflected in grazing incidence via a gold mirror towards the imaging detector. The detection of the high harmonic beam is realized with a micro channel plate (MCP) for amplification of the signal and an imaging phosphor screen. The MCP is mounted together with a phosphor screen on the rear flange of the experimental chamber.

The MCP (MCP 45, German Image Detector Systems)used in this system has an active diameter of $45\,\mathrm{mm}$ and is of imaging grade. The phosphor screen is coated with P43 with an ITO underlayer and has also an active area of $45\,\mathrm{mm}$.

For finding the position of the MCP detector the position of the spectrum has to be calculated according to:

$$\sin\alpha = m\frac{\lambda}{g} \qquad \tan\alpha = \frac{x}{l} \tag{7.5}$$

with the diffraction angle α, the diffraction order m, the wavelength λ, the grating constant g defining the distance between two lines, and the geometrical positions l longitudinal and x transversal to the diffracted beam.

For a transmission grating with $10\,000\,\mathrm{lines/mm}$ the grating constant is $100\,\mathrm{nm}$. The spectrum of the harmonic beam is assumed to reach $100\,\mathrm{eV}$ in the cut-off region corresponding to approximately $12\,\mathrm{nm}$. The transmission of the zirconium filter used for transmission of the XUV pulse has a transmission for $7\,\mathrm{nm}$ to $16\,\mathrm{nm}$. The spectrum between $7\,\mathrm{nm}$ to $17\,\mathrm{nm}$ is refracted in the open angle $\Delta\alpha$. For the first diffraction order it is calculated to:

$$\Delta\alpha = \arcsin\left(1\cdot\frac{17\,\mathrm{nm}}{100\,\mathrm{nm}}\right) - \arcsin\left(1\cdot\frac{7\,\mathrm{nm}}{100\,\mathrm{nm}}\right) = 9.8^\circ - 4.0^\circ = 5.8^\circ \tag{7.6}$$

The active diameter of the MCP is $45\,\mathrm{mm}$. The distance of the MCP to the grating is $220\,\mathrm{mm}$. The zero order and the first order of the $17\,\mathrm{nm}$ beam have a separation of :

$$x = 0.22\,\mathrm{m}\cdot\tan 9.8^\circ = 38\,\mathrm{mm} \tag{7.7}$$

The position of the $7\,\mathrm{nm}$ beam is then found at the position:

$$x(7\,\mathrm{nm}) = \tan 4.0^\circ\cdot 0.18\,\mathrm{m} = 10\,\mathrm{mm} \tag{7.8}$$

still separated from the zero order direct beam.

For displaying the full spectrum on the MCP, the direct beam has to be located on one side and the first order on the other side. Since the MCP is mounted centred to the direct beam, either the grating distance needs to be decreased or the MCP must be mounted on a flexible bellow. For future work, the mounting on the bellow already has been prepared. Until then the grating distance to the MCP is decreased to fit the active optical area.

The MCP stack is shown in Figure 7.17. The stack is mounted on a CF63 flange with three SHV feed through connectors. The MCP is connected with two copper rings from the front and back side applying a potential of $-1.1\,\mathrm{kV}$. A phosphor screen is located at the back side electrically isolated from the MCP by a PEEK distance ring. The phosphor screen is also electrically connected by a copper ring to apply a positive potential of $3\,\mathrm{kV}$

7.7.2. Time of flight spectrometer

The electron detector in the experimental chamber is a commercial electron time of flight (TOF) spectrometer from Stefan Kaesdorf (Stefan Kaesdorf, Geräte für Forschung und Industrie, Munich). With the detector the kinetic energy of the photoelectrons is measured.

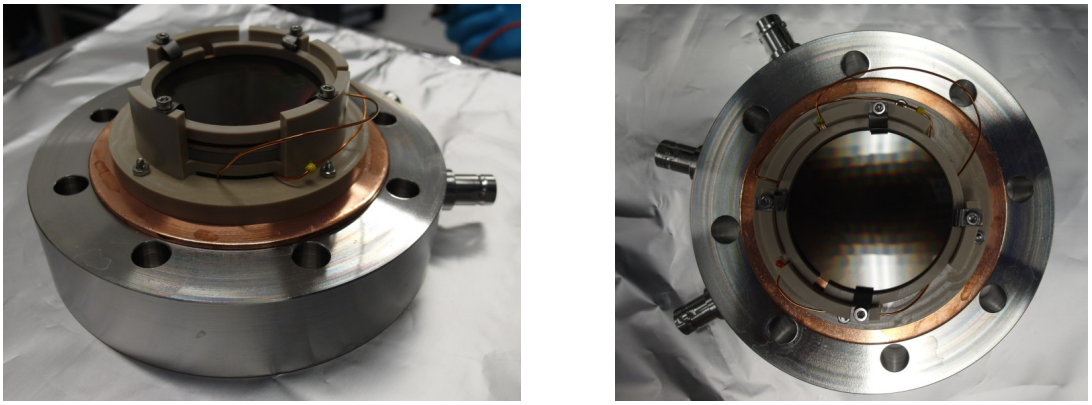

Figure 7.17.: Photograph of the microchannel plate stack for imaging the direct beam and for the grating spectrometer.

The TOF is attached from the top flange on the spherical part of the experimental chamber together with a bellow for alignment of the entrance relative to the sample surface. The spectrometer is designed for a working distance of $3\,\mathrm{mm}$ distance between the interaction area and the entrance of the TOF. The full collection angle of the TOF is $45°$ for an ionisation zone smaller than $200\,\mu\mathrm{m}$. After entering the TOF the electrons enter the drift tube, that is a field free region (encapsulated with a μ-metal shielding) where the electrons are propagating and dispersing due to their different initial velocities. For the measurement of very fast ($E_{kin} > 200eV$) or very slow electrons there is the possibility of deceleration or acceleration, respectively, by applying a negative or positive voltage ($\pm 180\,\mathrm{V}$) to the drift tube. Behind the drift tube the dispersed electron packet is accelerated by additional $1000\,\mathrm{eV}$ in the post-acceleration stage to lower the influence of the earth magnetic field that still can penetrate through the back side of the spectrometer. Then the electron packet hits an MCP detector (diameter $40\,\mathrm{mm}$, pore size $5\,\mu\mathrm{m}$, where the electron signal is multiplied. The time dependent electric output signal of the MCP is proportional to the time dependent number of electrons for a specific kinetic energy.

7.8. Sample manipulation

The sample holder is attached to an ultrastable manipulator (Omniax, Vacgen, East Sussex) and can be positioned translative in x-,y- and z-direction, and rotational along the manipulator axis and the sample surface plane. The sample holder is decoupled from the whole systems by a two diaphragm bellow system. The travel range in x- and y-direction is $\pm 25\,\mathrm{mm}$ and in z-direction $1000\,\mathrm{mm}$. The manipulator is bakeable to $230°$ providing an operating pressure down to $10^{-11}\,\mathrm{mbar}$. For loading more than one sample into vacuum a multi sample head has been built, which is illustrated in Figure 7.18. With this, up to six samples can be loaded on the manipulator and positioned in the experiment.

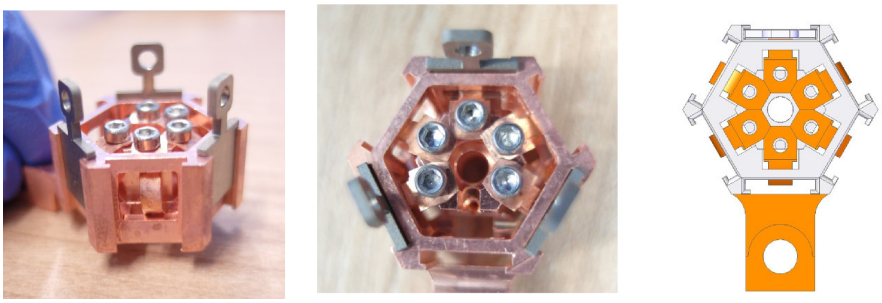

Figure 7.18.: Multi sample head for loading of up to six samples.

7.9. Determination of HHG source size

For the initial commissioning of the beamline argon is used for the HHG. To determine the source size the direct HHG beam is filtered with a Zr filter and imaged onto the MCP as shown in Figure 7.19. The filter transmits only the high energy harmonics above $70\,\mathrm{eV}$.

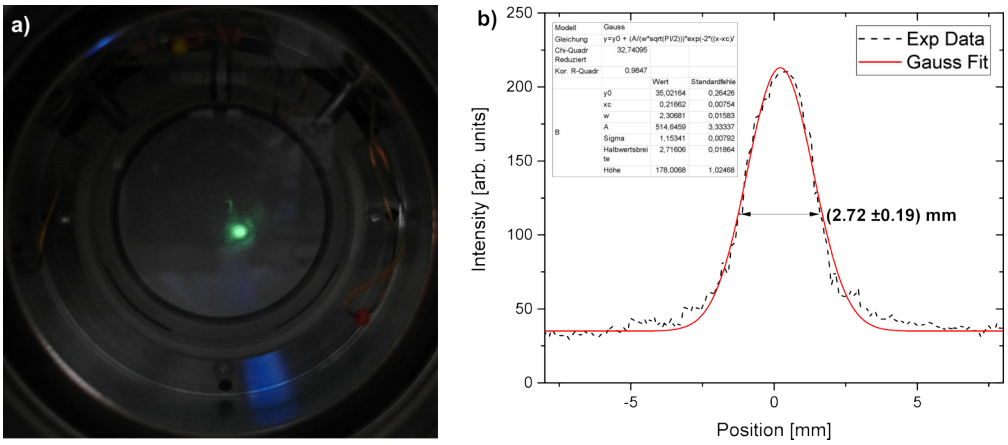

Figure 7.19.: Image of the HHG beam on the phosphor screen behind the MCP after spectral filtering with a Zr filter a) and beam profile with Gauss fit in b) resulting in a diameter of $(2.7 \pm 0.1)\,\mathrm{mm}$ FWHM.

For the following calculation a Gaussian beam is assumed. The divergence θ of a Gaussian beam is connected to the source size via the relation:

$$\theta = \frac{\lambda}{\pi w_0} \qquad \text{with} \theta = \tan\frac{w(l)}{l} \simeq \frac{w(l)}{l} \tag{7.9}$$

with the wavelength λ, and the beam waist w_0 which is half of the source size, the beam radius $w(l)$ at the position of the MCP and the distance l between HHG target and MCP. For the given geometry of $l = 2\,\mathrm{m}$ and $w(l) = (2.31 \pm 0.02)\,\mathrm{mm}$ $(1/e^2)$ the divergence is $(1.12 \pm 0.01)\,\mathrm{mrad}$. The wavelength transmitted through the filter is above $17.7\,\mathrm{nm}$. With

these values the source size radius is calculated:

$$w_0 = \frac{\lambda}{\pi\theta} = \frac{\lambda l}{\pi w(l)} = \frac{17.7\,\mathrm{nm} \cdot 2\,\mathrm{m}}{\pi \cdot 1.15\,\mathrm{mm}} = (4.88 \pm 0.04)\,\mu\mathrm{m} \tag{7.10}$$

The source size of the HHG beam is twice the beam waist and therefore approximately $10\,\mu\mathrm{m}$. The beam used in the experiment does not have a Gaussian profile ($\chi^2 = 32.7$), but for estimating the lowest limit for the source size it is an appropriate assumption.

7.10. Next steps

7.10.1. Xenon spectrum for TOF calibration

For calibration of the TOF the photoelectron spectrum of xenon can be recorded with distinct lines at:

Orbital	Binding energy eV	Kinetic Energy @ $79\,\mathrm{eV}$ ev
$4d\,7/2$	69.5	9.5
$4d\,5/2$	67.5	11.5
$5s$	23.3	55.7
$5p\,3/2$	13.4	65.6
$5p\,1/2$	12.1	66.9

Table 7.1.: Table of xenon electrons with their binding energy and kinetic energy after photoemission with $79\,\mathrm{eV}$ beam. Data taken from [135].

Additionally the sharp Auger linies in xenon can be used. The spectrum of the NOO Auger decay from $5s5p$ states is shown in Figure 7.20

For the simulation of the photoelectron spectrum for measurements with the Kaesdorf TOF spectrometer *SimIon* (Scientific Instrument Services Inc., USA) is used. The lens and drift tube voltages are adjusted to optimize the flight path inside the TOF to maximize the number of electrons that reach the detector. To high or to low lens voltages significantly reduce the number of detected electrons and lead to a bad signal-to-noise ratio or even lead to electron acceleration away from the TOF entrance. In the following table values for the lens and retardation voltage are listed that are optimized for the different emission states: The flight path of these electrons are illustrated in Figure 7.21. For the $4d$ electrons lens voltages of $65\,\mathrm{V}$ and $80\,\mathrm{V}$ are found. With those values the electron beams of both lines are collimated, respectively. Only the $5s$ electrons which are emitted in a small angle reach the detector. The electrons that can enter the TOF but do not reach the detector and hit the drift tube. Some of the $5s$ and the $5p$ electrons even do not enter the entrance aperture. Increasing the lens voltage even the faster electrons are collected and collimated. For the $5s$ electrons with an optimized configuration for $55.7\,\mathrm{eV}$ kinetic energy the lens voltage is set to $360\,\mathrm{V}$. For the $5p$ electrons an optimum value of $400\,\mathrm{V}$ is found for a collimated beam. In this case, the slow electrons already disperse but still reach the detector.

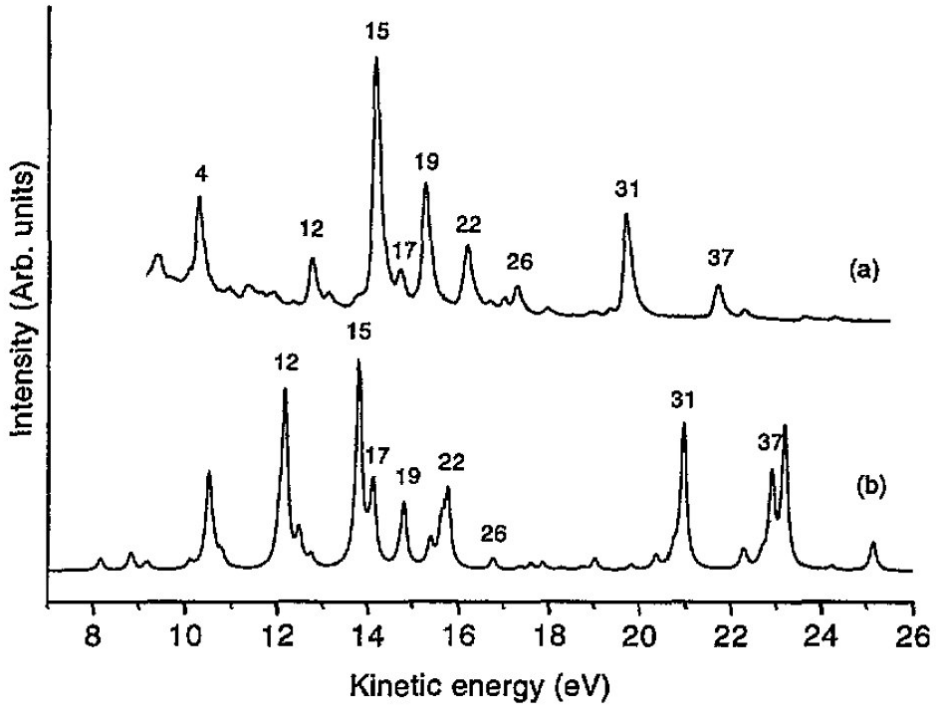

Figure 7.20.: NOO Auger decay in xenon: experimental data are shown in a) and calculated data in b). Copyright IOP Publishing. Reproduced with permission from [136]. All rights reserved.

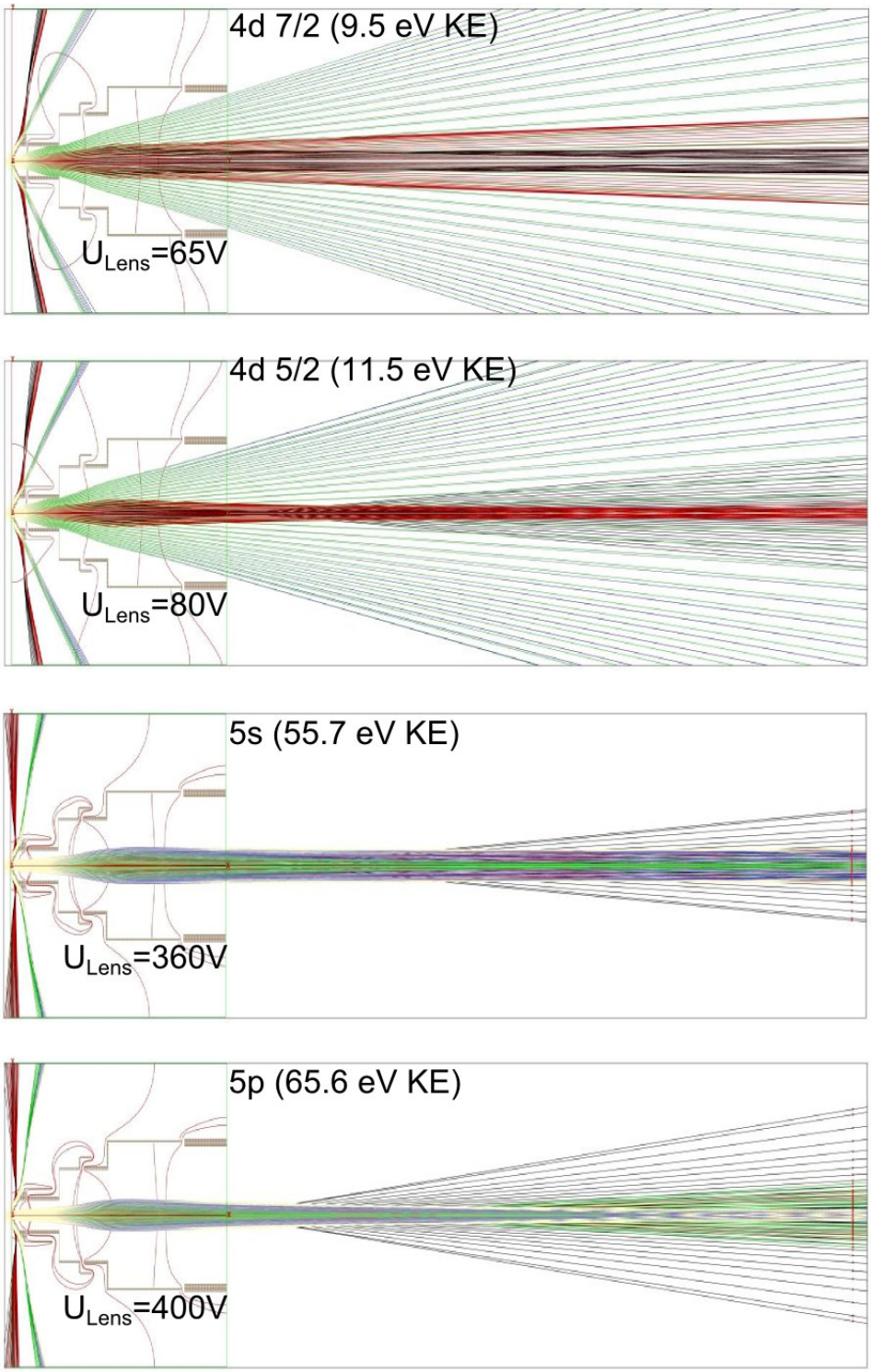

Figure 7.21.: Time of flight paths of xenon $4d$, $5s$, and $5p$ electrons with lens and retardation voltage optimized for each spectral line. The electrons are emitted in $\pm 45°$. The acceptance angle of the TOF is $30°$

Orbital	Kinetic energy eV	Lens kV	Drift tube kv
$4d\,7/2$	9.5	65	-5
$4d\,5/2$	11.5	80	-5
$5s$	55.7	360	-5
$5p\,1/2/5p\,3/2$	65.6	400	-5

Table 7.2.: Optimization of TOF potentials for photoelectrons from accessible orbitals without natural line broadening excited with a monochromatic XUV beam at $79\,\mathrm{eV}$.

As one can see the lens voltage setting defines spectral region line by lateral dispersion. The retardation voltage leads to a longitudinal dispersion of the electron beam resulting in a retardation or acceleration of the flight time. In Figure 7.22 the influence of the retardation voltages to the flight time is evaluated.

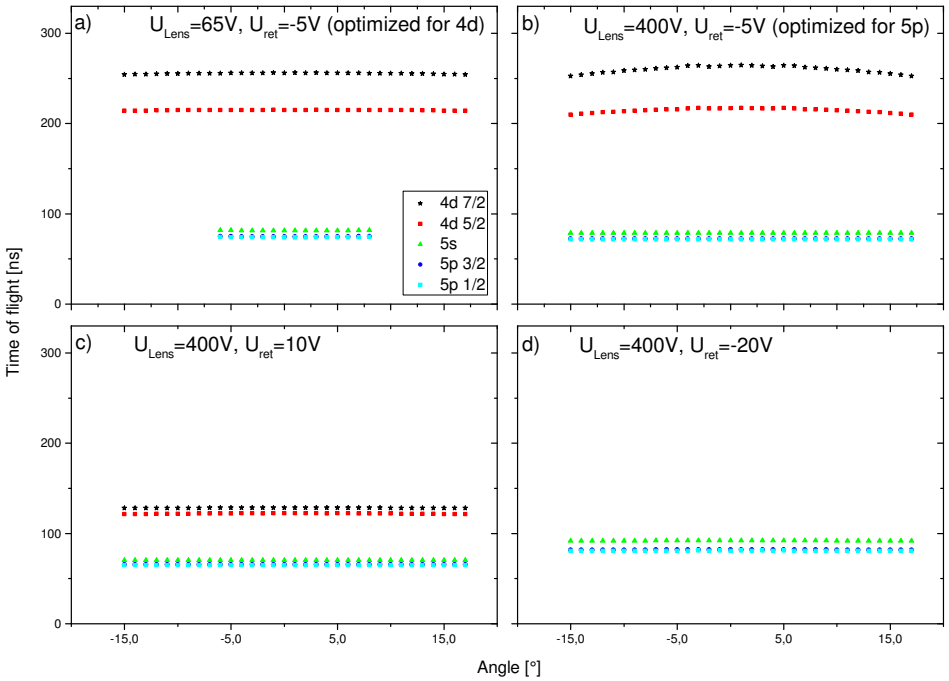

Figure 7.22.: Time of flight times of xenon $4d$, $5s$, and $5p$ electrons excited with a $79\,\mathrm{eV}$ beam with different lens and retardation voltages.

In a) the flight times for the different states are plotted for the $4d$ optimized lens and retardation voltages. The flight times are almost constant for all lines, independent from the emission angle. The acceptance angle for the fast electrons is decreased to less than $20°$. Therefore, not all emitted photoelectrons are detected which will decrease the peak intensity with respect to other peaks. In b) the time of flights for the $5p$ optimization are shown. The time of flight for the slow electrons are not constant anymore. This leads to a broadening

in the time signal of the peaks. The flight time distribution for each $5p$ and the $5s$ line is narrow similar to a). All electrons that enter the TOF within its acceptance angle reach the detector. In c) and d) only the retardation voltage is changed to $10\,\mathrm{V}$ and $-20\,\mathrm{V}$. In the first case the electrons are further accelerated inside the drift tube and therefore the time of flight becomes shorter resulting in a worse resolution assuming a fixed region of interest. In the second case, the electrons are further decelerated resulting in a better resolution but only the fast electrons reach the detector. However, for very slow electrons (kinetiv energy below $10\,\mathrm{eV}$ an acceleration is necessary due to the limited detection window.

7.10.2. Proof-of-principle experiment

In a proof-of-principle experiment a photoelectron spectrum of phenylalanin will be measured. Phenylalanin is a chiral amino acid based on a benzene ring. A model of the chemical structure is illustrated in 7.23. The measurement of adiabatic attosecond charge migration

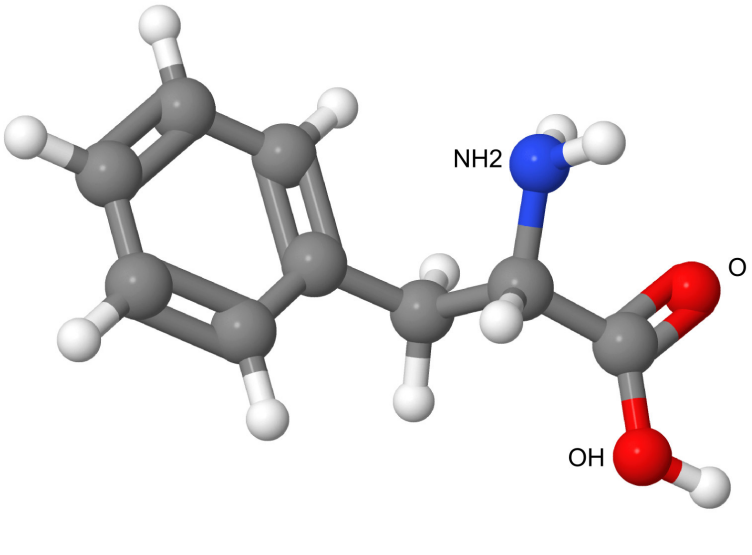

Figure 7.23.: Chemical structure of D-Phenylalanin ($C_9H_11NO_2$). Figure produced with Jmol.

in ring shaped molecules is a recent topic in attosecond science [17, 137, 138]. The period of the charge migration in benzene is predicted to $848\,\mathrm{as}$ [137]. To access the charge dynamics on the molecule with XUV pulses enabling attosecond time resolution a bromine atom is bound to the benzene ring as marker. The $Br\,3d$ peak has a binding energy of $72.8\,\mathrm{eV}$. The charge migration in the benzene ring will influence the electronic environment of the $Br\,3d$ photoemission resulting in a time dependent photoemission response. This shift will be adressed with the attosecond streaking experiments.

The synthesis and characterisation of the molecule is done in the framework of the diploma thesis of Sebastian Herrmann (AK Rehbein,Chemistry Department, Hamburg University).

The bromo-phenylalanin will be investigated with HHG radiation produced in argon. The beam is spectrally filtered with a Zr filter and a $79\,\mathrm{eV}$ multilayer mirror. The reflectivity curve is given in the Appendix B. The multilayer mirror reflects the beam onto the sample surface. The sample is mounted on a manipulator enabling the positioning in all three translational degrees of freedom. Furthermore, the sample is rotatable along the manipulator axis and in the plane of sample surface. A view inside the experimental chamber is illustrated in Figure 7.24.

An XPS analysis of the sample is presented in Figure 7.25. The overview on the left shows Peaks originating from carbon, oxygen, nitrogen, and bromine. With an attosecond XUV pulse of a maximum energy of $95\,\mathrm{eV}$ photoelectreons up to this binding energy can be

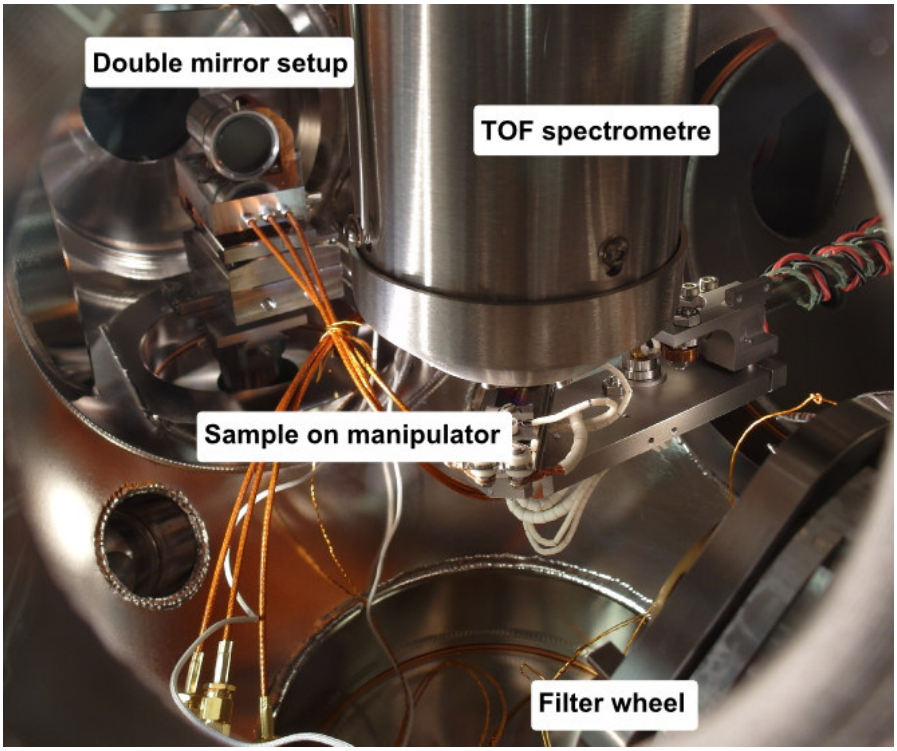

Figure 7.24.: View inside the experimental chamber showing the setup for attostreaking on the photoelectron spectrum of bromo-phenylalanin.

emitted. Some of the occupied orbitals originating from the bromine atom within this energy range are presented in Figure 7.26.

With *SimIon* the expected photoelectron sprectrum can be simulated. The $Br\,3d$ peak has a natural Lorentzian line shape and is located at $(22.2 \pm 1.0)\,\mathrm{eV}$ HWHM. In photoemission by an attosecond pulse, this peak is convoluted with a Gaussian laser pulse $(95 \pm 2)\,\mathrm{eV}$ HWHM (corresponding to a pulse duration of $455\,\mathrm{as}$) resulting in a Voigt distribution. In the simulations it is approximated with a Gaussian particle distribution since this is the determining broadening effect and *SimIon* is restricted to Gaussian or Lorentzian particle distributions. Therefore, $10\,000$ electrons are generated with a Gaussian energy distribution at $(22.2 \pm 2.5)\,\mathrm{eV}$ HWHM.The focus size is assumed with a radial 2D 1σ-Gaussian distribution at of $(1 \pm 1)\,\mu\mathrm{m}$. The particles are produced in the working distance of the TOF at $3\,\mathrm{mm}$ before the entrance cone. The particles are emitted in the full acceptance angle of the TOF of $\pm 30°$. The applied voltages to the lens and drift tube are $120\,\mathrm{V}$ and $-5\,\mathrm{V}$, respectively. The simulated flight times are shown in Figure 7.27 as histogram with a Gaussian fit. The photoelectron wavepacket arrives at a mean flight time with a FWHM spread of:

$$\Delta TOF(Br\,3d) = (134.12 \pm 18.13)\,\mathrm{ns} \tag{7.11}$$

This experiment will be conducted in the near future. We hope to identify the time dependent response in photoemission in the streaking traces and to identify the effect that

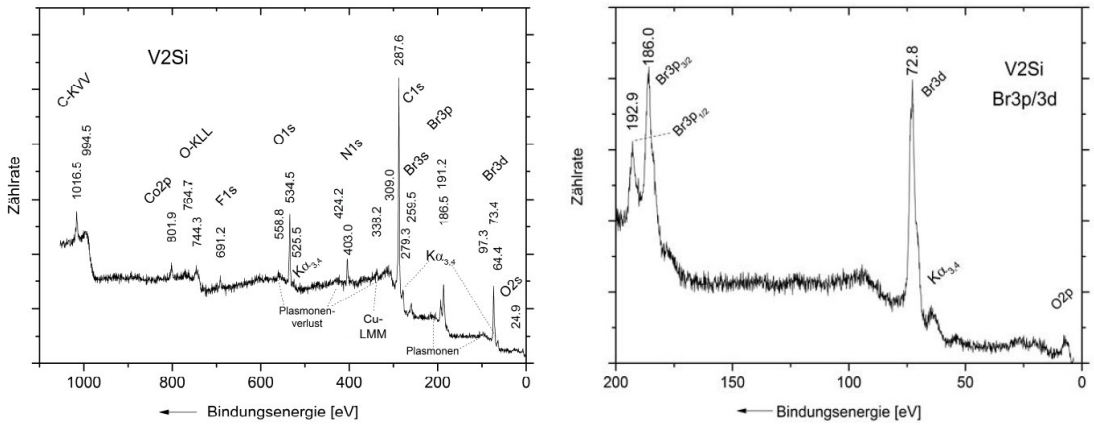

Figure 7.25.: XPS of bromo-phenylalanin (Courtesy of S. Herrmann, Hamburg University).

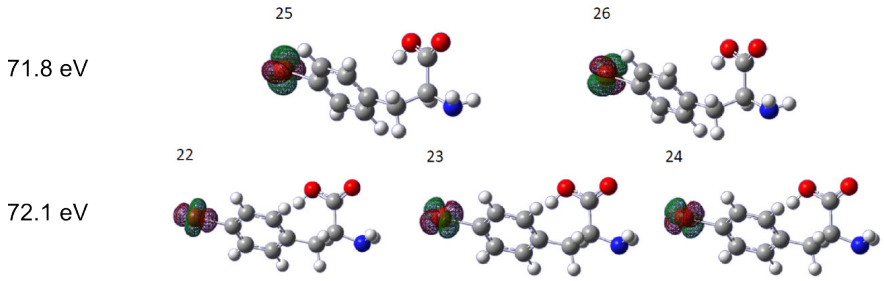

Figure 7.26.: Occupied orbitals of bromo-phenylalanin at binding energies of $71.8\,\mathrm{eV}$ and $72.1\,\mathrm{eV}$ (Courtesy of J. Rehbein, Hamburg University).

could be e.g. an angular dependency or a peak shift resulting in a change of the number or energy of photoelectrons. Since the laser system was commissioned in July 2016, it was not possible to do this experiment earlier.

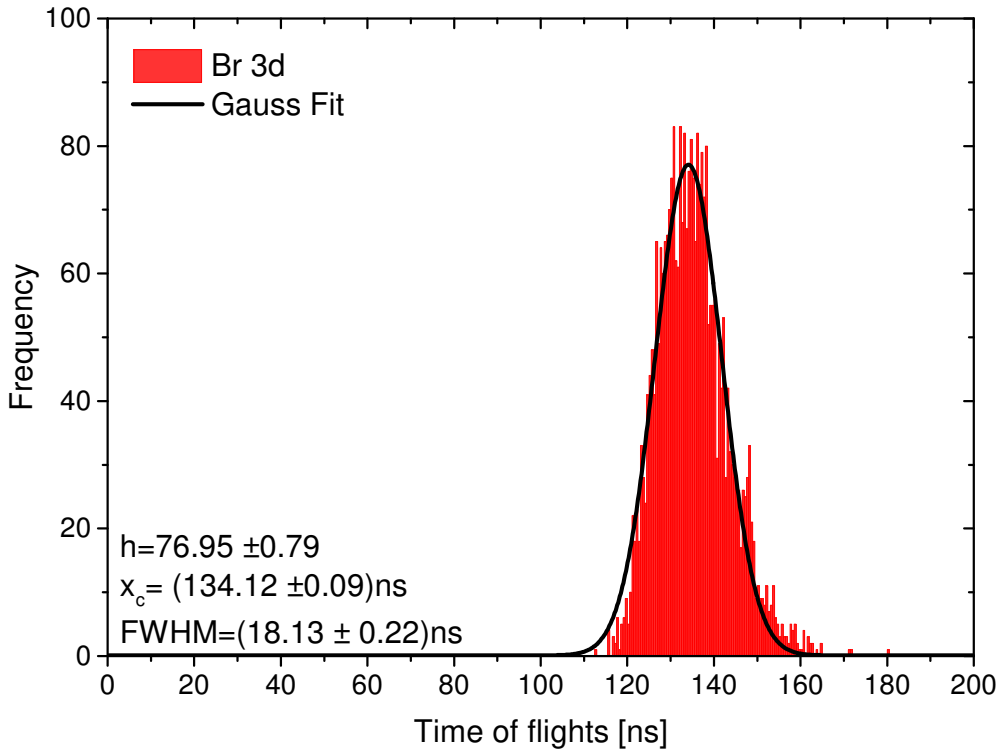

Figure 7.27.: Flight times of Bromo-phenylalanin $Br3d$ photoelectrons excited with quasi-instantaneous emission with $95\,\mathrm{eV}$ photon energy.

8. Conclusion

The goal of this thesis was the investigation of ultrafast phenomena in nanoparticles and thin films. I could demonstrate that utilizing the attosecond streaking technique charge oscillations in plasmonic structures or transportation effects during photoexcitation in thin films can be studied directly in the time domain.

The technology for such experiments is based on ultrafast laser sources with few cycle laser pulses and the frequency conversion to the XUV by high harmonic generation enabling the generation of isolated attosecond pulses. Studying surfaces with photoelectron spectroscopy, ultra high vacuum conditions are required. On the sample side, manufacturing techniques as focused ion beam writing or e-beam lithography are approaching their limit with a few ten nanometer feature sizes. Another difficulty is the design of nanoparticle samples suitable for these experiments in particular regarding orientation of the plasmonic field and the collection efficiency of the time-of-flight detector.

For the realisation of such experiments a HHG beamline was built delivering XUV pulses. It starts with the incoupling of the driving laser with $30\,\mathrm{fs}$ pulse duration at a central pulse wavelength of $795\,\mathrm{nm}$ FWHM. XUV radiation above $79\,\mathrm{eV}$ in argon was produced. Ultrahigh vacuum conditions are reached in the experimental chamber. Three differential pumping stages efficiently pump the gas from the HHG generation and enable a pressure difference between the HHG chamber and experimental chamber of five orders of magnitude. To avoid venting the chamber for inserting new samples, a multi-sample head has been designed that is adapted to the manipulator head. With this, up to six samples can be stored in the chamber. For nanometre stability, all optical elements and the sample are decoupled from vibrations introduced by vacuum pumps.

A proof-of-principle experiment showed the applicability of attosecond streaking to non-crystalline and non-UHV prepared thin film samples. One of the samples was a polycrystalline gold film, the other an amorphous oxidized tungsten film. The samples were stored in ambient conditions before they were inserted into the streaking chamber and into the characterisation instruments. The streaking results for gold showed a photoelectron wavepacket broadening in the interaction zone that can be explained by the emission depth, which is in the order of the inelastic mean-free path. At delay times far behind the NIR-pulse significant deviation from gas phase measurements were found, which are interpreted as plasmonic interactions appearing several ten femtoseconds after excitation by the NIR pulse. The streaking on tungsten trioxide revealed a broader photoelectron wavepacket than from mean-free path calculations. This further broadening can be attributed to electronic interband excitations.

Although streaking measurements have been successfully performed on non-UHV prepared samples, for future investigation of nanostructures a contamination free surface is beneficial for the signal-to-noise ratio. A cleaning strategy was developed based on UV-ozone cleaning where organic contaminants are removed nondestructively and efficient.

Furthermore, plasmonic nanostructures were designed with the target of electron dynamics on ultrashort time-scale. A challenge was tuning of the orientation of the electric field to be accessible by spectroscopy to reveal plasmonic subcycle dynamics on fastest timescales. I simulated and developed hybridised triple layer disk resonators that show surface modes depending on thickness. The mode shapes depend on asymmetry factors like relative disk diameter of the top and bottom disk, thickness of the top disk, and material composition of the outer disks. The modes are excited by the laser pulse and the built up time varies for the different modes. This results in a complex composition with a dynamic propagation direction including phase changes on the timescale of attoseconds.

The XUV pulse duration measurement is a perspective measurement proving the generation of isolated attosecond pulses. After calibrating the TOF with gas phase streaking, first experiments are applicable at the targets characterized in this thesis. For even better vacuum conditions in the experimental chamber, another skimmer aperture can be installed in the first differential pumping stage and the experimental chamber can be baked out for a better background pressure. The realisation of nanodisk resonator samples is already in progress starting from a triple layer film. The attosecond streaking on nanostructured surfaces has never been reported so far. The successful demonstration of streaking on nanostructures like resonators would revolutionize the understanding of plasmonic structures by direct mapping of the electric field in the time domain.

In the future with the described setup electronic dynamics in electron transport in solids can be measured with attosecond time-resolution. This opens the way to new sample classes as opto-electronic devices used in nanoplasmonic devices which will have a huge impact in information technology. The experimental implementation of attosecond photoscopy allows an even better access to this information.

A. Simulation

A.1. Test of simulation environment

In the following simulation of nanodisk sandwiches from *Dmitriev* with different top layer thicknesses [52] are compared to results from the simulation environment of *CST Studio Suite*. In Figure A.1 experimental extinction spectra of a (10-10-10) sandwich are shown in the vertical centre curves in a) and compared to calculations in b). The curves of the (10-10-10) experimental spectra agree qualitatively with the calculated spectra. The peak positions are shifted in the experimental measurements to higher wavelength compared to the calculations. This shift can result from the surface roughness which is most likely not included in the calculations. The electric near fields are presented in d) for three top disk thicknesses

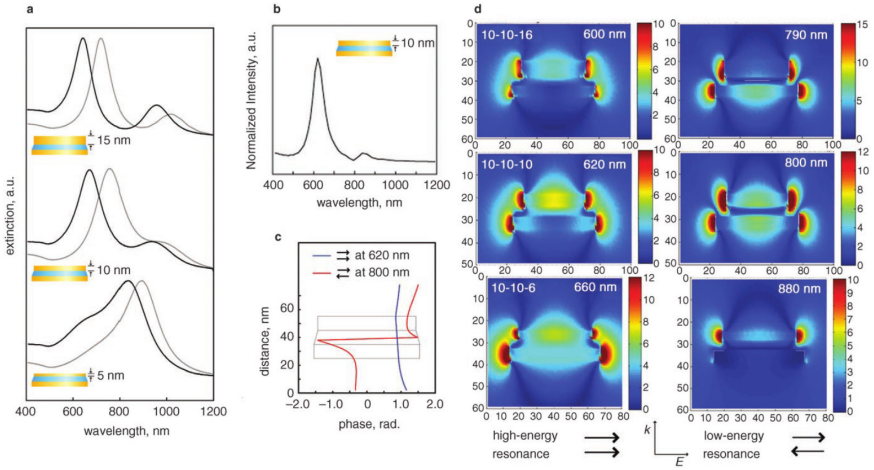

Figure A.1.: Simulation of (10-10-6) to (10-10-16) disk sandwiches with top disk diameter of $88\,\mathrm{nm}$ and bottom disk diameter of $108\,\mathrm{nm}$ [52].

excited with monochromatic light with the resonance wavelength. In the (vertical) centre images the (10-10-10) sandwiches are shown. The electric field in the spacing layer disk differs. In the low energy resonance, the field decreases to zero in the center of the spacing layer, which is not the case for the high energy resonance. This is explained by the phase shown in c). The phase of the long energy resonance is shifted within the spacing layer thickness by approximately $3\,\mathrm{rad}$ whereas the phase of the high energy resonance is almost constant over the the spacing layer thickness.

These results were reproduced with *CST Studio Suite* and presented in Figure A.2.

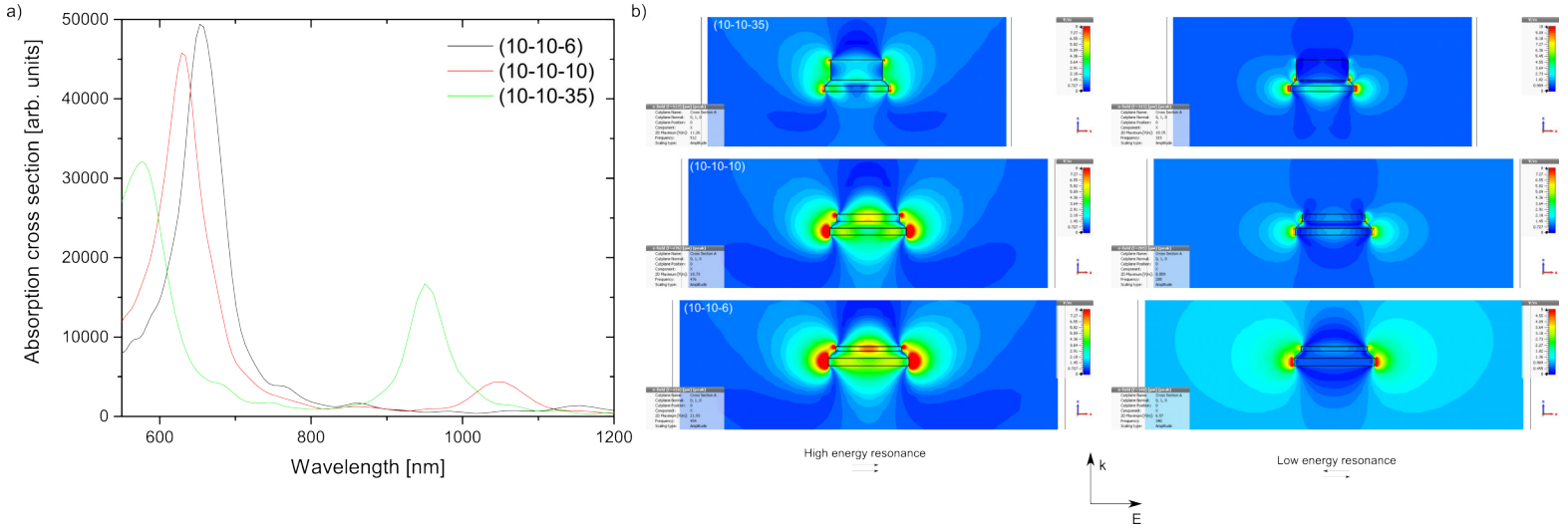

Figure A.2.: Simulation of (10-10-6) to (10-10-36) disk sandwiches with top disk diameter of $88\,\mathrm{nm}$ and bottom disk diameter of $108\,\mathrm{nm}$ with *CST Studio Suite*.

The absorption absorption cross sections for three top layer thicknesses are shown in a). The results correspond to the extinction spectra calculated and measurend by *Dmitriev* qualitatively. Also the electric field at the (10-10-10) sample could be reproduced with the phase shift in the spacing layer. The phase is presented as a false-colour plot in Figure A.3.

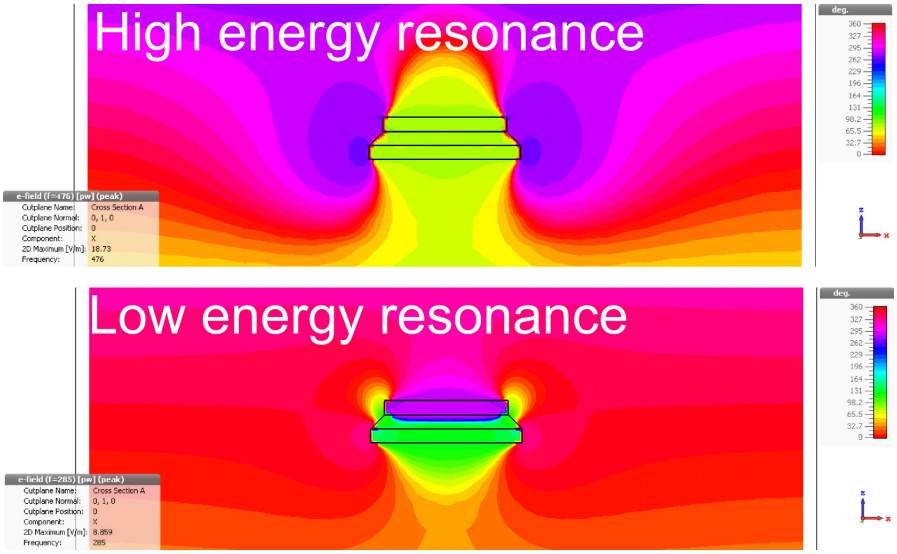

Figure A.3.: Phase of the electric field of the (10-10-10) disk sandwiches calculated with *CST Studio Suite.*

By reproducing the results from [52] the simulation environment is expected to be stable and to deliver reliable results.

A.2. Sample geometries

A.2.1. Au-SiO2-Au Sandwich

The sample geometry of the gold-silica-gold nanosandwich are shown in the following table:

Layer	Material	Radius	Thickness
1	Gold	54 nm	1 nm to 3 nm
2	Silica	adaptive 44 nm to 54 nm	10 nm
3	Gold	44 nm	10 nm

A.2.2. Au-SiO2-Ag Sandwich

The sample geometry of the gold-silica-silver nanosandwich are shown in the following table:

Layer	Material	Radius	Thickness
1	Silver	54 nm	1 nm
2	Silica	adaptive 44 nm to 54 nm	5 nm to 10 nm
3	Gold	44 nm	10 nm

A.3. Optical data of materials

The optical data for calculating ϵ' and ϵ'' are used from the CST database. The database uses the experimental data from [139] for gold and silica, and from [140] for silver. The complex permittivity is obtained from optical quantities with using the Kramers-Kronig-Relation:

$$(n + ik)^2 = (\epsilon'_r + i\epsilon''_r)\mu_r \tag{A.1}$$

For non-magnetic materials $\mu_R = 1$ one obtains:

$$\epsilon'_r = n^2 - k^2 \tag{A.2}$$

$$\epsilon''_r = 2nk \tag{A.3}$$

The complex permittivities for gold, silver, and silica are shown in Figures A.4, A.5, and A.6, respectively.

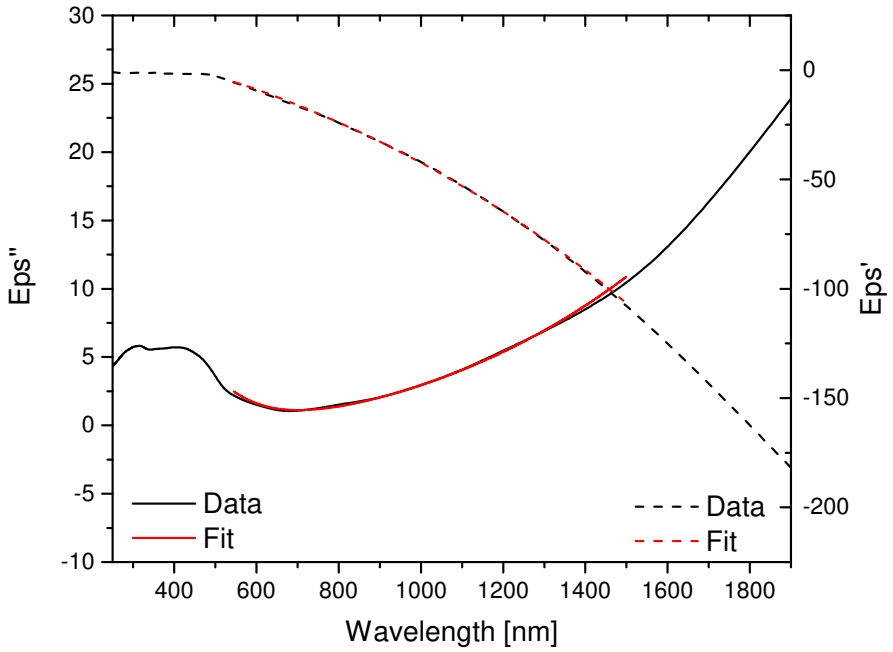

Figure A.4.: Complex permittivity of gold, experimental data obtained from [139] with CST fit.

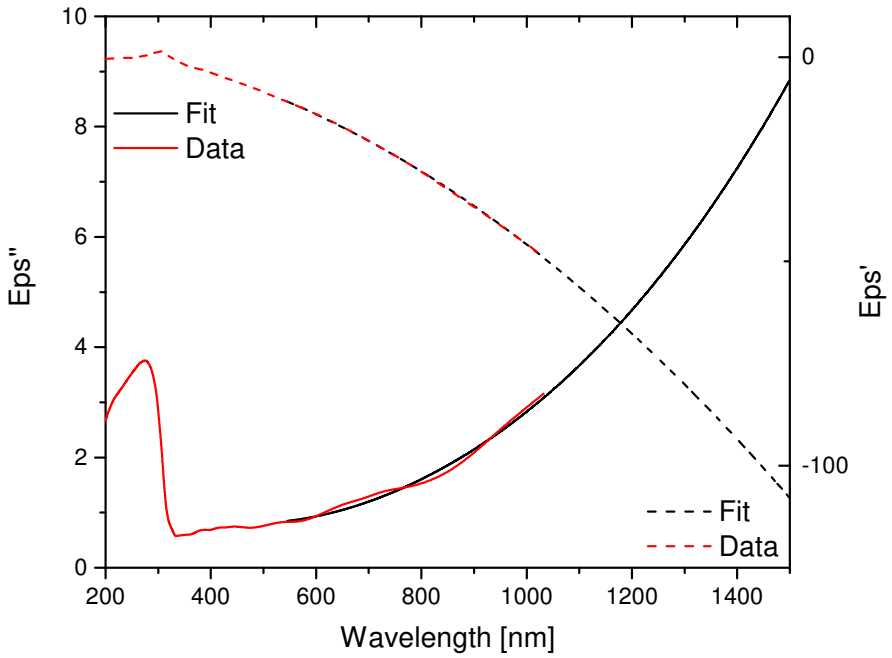

Figure A.5.: Complex permittivity of silica, experimental data obtained from [140] with CST fit.

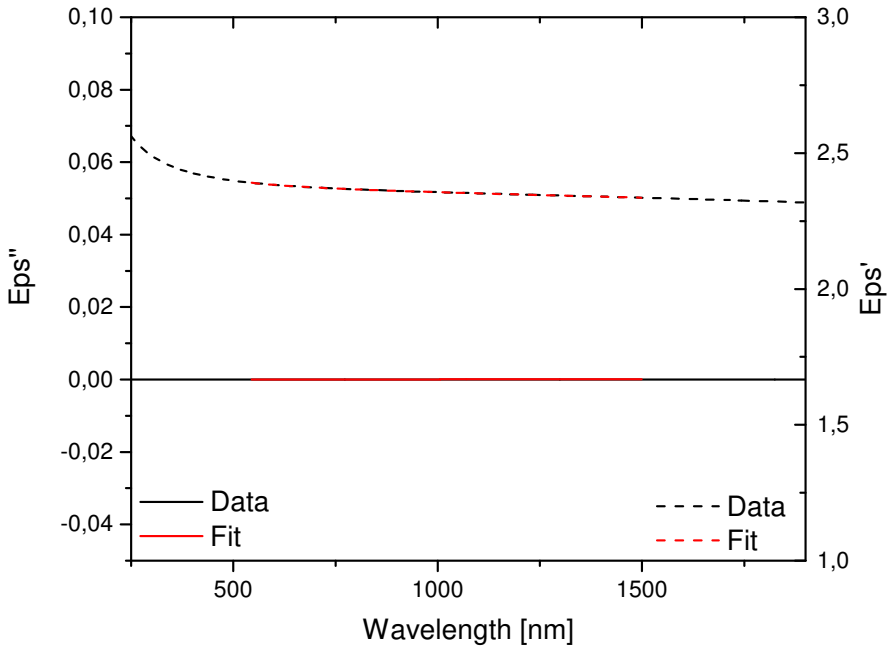

Figure A.6.: Complex permittivity of silica, experimental data obtained from [139] with CST fit.

B. Mirror Reflectivities

B.1. $95\,\mathrm{eV}$ multilayer mirror

The multilayer is composed of molybdenum and silicon layers:

Substrate material	fused silica
Coating	Mo/Si
Focal length	$180\,\mathrm{mm}$
incidence angle	$5°$
γ ratio	0.5
period thickness	$6.75\,\mathrm{nm}$

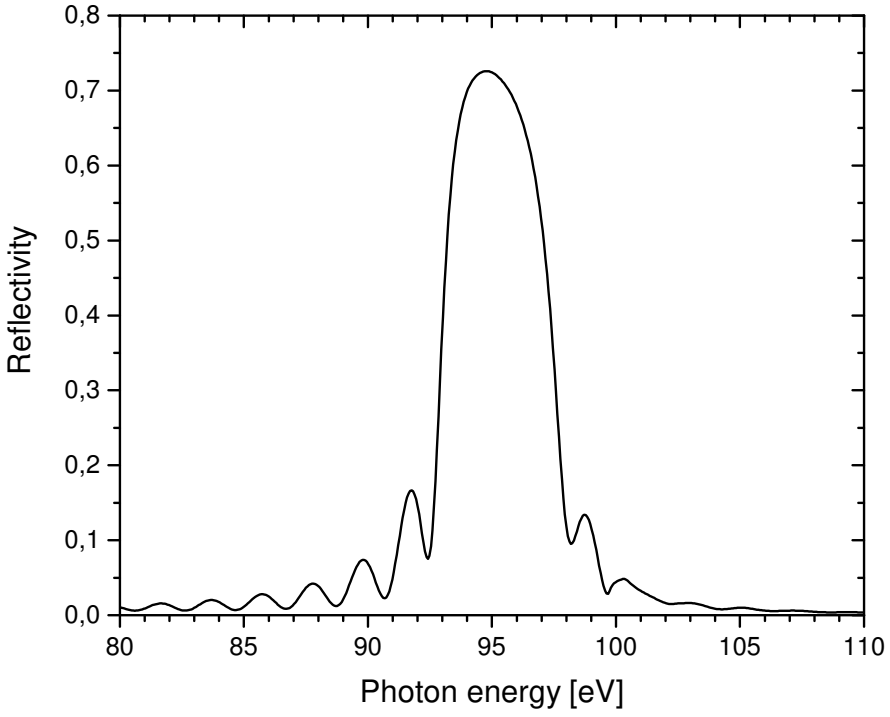

Figure B.1.: Mirror reflectivity of the $95\,\mathrm{eV}$ mirror.

By Fourier transformation of the mirror reflectivity from B.1 one obtains the temporal duration of the pulse shown in B.2. The estimated pulse duration with the Time-Bandwidth

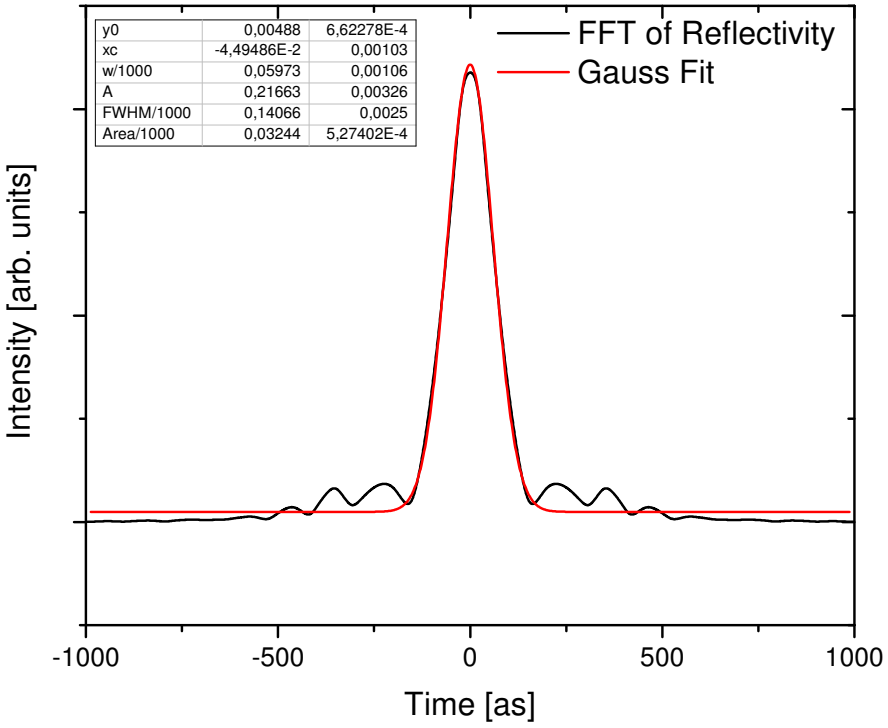

Figure B.2.: Resulting pulse duration of the $95\,\mathrm{eV}$ mirror.

product is calculated to:

$$\delta\nu = 1.94 \times 10^{15}\,\mathrm{Hz}$$
$$\tau \leq \frac{0.441}{1.94 \times 10^{15}\,\mathrm{Hz}} \leq 227\,\mathrm{as}$$

B.2. 79 eV multilayer mirror

The reflectivity of the multilayer is:

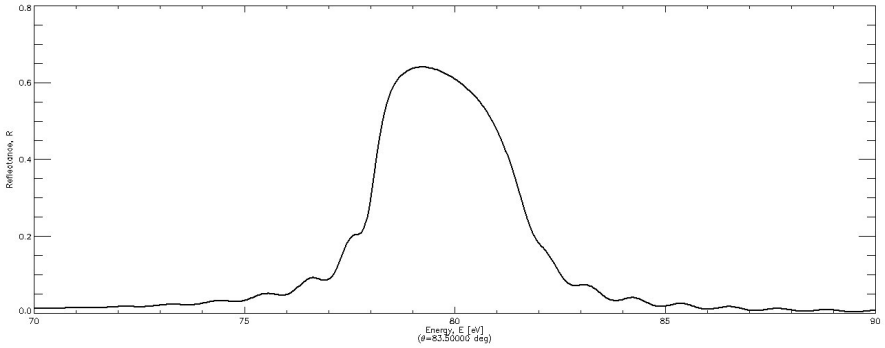

Figure B.3.: Mirror reflectivity of the 79 eV mirror.

C. HHG Incoupling

Element	Distance mm	Angle °	Radius of curvature mm
Mirror 1	80	45	-
Mirror 2	130	40	-
Focusing Mirror	80	10	1000
Mirror 4	50	40	-
Mirror 5	140	45	-
Window	0.2	-	-
Focus	230.1	-	-

Table C.1.: Geometrical parameters used for the incoupling into the HHG chamber

D. Time of flight electron spectrometer

For $3\,\mathrm{mm}$ distance between the sample and entrance aperture the Time of flight is correlated to the electron energy as shown in Figure D.1

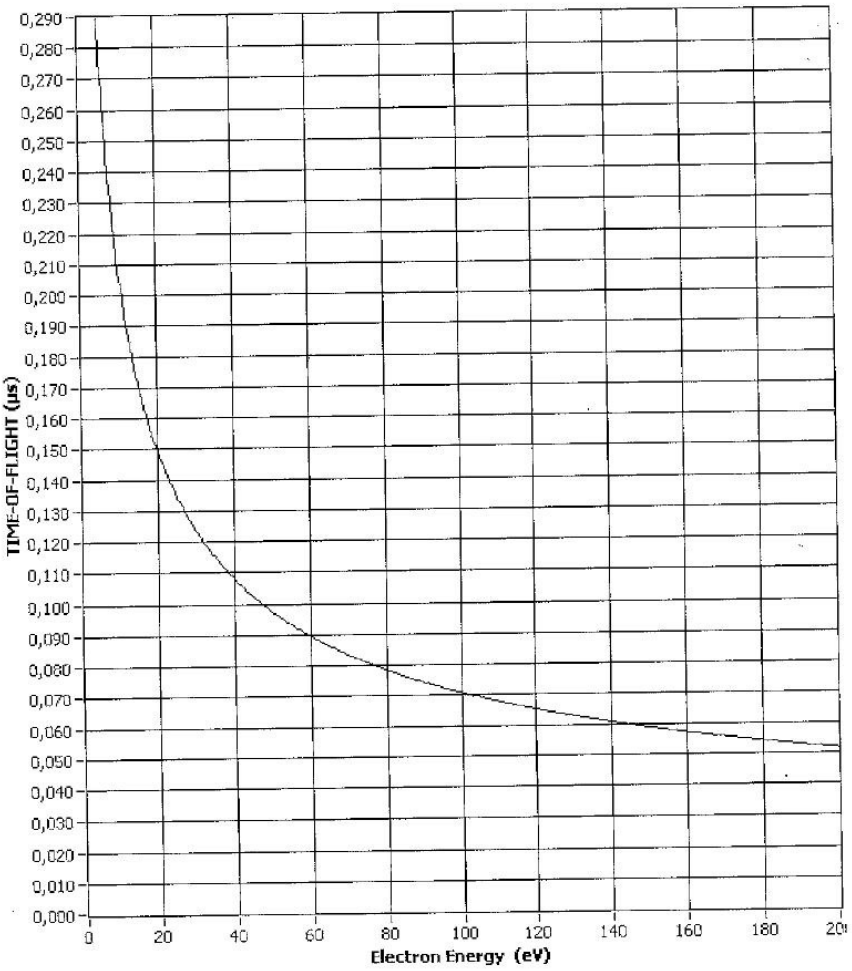

Figure D.1.: Correlation of Time of flights and electron energy for the Stefan Kaesdorf time of flight spectrometer used in the attosecond streaking beamline.

List of Figures

Bibliography

[1] I. Freestone, N. Meeks, M. Sax, and C. Higgitt. The Lycurgus Cup — A Roman nanotechnology. *Gold Bull.*, 40(4):270–277, dec 2007. ISSN 0017-1557. doi: 10.1007/BF03215599. URL http://link.springer.com/10.1007/BF03215599.

[2] D. Bohm and D. Pines. A Collective Description of Electron Interactions: III. Coulomb Interactions in a Degenerate Electron Gas. *Phys. Rev.*, 92(3):609–625, nov 1953. ISSN 0031-899X. doi: 10.1103/PhysRev.92.609. URL http://link.aps.org/doi/10.1103/PhysRev.92.609.

[3] Erwin Kretschmann. *Untersuchungen zur Anregung und Streuung von Oberflächenplasmaschwingungen an Silberschichten*. Dissertation, Hamburg, 1972.

[4] Andreas Otto. Spectroscopy of surface polaritons by attenuated total reflection. In *Opt. Prop. solids*, page 678. North Holland, Amsterdam, seraphin, edition, 1976.

[5] D. Peer, J. M. Karp, S. Hong, O. C. Farokhzad, R. Margalit, and R. Langer. Nanocarriers as an emerging platform for cancer therapy. *Nat. Nanotechnol.*, 2 (12):751–760, dec 2007. ISSN 1748-3387. doi: 10.1038/nnano.2007.387. URL http://www.nature.com/doifinder/10.1038/nnano.2007.387.

[6] X. Huang, I. H. El-Sayed, W. Qian, and M. A. El-Sayed. Cancer Cell Imaging and Photothermal Therapy in the Near-Infrared Region by Using Gold Nanorods. *J. Am. Chem. Soc.*, 128(6):2115–2120, feb 2006. ISSN 0002-7863. doi: 10.1021/ja057254a. URL http://pubs.acs.org/doi/abs/10.1021/ja057254a.

[7] X. Qian, X.-H. Peng, D. O. Ansari, Q. Yin-Goen, G. Z. Chen, D. M. Shin, L. Yang, A. N. Young, M. D. Wang, and S. Nie. In vivo tumor targeting and spectroscopic detection with surface-enhanced Raman nanoparticle tags. *Nat. Biotechnol.*, 26(1):83–90, dec 2007. ISSN 1087-0156. doi: 10.1038/nbt1377. URL http://www.ncbi.nlm.nih.gov/pubmed/18157119http://www.nature.com/doifinder/10.1038/nbt1377.

[8] G. Peng, U. Tisch, O. Adams, M. Hakim, N. Shehada, Y. Y. Broza, S. Billan, R. Abdah-Bortnyak, A. Kuten, and H. Haick. Diagnosing lung cancer in exhaled breath using gold nanoparticles. *Nat. Nanotechnol.*, 4:669–673, nov 2009. ISSN 1748-3387. doi: 10.1038/nnano.2009.235. URL http://dx.doi.org/10.1038/nnano.2009.235http://www.nature.com/doifinder/10.1038/nnano.2009.235.

[9] M. L. Brongersma and V. M. Shalaev. The Case for Plasmonics. *Science (80-.).*, 328:440–441, apr 2010. ISSN 0036-8075. doi: 10.1126/science.1186905. URL http://www.sciencemag.org/cgi/doi/10.1126/science.1186905.

[10] R. Zia, J. A. Schuller, A. Chandran, and M. L. Brongersma. Plasmonics: the next chip-scale technology. *Mater. Today*, 9(7-8):20–27, jul 2006. ISSN 13697021. doi: 10.1016/S1369-7021(06)71572-3. URL http://linkinghub.elsevier.com/retrieve/pii/S1369702106715723.

[11] E Ozbay. Plasmonics: Merging Photonics and Electronics at Nanoscale Dimensions. *Science (80-.).*, 311:189–193, jan 2006. ISSN 0036-8075. doi: 10.1126/science.1114849. URL http://www.sciencemag.org/cgi/doi/10.1126/science.1114849.

[12] E. E. Krasovskii, C. Friedrich, W. Schattke, and P. M. Echenique. Rapid propagation of a Bloch wave packet excited by a femtosecond ultraviolet pulse. *Phys. Rev. B*, 94 (19):195434, nov 2016. ISSN 2469-9950. doi: 10.1103/PhysRevB.94.195434. URL http://link.aps.org/doi/10.1103/PhysRevB.94.195434.

[13] A. G. Borisov, D. Sánchez-Portal, A. K. Kazansky, and P. M. Echenique. Resonant and nonresonant processes in attosecond streaking from metals. *Phys. Rev. B*, 87 (12):121110, mar 2013. ISSN 1098-0121. doi: 10.1103/PhysRevB.87.121110. URL http://link.aps.org/doi/10.1103/PhysRevB.87.121110.

[14] R. D. Muino, D. Sanchez-Portal, V. M. Silkin, E. V. Chulkov, and P. M. Echenique. Time-dependent electron phenomena at surfaces. *Proc. Natl. Acad. Sci.*, 108(3): 971–976, jan 2011. ISSN 0027-8424. doi: 10.1073/pnas.1008517107. URL http://www.pnas.org/cgi/doi/10.1073/pnas.1008517107.

[15] M. Drescher, M. Hentschel, R. Kienberger, M. Uiberacker, V. Yakovlev, A. Scrinzi, Th. Westerwalbesloh, U. Kleineberg, U. Heinzmann, and F. Krausz. Time-resolved atomic inner-shell spectroscopy. *Nature*, 419:803–807, oct 2002. ISSN 0028-0836. doi: 10.1038/nature01143. URL http://www.ncbi.nlm.nih.gov/pubmed/12397349http://www.nature.com/doifinder/10.1038/nature01143.

[16] M. Uiberacker, Th. Uphues, M. Schultze, A. J. Verhoef, V. Yakovlev, M. F. Kling, J. Rauschenberger, N. M. Kabachnik, H. Schröder, M. Lezius, K. L. Kompa, H.-G. Muller, M. J. J. Vrakking, S. Hendel, U. Kleineberg, U. Heinzmann, M. Drescher, and F. Krausz. Attosecond real-time observation of electron tunnelling in atoms. *Nature*, 446(7136):627–632, apr 2007. ISSN 0028-0836. doi: 10.1038/nature05648. URL http://ieeexplore.ieee.org/document/4386274/http://www.nature.com/doifinder/10.1038/nature05648.

[17] V. Despré, A. Marciniak, V. Loriot, M. C. E. Galbraith, A. Rouzée, M. J. J. Vrakking, F. Lépine, and A. I. Kuleff. Attosecond Hole Migration in Benzene Molecules Surviving Nuclear Motion. *J. Phys. Chem. Lett.*, 6(3):426–431, feb 2015. ISSN 1948-7185. doi: 10.1021/jz502493j. URL http://pubs.acs.org/doi/abs/10.1021/jz502493j.

[18] G. Sansone, F. Kelkensberg, J. F. Pérez-Torres, F. Morales, M. F. Kling, W. Siu, O. Ghafur, P. Johnsson, M. Swoboda, E. Benedetti, F. Ferrari, F. Lépine, J. L. Sanz-Vicario, S. Zherebtsov, I. Znakovskaya, A. L'Huillier, M. Yu Ivanov, M. Nisoli,

F. Martín, and M. J. J. Vrakking. Electron localization following attosecond molecular photoionization. *Nature*, 465(7299):763–766, jun 2010. ISSN 0028-0836. doi: 10.1038/nature09084. URL http://www.nature.com/doifinder/10.1038/nature09084http://www.ncbi.nlm.nih.gov/pubmed/20535207.

[19] F. Kelkensberg, C. Lefebvre, W. Siu, O. Ghafur, T. T. Nguyen-Dang, O. Atabek, A. Keller, V. Serov, P. Johnsson, M. Swoboda, T. Remetter, A. L'Huillier, S. Zherebtsov, G. Sansone, E. Benedetti, F. Ferrari, M. Nisoli, F. Lépine, M. F. Kling, and M. J J Vrakking. Molecular Dissociative Ionization and Wave-Packet Dynamics Studied Using Two-Color XUV and IR Pump-Probe Spectroscopy. *Phys. Rev. Lett.*, 103(12):123005, sep 2009. ISSN 0031-9007. doi: 10.1103/PhysRevLett.103.123005. URL http://link.aps.org/doi/10.1103/PhysRevLett.103.123005.

[20] S. Neppl, R. Ernstorfer, E. M. Bothschafter, a. L. Cavalieri, D. Menzel, J. V. Barth, F. Krausz, R. Kienberger, and P. Feulner. Attosecond Time-Resolved Photoemission from Core and Valence States of Magnesium. *Phys. Rev. Lett.*, 109(8):087401, aug 2012. ISSN 0031-9007. doi: 10.1103/PhysRevLett.109.087401. URL http://link.aps.org/doi/10.1103/PhysRevLett.109.087401.

[21] S. Neppl, R. Ernstorfer, A. L. Cavalieri, C. Lemell, G. Wachter, E. Magerl, E. M. Bothschafter, M. Jobst, M. Hofstetter, U. Kleineberg, J. V. Barth, D. Menzel, J. Burgdörfer, P. Feulner, F. Krausz, and R. Kienberger. Direct observation of electron propagation and dielectric screening on the atomic length scale. *Nature*, 517:342–346, jan 2015. ISSN 0028-0836. doi: 10.1038/nature14094. URL http://www.nature.com/nature/journal/v517/n7534/abs/nature14094.html{%}5Cnhttp://www.nature.com/nature/journal/v517/n7534/pdf/nature14094.pdfhttp://www.nature.com/doifinder/10.1038/nature14094.

[22] W. A. Okell, T. Witting, D. Fabris, C. A. Arrell, J. Hengster, S. Ibrahimkutty, A. Seiler, M. Barthelmess, S. Stankov, D. Y. Lei, Y. Sonnefraud, M. Rahmani, T. Uphues, S. A. Maier, J. P. Marangos, and J. W. G. Tisch. Temporal broadening of attosecond photoelectron wavepackets from solid surfaces. *Optica*, 2(4):383, apr 2015. ISSN 2334-2536. doi: 10.1364/OPTICA.2.000383. URL https://www.osapublishing.org/abstract.cfm?URI=optica-2-4-383.

[23] D. Strickland and G. Mourou. Compression of amplified chirped optical pulses. *Opt. Commun.*, 56(3):219–221, dec 1985. ISSN 00304018. doi: 10.1016/0030-4018(85)90120-8. URL http://linkinghub.elsevier.com/retrieve/pii/0030401885901208.

[24] M. Krebs, S. Hädrich, S. Demmler, J. Rothhardt, A. Zaïr, L. Chipperfield, J. Limpert, and A. Tünnermann. Towards isolated attosecond pulses at megahertz repetition rates. *Nat. Photonics*, 7(7):555–559, jun 2013. ISSN 1749-4885. doi: 10.1038/nphoton.2013.131. URL http://www.nature.com/doifinder/10.1038/nphoton.2013.131.

[25] S.-W. Huang, G. Cirmi, J. Moses, K.-H. Hong, S. Bhardwaj, J. R. Birge, L.-J. Chen, E. Li, B. J. Eggleton, G. Cerullo, and F. X. Kärtner. High-energy pulse synthesis with sub-cycle waveform control for strong-field physics. *Nat. Photonics*, 5(8):475–479, jul 2011. ISSN 1749-4885. doi: 10.1038/nphoton.2011.140. URL http://www.nature.com/doifinder/10.1038/nphoton.2011.140.

[26] G. Sansone, E. Benedetti, F. Calegari, C. Vozzi, L. Avaldi, R. Flammini, L. Poletto, P. Villoresi, C. Altucci, R. Velotta, S. Stagira, S. De Silvestri, and M. Nisoli. Isolated Single-Cycle Attosecond Pulses. *Science (80-.).*, 314:443–446, oct 2006. ISSN 0036-8075. doi: 10.1126/science.1132838. URL http://www.sciencemag.org/cgi/doi/10.1126/science.1132838.

[27] M. Chini, K. Zhao, and Z. Chang. The generation, characterization and applications of broadband isolated attosecond pulses. *Nat. Photonics*, 8:178–186, feb 2014. ISSN 1749-4885. doi: 10.1038/nphoton.2013.362. URL http://www.nature.com/doifinder/10.1038/nphoton.2013.362.

[28] E. Goulielmakis, V. S. Yakovlev, A. L. Cavalieri, M. Uiberacker, V. Pervak, A. Apolonski, R. Kienberger, U. Kleineberg, and F. Krausz. Attosecond Control and Measurement: Lightwave Electronics. *Science (80-.).*, 317:769–775, aug 2007. ISSN 0036-8075. doi: 10.1126/science.1142855. URL http://www.sciencemag.org/cgi/doi/10.1126/science.1142855.

[29] J. Itatani, F. Quéré, G. L. Yudin, M. Yu. Ivanov, F. Krausz, and P. B. Corkum. Attosecond Streak Camera. *Phys. Rev. Lett.*, 88(17):173903, apr 2002. ISSN 0031-9007. doi: 10.1103/PhysRevLett.88.173903. URL http://link.aps.org/doi/10.1103/PhysRevLett.88.173903.

[30] K. Zhao, Q. Zhang, M. Chini, Y. Wu, X. Wang, and Z. Chang. Tailoring a 67 attosecond pulse through advantageous phase-mismatch. *Opt. Lett.*, 37(18):3891, sep 2012. ISSN 0146-9592. doi: 10.1364/OL.37.003891. URL https://www.osapublishing.org/abstract.cfm?URI=ol-37-18-3891.

[31] R. W. Wood. On a Remarkable Case of Uneven Distribution of Light in a Diffraction Grating Spectrum. *Proc. Phys. Soc. London*, 18(1): 269–275, jun 1902. ISSN 1478-7814. doi: 10.1088/1478-7814/18/1/325. URL http://stacks.iop.org/1478-7814/18/i=1/a=325?key=crossref.7ebbe1383fb00dffe4b52e1569cdd953.

[32] L. Rayleigh. On the Dynamical Theory of Gratings. *Proc. R. Soc. A Math. Phys. Eng. Sci.*, 79(532):399–416, aug 1907. ISSN 1364-5021. doi: 10.1098/rspa.1907.0051. URL http://rspa.royalsocietypublishing.org/cgi/doi/10.1098/rspa.1983.0054http://rspa.royalsocietypublishing.org/cgi/doi/10.1098/rspa.1907.0051.

[33] U. Fano. The Theory of Anomalous Diffraction Gratings and of Quasi-Stationary Waves on Metallic Surfaces (Sommerfeld's Waves). *J. Opt.*

Soc. Am., 31(3):213, mar 1941. ISSN 0030-3941. doi: 10.1364/JOSA.31.000213. URL http://www.opticsinfobase.org/abstract.cfm?URI=josa-31-3-213{%}5Cnhttp://www.opticsinfobase.org/DirectPDFAccess/9532F14D-C272-39F0-C249EA23E9643768{_}49385/josa-31-3-213.pdf?da=1{&}id=49385{&}seq=0{&}mobile=no{%}5Cnhttp://www.opticsinfobase.org/josa/abstract.cfm?uri=.

[34] C. F. Bohren and D. P. Huffman. *Absorption and scattering of light by small particles*. New York, 1983.

[35] R. Feynman, M. Sands, and R. Leighton. *The Feynman Lectures on Physics, Volume II*. Addison-Weslay, 1964.

[36] G. Mie. Beiträge zur Optik trüber Medien, speziell kolloidaler Metallösungen. *Ann. Phys.*, 330(3):377–445, 1908. ISSN 00033804. doi: 10.1002/andp.19083300302. URL http://dx.doi.org/10.1002/andp.19083300302http://doi.wiley.com/10.1002/andp.19083300302.

[37] W. Hergert and T. Wriedth. *The Mie Theory*. Springer Berlin Heidelberg, 1 edition, 2012.

[38] Stefan A. Maier. *Plasmonics: Fundamentals and Applications*. Springer Science+Business Media LLC, New York, 2007. ISBN 9780387331508.

[39] M. A. Ordal, R. J. Bell, R. W. Alexander, L. L. Long, and M. R. Querry. Optical properties of fourteen metals in the infrared and far infrared: Al, Co, Cu, Au, Fe, Pb, Mo, Ni, Pd, Pt, Ag, Ti, V, and W. *Appl. Opt.*, 24(24):4493, dec 1985. ISSN 0003-6935. doi: 10.1364/AO.24.004493. URL http://ao.osa.org/abstract.cfm?URI=ao-24-24-4493https://www.osapublishing.org/abstract.cfm?URI=ao-24-24-4493.

[40] Ansgar Liebsch. *Electronic Excitations at Metal Surfaces*. New York, 1997.

[41] A. Yelon, K.N. Piyakis, and E. Sacher. Surface plasmons in Drude metals. *Surf. Sci.*, 569(1-3):47–55, oct 2004. ISSN 00396028. doi: 10.1016/j.susc.2004.07.028. URL http://linkinghub.elsevier.com/retrieve/pii/S0039602804009495.

[42] F. Goos and H. Hänchen. Über das Eindringen des totalreflektierten Lichtes in das dünnere Medium. *Ann. Phys.*, 435(5):383–392, 1943. ISSN 00033804. doi: 10.1002/andp.19434350504. URL http://doi.wiley.com/10.1002/andp.19434350504.

[43] W. L. Barnes, T. W. Preist, S. C. Kitson, and J. R. Sambles. Physical origin of photonic energy gaps in the propagation of surface plasmons on gratings. *Phys. Rev. B*, 54(9):6227–6244, sep 1996. ISSN 0163-1829. doi: 10.1103/PhysRevB.54.6227. URL http://link.aps.org/doi/10.1103/PhysRevB.54.6227.

[44] E.L. Hu, M. Brongersma, and A. Baca. Applications: nanophotonics and plasmonics. chapter 9, pages 318–340. 2011.

[45] M. W. Knight, H. Sobhani, P. Nordlander, and N. J. Halas. Photodetection with Active Optical Antennas. *Science (80-.).*, 332(6030):702–704, may 2011. ISSN 0036-8075. doi: 10.1126/science.1203056. URL http://www.sciencemag.org/cgi/doi/10.1126/science.1203056{%}5Cnhttp://www.ncbi.nlm.nih.gov/pubmed/21551059http://www.sciencemag.org/cgi/doi/10.1126/science.1203056.

[46] E. C. Dreaden, A. M. Alkilany, X. Huang, C. J. Murphy, and M. A. El-Sayed. The golden age: gold nanoparticles for biomedicine. *Chem. Soc. Rev.*, 41(7):2740–2779, 2012. ISSN 0306-0012. doi: 10.1039/C1CS15237H. URL http://xlink.rsc.org/?DOI=C1CS15237H.

[47] P. Bharadwaj, B. Deutsch, and L. Novotny. Optical Antennas. *Adv. Opt. Photonics*, 1(3):438, nov 2009. ISSN 1943-8206. doi: 10.1364/AOP.1.000438. URL http://www.opticsinfobase.org/abstract.cfm?URI=aop-1-3-438https://www.osapublishing.org/aop/abstract.cfm?uri=aop-1-3-438.

[48] E. Prodan. A Hybridization Model for the Plasmon Response of Complex Nanostructures. *Science (80-.).*, 302:419–422, oct 2003. ISSN 0036-8075. doi: 10.1126/science.1089171. URL http://www.ncbi.nlm.nih.gov/pubmed/14564001http://www.sciencemag.org/cgi/doi/10.1126/science.1089171.

[49] H. Wang, D. W. Brandl, F. Le, P. Nordlander, and N. J. Halas. Nanorice: A Hybrid Plasmonic Nanostructure. *Nano Lett.*, 6(4):827–832, apr 2006. ISSN 1530-6984. doi: 10.1021/nl060209w. URL http://pubs.acs.org/doi/abs/10.1021/nl060209w.

[50] F. Hao, C. L. Nehl, J. H. Hafner, and P. Nordlander. Plasmon Resonances of a Gold Nanostar. *Nano Lett.*, 7(3):729–732, mar 2007. ISSN 1530-6984. doi: 10.1021/nl062969c. URL http://pubs.acs.org/doi/abs/10.1021/nl062969c.

[51] M. Frederiksen, V. E. Bochenkov, R. Ogaki, and D. S. Sutherland. Onset of Bonding Plasmon Hybridization Preceded by Gap Modes in Dielectric Splitting of Metal Disks. *Nano Lett.*, 13(12):6033–6039, dec 2013. ISSN 1530-6984. doi: 10.1021/nl4032567. URL http://pubs.acs.org/doi/abs/10.1021/nl4032567.

[52] A. Dmitriev, T. Pakizeh, M. Käll, and D. S. Sutherland. Gold–Silica–Gold Nanosandwiches: Tunable Bimodal Plasmonic Resonators. *Small*, 3(2):294–299, feb 2007. ISSN 16136810. doi: 10.1002/smll.200600409. URL http://doi.wiley.com/10.1002/smll.200600409.

[53] R. E. Dietz, M. Campagna, J. N. Chazalviel, and H. R. Shanks. Inelastic electron scattering by intra- and interband plasmons in rhenium trioxide, tungsten trioxide, and some tungsten bronzes. *Phys. Rev. B*, 17(10):3790–3800, may 1978. ISSN 0163-1829. doi: 10.1103/PhysRevB.17.3790. URL http://link.aps.org/doi/10.1103/PhysRevB.17.3790.

[54] K. Sturm and L. E. Oliveira. Theory of a zone-boundary collective state in A1: A model calculation. *Phys. Rev. B*, 30(8):4351–4365, oct 1984. ISSN 0163-

1829. doi: 10.1103/PhysRevB.30.4351. URL http://link.aps.org/doi/10.1103/PhysRevB.30.4351.

[55] K. Sturm and L. E. Oliveira. Band-structure-dependent collective states in simple metals. *Phys. Rev. B*, 40(6):3672–3681, aug 1989. ISSN 0163-1829. doi: 10.1103/PhysRevB.40.3672. URL http://link.aps.org/doi/10.1103/PhysRevB.40.3672.

[56] A. Schiffrin, T. Paasch-Colberg, N. Karpowicz, V. Apalkov, D. Gerster, S. Mühlbrandt, M. Korbman, J. Reichert, M. Schultze, S. Holzner, J. V. Barth, R. Kienberger, R. Ernstorfer, V. S. Yakovlev, M. I. Stockman, and F. Krausz. Optical-field-induced current in dielectrics. *Nature*, 493(7430):70–74, dec 2013. ISSN 0028-0836. doi: 10.1038/nature11567. URL http://dx.doi.org/10.1038/nature11567http://www.nature.com/doifinder/10.1038/nature11567.

[57] M. Schultze, E. M. Bothschafter, A. Sommer, S. Holzner, W. Schweinberger, M. Fiess, M. Hofstetter, R. Kienberger, V. Apalkov, V. S. Yakovlev, M. I. Stockman, and F. Krausz. Controlling dielectrics with the electric field of light. *Nature*, 493:75–78, dec 2012. ISSN 0028-0836. doi: 10.1038/nature11720. URL http://www.ncbi.nlm.nih.gov/pubmed/23222519http://www.nature.com/doifinder/10.1038/nature11720.

[58] C.F. Powell, J.H. Oxley, and J.M. Blocher. Vapor Deposition. *J. Electrochem. Soc.*, 113(10), 1966.

[59] T. Suntola. Atomic layer epitaxy. *Thin Solid Films*, 216(1):84–89, aug 1992. ISSN 00406090. doi: 10.1016/0040-6090(92)90874-B. URL http://linkinghub.elsevier.com/retrieve/pii/004060909290874B.

[60] L.A. Giannuzzi and F.A. Stevie. A review of focused ion beam milling techniques for TEM specimen preparation. *Micron*, 30(3):197–204, jun 1999. ISSN 09684328. doi: 10.1016/S0968-4328(99)00005-0. URL http://linkinghub.elsevier.com/retrieve/pii/S0968432899000050.

[61] W. W. Molzen, A. N. Broers, J. J. Cuomo, J. M. E. Harper, and R. B. Laibowitz. Materials and techniques used in nanostructure fabrication. *J. Vac. Sci. Technol.*, 16(2):269–272, mar 1979. ISSN 0022-5355. doi: 10.1116/1.569924. URL http://avs.scitation.org/doi/10.1116/1.569924.

[62] J. R. Vig. UV/ozone cleaning of surfaces. *J. Vac. Sci. Technol. A Vacuum, Surfaces, Film.*, 3(3):1027–1034, may 1985. ISSN 0734-2101. doi: 10.1116/1.573115. URL http://avs.scitation.org/doi/10.1116/1.573115.

[63] J. J. Mock, M. Barbic, D. R. Smith, D. A. Schultz, and S. Schultz. Shape effects in plasmon resonance of individual colloidal silver nanoparticles. *J. Chem. Phys.*, 116(15):6755–6759, apr 2002. ISSN 0021-9606. doi: 10.1063/1.1462610. URL http://aip.scitation.org/doi/10.1063/1.1462610.

[64] K. Siegbahn. ESCA; atomic, molecular and solid state structure studied by means of electron spectroscopy. Technical report, 1967.

[65] C.D. Wagner, W.M. Riggs, L.E. Davis, and J.F Moulder. *Handbook of X-ray Photoelectron Spectroscopy*. Perkin-Elmer Corporation, Eden Prairie, 1979.

[66] B. Warren. *X-ray Diffraction*. Courier Corporation, 1969. ISBN 0486663175.

[67] W. H. Bragg and W. L. Bragg. The Reflection of X-rays by Crystals. *Proc. R. Soc. A Math. Phys. Eng. Sci.*, 88(605):428–438, jul 1913. ISSN 1364-5021. doi: 10.1098/rspa.1913.0040. URL `http://rspa.royalsocietypublishing.org/cgi/doi/10.1098/rspa.1913.0040`.

[68] L. G. Parratt. Surface Studies of Solids by Total Reflection of X-Rays. *Phys. Rev.*, 95(2):359–369, jul 1954. ISSN 0031-899X. doi: 10.1103/PhysRev.95.359. URL `http://link.aps.org/doi/10.1103/PhysRev.95.359`.

[69] J. Als-Nielsen and D. McMorrow. *Elements of Modern X-ray Physics*. John Wiley & Sons, Inc., 2011.

[70] C.W. Oatley, W.C. Nixon, and R.F.W. Pease. Scanning Electron Microscopy. In L. Marton, editor, *Adv. Electron. Electron Phys.*, pages 181–247. Academic Press, 1966.

[71] G. Binnig, C. F. Quate, and Ch. Gerber. Atomic Force Microscope. *Phys. Rev. Lett.*, 56(9):930–933, mar 1986. ISSN 0031-9007. doi: 10.1103/PhysRevLett.56.930. URL `http://link.aps.org/doi/10.1103/PhysRevLett.56.930`.

[72] H. Heinzelmann and D. W. Pohl. Scanning near-field optical microscopy. *Appl. Phys. A Solids Surfaces*, 59(2):89–101, aug 1994. ISSN 0721-7250. doi: 10.1007/BF00332200. URL `http://link.springer.com/10.1007/BF00332200`.

[73] M. I. Stockman, M. F. Kling, U. Kleineberg, and F. Krausz. Attosecond nanoplasmonic-field microscope. *Nat. Photonics*, 1:539–544, sep 2007. ISSN 1749-4885. doi: 10.1038/nphoton.2007.169. URL `http://www.nature.com/doifinder/10.1038/nphoton.2007.169`.

[74] Claude Rulliere, editor. *Femtosecond Laser Pulses*. Springer-Verlag New York, 1998.

[75] Jean-Claude Diels and Wolfgang Rudolph. *Ultrashort Laser Pulse Phenomena*. Academic Press, 2006.

[76] Thomas Schultz and Marc Vrakking, editors. *Attosecond and XUV physics*. Weinheim, 2014.

[77] T. Südmeyer, S. V. Marchese, S. Hashimoto, C. R. E. Baer, G. Gingras, B. Witzel, and U. Keller. Femtosecond laser oscillators for high-field science. *Nat. Photonics*, 2: 599–604, oct 2008. ISSN 1749-4885. doi: 10.1038/nphoton.2008.194. URL `http://www.nature.com/doifinder/10.1038/nphoton.2008.194`.

[78] A. Antonetti, M.M. Malley, G. Mourou, and A. Orszag. High power switching with picosecond precision: Applications to high speed Kerr cell and pockels cell. *Opt. Commun.*, 23(3):435–439, dec 1977. ISSN 00304018. doi: 10.1016/0030-4018(77)90400-X. URL http://linkinghub.elsevier.com/retrieve/pii/003040187790400X.

[79] M. Nisoli, S. De Silvestri, and O. Svelto. Generation of high energy 10 fs pulses by a new pulse compression technique. *Appl. Phys. Lett.*, 68(20):2793–2795, may 1996. ISSN 0003-6951. doi: 10.1063/1.116609. URL http://aip.scitation.org/doi/10.1063/1.116609.

[80] M. Nisoli, S. De Silvestri, O. Svelto, R. Szipöcs, K. Ferencz, Ch. Spielmann, S. Sartania, and F. Krausz. Compression of high-energy laser pulses below 5 fs. *Opt. Lett.*, 22(8):522, apr 1997. ISSN 0146-9592. doi: 10.1364/OL.22.000522. URL https://www.osapublishing.org/abstract.cfm?URI=ol-22-8-522.

[81] C. Vozzi, M. Nisoli, G. Sansone, S. Stagira, and S. De Silvestri. Optimal spectral broadening in hollow-fiber compressor systems. *Appl. Phys. B*, 80(3):285–289, mar 2005. ISSN 0946-2171. doi: 10.1007/s00340-004-1721-1. URL http://link.springer.com/10.1007/s00340-004-1721-1.

[82] F. Böhle, M. Kretschmar, A. Jullien, M. Kovacs, M. Miranda, R. Romero, H. Crespo, U. Morgner, P. Simon, R. Lopez-Martens, and T. Nagy. Compression of CEP-stable multi-mJ laser pulses down to 4 fs in long hollow fibers. *Laser Phys. Lett.*, 11(9):095401, sep 2014. ISSN 1612-2011. doi: 10.1088/1612-2011/11/9/095401. URL http://iopscience.iop.org/article/10.1088/1612-2011/11/9/095401{%}5Cnhttp://stacks.iop.org/1612-202X/11/i=9/a=095401?key=crossref.7f1b86786d7aa34303c75d2347a4d9b8http://stacks.iop.org/1612-202X/11/i=9/a=095401?key=crossref.7f1b86786d7aa34303c75d2347a4d9b8.

[83] H.R. Telle, G. Steinmeyer, A.E. Dunlop, J. Stenger, D.H. Sutter, and U. Keller. Carrier-envelope offset phase control: A novel concept for absolute optical frequency measurement and ultrashort pulse generation. *Appl. Phys. B*, 69(4):327–332, oct 1999. ISSN 0946-2171. doi: 10.1007/s003400050813. URL http://link.springer.com/10.1007/s003400050813.

[84] Th. Udem, R. Holzwarth, and T. W. Hänsch. Optical frequency metrology. *Nature*, 416(6877):233–237, mar 2002. ISSN 0028-0836. doi: 10.1038/416233a. URL http://www.nature.com/doifinder/10.1038/416233a.

[85] T. Fuji, J. Rauschenberger, A. Apolonski, V. S. Yakovlev, G. Tempea, T. Udem, C. Gohle, T. W. Hänsch, W. Lehnert, M. Scherer, and F. Krausz. Monolithic carrier-envelope phase-stabilization scheme. *Opt. Lett.*, 30(3):332, feb 2005. ISSN 0146-9592. doi: 10.1364/OL.30.000332. URL https://www.osapublishing.org/abstract.cfm?URI=ol-30-3-332.

[86] G. G. Paulus, F. Lindner, H. Walther, A. Baltuška, E. Goulielmakis, M. Lezius, and F. Krausz. Measurement of the Phase of Few-Cycle Laser Pulses. *Phys. Rev. Lett.*, 91 (25):253004, dec 2003. ISSN 0031-9007. doi: 10.1103/PhysRevLett.91.253004. URL http://link.aps.org/doi/10.1103/PhysRevLett.91.253004.

[87] T. Wittmann, B. Horvath, W. Helml, M. G. Schätzel, X. Gu, Adrian L. Cavalieri, G. G. Paulus, and R. Kienberger. Single-shot carrier–envelope phase measurement of few-cycle laser pulses. *Nat. Phys.*, 5:357–362, may 2009. ISSN 1745-2473. doi: 10.1038/nphys1250. URL http://www.nature.com/nphys/journal/v5/n5/abs/nphys1250.html{%}5Cnpapers3://publication/doi/10.1038/NPHYS1250http://www.nature.com/doifinder/10.1038/nphys1250.

[88] L. V. Keldysh. Ionization in the field of a strong electromagnetic wave. *Sov. Phys. JETP*, 20(5):1307–1314, 1965. ISSN 0038-5646. doi: 10.1234/12345678.

[89] P. B. Corkum and Ferenc Krausz. Attosecond science. *Nat. Phys.*, 3:381–387, jun 2007. ISSN 1745-2473. doi: 10.1038/nphys620. URL http://www.nature.com/doifinder/10.1038/nphys620.

[90] M.V. Ammosov, N.B. Delone, and V.P. Krainov. Tunnel ionization of complex atoms and of atomic ions in an alternating electromagnetic field. *Sov. Phys. JETP*, 64(6):1191, oct 1986. URL http://proceedings.spiedigitallibrary.org/proceeding.aspx?articleid=1243407http://www.ncbi.nlm.nih.gov/pubmed/22232002.

[91] A. Scrinzi, M. Geissler, and T. Brabec. Ionization Above the Coulomb Barrier. *Phys. Rev. Lett.*, 83(4):706–709, jul 1999. ISSN 0031-9007. doi: 10.1103/PhysRevLett.83.706. URL http://link.aps.org/doi/10.1103/PhysRevLett.83.706.

[92] E. Goulielmakis. Attosecond photonics: Extreme ultraviolet catastrophes. *Nat. Photonics*, 6(3):142–143, feb 2012. ISSN 1749-4885. doi: 10.1038/nphoton.2012.28. URL http://www.nature.com/doifinder/10.1038/nphoton.2012.28.

[93] Peter Hommelhoff and Matthias F. Kling, editors. *Attosecond Nanophysics*. Weinheim, 2015.

[94] M. Lewenstein, Ph. Balcou, M. Yu. Ivanov, Anne L'Huillier, and P. B. Corkum. Theory of high-harmonic generation by low-frequency laser fields. *Phys. Rev. A*, 49(3):2117–2132, mar 1994. ISSN 1050-2947. doi: 10.1103/PhysRevA.49.2117. URL http://link.aps.org/doi/10.1103/PhysRevA.49.2117.

[95] N. A. Papadogiannis, B. Witzel, C. Kalpouzos, and D. Charalambidis. Observation of Attosecond Light Localization in Higher Order Harmonic Generation. *Phys. Rev. Lett.*, 83(21):4289–4292, nov 1999. ISSN 0031-9007. doi: 10.1103/PhysRevLett.83.4289. URL http://link.aps.org/doi/10.1103/PhysRevLett.83.4289.

[96] P. M. Paul. Observation of a Train of Attosecond Pulses from High Harmonic Generation. *Science (80-.).*, 292(5522):1689–1692, jun 2001. ISSN 00368075. doi: 10.1126/science.1059413. URL http://www.sciencemag.org/cgi/doi/10.1126/science.1059413.

[97] F. Calegari, G. Sansone, S. Stagira, C. Vozzi, and M. Nisoli. Advances in attosecond science. *J. Phys. B At. Mol. Opt. Phys.*, 49(6):062001, mar 2016. ISSN 0953-4075. doi: 10.1088/0953-4075/49/6/062001. URL http://stacks.iop.org/0953-4075/49/i=6/a=062001?key=crossref.a15311cab3a49d414b4941055efba6d0.

[98] F. Ferrari, F. Calegari, M. Lucchini, C. Vozzi, S. Stagira, G. Sansone, and M. Nisoli. High-energy isolated attosecond pulses generated by above-saturation few-cycle fields. *Nat. Photonics*, 4(12):875–879, dec 2010. ISSN 1749-4885. doi: 10.1038/nphoton.2010.250. URL http://dx.doi.org/10.1038/nphoton.2010.250http://www.nature.com/doifinder/10.1038/nphoton.2010.250.

[99] H. Mashiko, S. Gilbertson, C. Li, S. D. Khan, M. M. Shakya, E. Moon, and Z. Chang. Double Optical Gating of High-Order Harmonic Generation with Carrier-Envelope Phase Stabilized Lasers. *Phys. Rev. Lett.*, 100(10):103906, mar 2008. ISSN 0031-9007. doi: 10.1103/PhysRevLett.100.103906. URL http://link.aps.org/doi/10.1103/PhysRevLett.100.103906.

[100] K. Taec Kim, C. Zhang, T. Ruchon, J.-F. Hergott, T. Auguste, D. M. Villeneuve, P. B. Corkum, and F. Quéré. Photonic streaking of attosecond pulse trains. *Nat. Photonics*, 7(8):651–656, jul 2013. ISSN 1749-4885. doi: 10.1038/nphoton.2013.170. URL http://www.nature.com/nphoton/journal/v7/n8/pdf/nphoton.2013.170.pdfhttp://www.nature.com/doifinder/10.1038/nphoton.2013.170.

[101] F. Krausz and M. Ivanov. Attosecond physics. *Rev. Mod. Phys.*, 81(1):163–234, feb 2009. ISSN 0034-6861. doi: 10.1103/RevModPhys.81.163. URL http://link.aps.org/doi/10.1103/RevModPhys.81.163.

[102] Stefan Hüfner. *Photoelectron spectroscopy: principles and applications*, volume 82. Springer-Verlag, Berlin Heidelberg, 3rd edition, 1995. ISBN 3662032090.

[103] S. Tougaard and P. Sigmund. Influence of elastic and inelastic scattering on energy spectra of electrons emitted from solids. *Phys. Rev. B*, 25(1):4452, sep 1982. ISSN 0163-1829. doi: 10.1103/PhysRevB.32.2808. URL https://doi.org/10.1103/PhysRevB.25.4452.

[104] S. Tanuma, T. Shiratori, T. Kimura, K. Goto, S. Ichimura, and C. J. Powell. Experimental determination of electron inelastic mean free paths in 13 elemental solids in the 50 to 5000 eV energy range by elastic-peak electron spectroscopy. *Surf. Interface Anal.*, 37(11):833–845, nov 2005. ISSN 0142-2421. doi: 10.1002/sia.2102. URL http://doi.wiley.com/10.1002/sia.2102.

[105] F. Quéré, Y. Mairesse, and J. Itatani. Temporal characterization of attosecond XUV fields. *J. Mod. Opt.*, 52(2-3):339–360, jan 2005. ISSN 0950-0340. doi: 10.1080/09500340412331307942. URL http://www.tandfonline.com/doi/abs/10.1080/09500340412331307942.

[106] E. Goulielmakis. Direct Measurement of Light Waves. *Science (80- .).*, 305:1267–1269, aug 2004. ISSN 0036-8075. doi: 10.1126/science.1100866. URL http://www.ncbi.nlm.nih.gov/pubmed/15333834http://www.sciencemag.org/cgi/doi/10.1126/science.1100866.

[107] A. L. Cavalieri, N. Müller, Th. Uphues, V. S. Yakovlev, A. Baltuška, B. Horvath, B. Schmidt, L. Blümel, R. Holzwarth, S. Hendel, M. Drescher, U. Kleineberg, P. M. Echenique, R. Kienberger, F. Krausz, and U. Heinzmann. Attosecond spectroscopy in condensed matter. *Nature*, 449:1029–1032, oct 2007. ISSN 0028-0836. doi: 10.1038/nature06229. URL http://www.ncbi.nlm.nih.gov/pubmed/17960239http://www.nature.com/doifinder/10.1038/nature06229.

[108] S. Neppl. *Attosecond Time-Resolved Photoemission from Surfaces and Interfaces*. PhD thesis, Technische Universität München, 2012.

[109] E. Skopalová, D. Y. Lei, T. Witting, C. Arrell, F. Frank, Y. Sonnefraud, S. A. Maier, J. W. G. Tisch, and J. P. Marangos. Numerical simulation of attosecond nanoplasmonic streaking. *New J. Phys.*, 13(8):083003, aug 2011. ISSN 1367-2630. doi: 10.1088/1367-2630/13/8/083003. URL http://stacks.iop.org/1367-2630/13/i=8/a=083003?key=crossref.9a33e61b66fedafe415bda0969ce1dd6.

[110] F. Kelkensberg, A. F. Koenderink, and M. J. J. Vrakking. Attosecond streaking in a nano-plasmonic field. *New J. Phys.*, 14(9):093034, sep 2012. ISSN 1367-2630. doi: 10.1088/1367-2630/14/9/093034. URL http://stacks.iop.org/1367-2630/14/i=9/a=093034?key=crossref.0a4d8d9e8362371a6e3d1478c8cefd16.

[111] M. Lupetti, J. Hengster, T. Uphues, and A. Scrinzi. Attosecond Photoscopy of Plasmonic Excitations. *Phys. Rev. Lett.*, 113(11):113903, sep 2014. ISSN 0031-9007. doi: 10.1103/PhysRevLett.113.113903. URL http://link.aps.org/doi/10.1103/PhysRevLett.113.113903.

[112] Viktor Myroshnychenko, Jessica Rodríguez-Fernández, Isabel Pastoriza-Santos, Alison M Funston, Carolina Novo, Paul Mulvaney, Luis M Liz-Marzán, and F Javier García de Abajo. Modelling the optical response of gold nanoparticles. *Chem. Soc. Rev.*, 37(9):1792, 2008. ISSN 0306-0012. doi: 10.1039/b711486a. URL http://xlink.rsc.org/?DOI=b711486a.

[113] B. T. Draine and P. J. Flatau. Discrete-Dipole Approximation For Scattering Calculations. *J. Opt. Soc. Am. A*, 11(4):1491, apr 1994. ISSN 1084-7529. doi: 10.1364/JOSAA.11.001491. URL http://www.opticsinfobase.org/abstract.cfm?URI=josaa-11-4-1491https://www.osapublishing.org/abstract.cfm?URI=josaa-11-4-1491.

[114] F. J. García de Abajo and A Howie. Retarded field calculation of electron energy loss in inhomogeneous dielectrics. *Phys. Rev. B*, 65(11):115418, mar 2002. ISSN 0163-1829. doi: 10.1103/PhysRevB.65.115418. URL http://caslon.stanford.edu:3210/sfxlcl3?url{_}ver=Z39.88-2004{&}ctx{_}ver=Z39.88-2004{&}ctx{_}enc=info:ofi/enc:UTF-8{&}rft{_}val{_}fmt=info:ofi/fmt:kev:mtx:journal{&}rft.genre=article{&}rft.issn=0163-1829{&}rft.coden=PRBMDO{&}rft.date=2002{&}rft.volume=65{&}rft.issue=11{&}rft.spage=11.

[115] F. J. García de Abajo and A. Howie. Relativistic Electron Energy Loss and Electron-Induced Photon Emission in Inhomogeneous Dielectrics. *Phys. Rev. Lett.*, 80(23):5180–5183, jun 1998. ISSN 0031-9007. doi: 10.1103/PhysRevLett.80.5180. URL http://link.aps.org/doi/10.1103/PhysRevLett.80.5180.

[116] A. Taflove and K. R. Umashankar. The Finite-Difference Time-Domain Method for Numerical Modeling of Electromagnetic Wave Interactions. *Electromagnetics*, 10(1-2):105–126, jan 1990. ISSN 0272-6343. doi: 10.1080/02726349008908231. URL http://ebooks.cambridge.org/ref/id/CBO9781107415324A009http://www.tandfonline.com/doi/abs/10.1080/02726349008908231.

[117] U. Hohenester and A. Trügler. MNPBEM – A Matlab toolbox for the simulation of plasmonic nanoparticles. *Comput. Phys. Commun.*, 183(2):370–381, feb 2012. ISSN 00104655. doi: 10.1016/j.cpc.2011.09.009. URL http://linkinghub.elsevier.com/retrieve/pii/S0010465511003274.

[118] A. F. Oskooi, D. Roundy, M. Ibanescu, P. Bermel, J.D. Joannopoulos, and S. G. Johnson. Meep: A flexible free-software package for electromagnetic simulations by the FDTD method. *Comput. Phys. Commun.*, 181(3):687–702, mar 2010. ISSN 00104655. doi: 10.1016/j.cpc.2009.11.008. URL http://linkinghub.elsevier.com/retrieve/pii/S001046550900383X.

[119] W. P. Davey. Precision Measurements of the Lattice Constants of Twelve Common Metals. *Phys. Rev.*, 25(6):753–761, jun 1925. ISSN 0031-899X. doi: 10.1103/PhysRev.25.753. URL http://link.aps.org/doi/10.1103/PhysRev.25.753.

[120] G. Zhan, R. Liang, H. Liang, J. Luo, and R. Zhao. Asymmetric band-pass plasmonic nanodisk filter with mode inhibition and spectrally splitting capabilities. *Opt. Express*, 22(8):9912, apr 2014. ISSN 1094-4087. doi: 10.1364/OE.22.009912. URL http://www.ncbi.nlm.nih.gov/pubmed/24787873https://www.osapublishing.org/oe/abstract.cfm?uri=oe-22-8-9912.

[121] S. L. McCall, A. F J Levi, R. E. Slusher, S. J. Pearton, and R. A. Logan. Whispering-gallery mode microdisk lasers. *Appl. Phys. Lett.*, 60(3):289–291, jan 1992. ISSN 0003-6951. doi: 10.1063/1.106688. URL http://aip.scitation.org/doi/10.1063/1.106688.

[122] W. A. Okell, T. Witting, D. Fabris, C. A. Arrell, J. Hengster, S. Ibrahimkutty, A. Seiler, M. Barthelmess, S. Stankov, D. Y. Lei, Y. Sonnefraud, M. Rahmani, Th. Uphues, S. A. Maier, J. P. Marangos, and J. W. G. Tisch. Temporal broadening of attosecond photoelectron wavepackets from solid surfaces. *Optica*, 2(4):383, apr 2015. ISSN 2334-2536. doi: 10.1364/OPTICA.2.000383. URL https://www.osapublishing.org/abstract.cfm?URI=optica-2-4-383.

[123] William A. Okell. *Ultrafast measurements in condensed matter*. PhD thesis, Imperial College London, 2014.

[124] W. A. Okell, T. Witting, D. Fabris, D. Austin, M. Bocoum, F. Frank, A. Ricci, A. Jullien, D. Walke, J. P. Marangos, R. Lopez-Martens, and J. W. G. Tisch. Carrier-envelope phase stability of hollow fibers used for high-energy few-cycle pulse generation. *Opt. Lett.*, 38(19):3918, oct 2013. ISSN 0146-9592. doi: 10.1364/OL.38.003918. URL http://www.ncbi.nlm.nih.gov/pubmed/24081088https://www.osapublishing.org/abstract.cfm?URI=ol-38-19-3918.

[125] F. Frank, C. Arrell, T. Witting, W. A. Okell, J. McKenna, J. S. Robinson, C. A. Haworth, D. Austin, H. Teng, I. A. Walmsley, J. P. Marangos, and J. W. G. Tisch. Invited Review Article: Technology for Attosecond Science. *Rev. Sci. Instrum.*, 83(7):071101, jul 2012. ISSN 0034-6748. doi: 10.1063/1.4731658. URL http://www.ncbi.nlm.nih.gov/pubmed/22852664http://aip.scitation.org/doi/10.1063/1.4731658.

[126] N. Pfullmann, C. Waltermann, M. Noack, S. Rausch, T. Nagy, C. Reinhardt, M. Kovačev, V. Knittel, R. Bratschitsch, D. Akemeier, A. Hütten, A. Leitenstorfer, and U. Morgner. Bow-tie nano-antenna assisted generation of extreme ultraviolet radiation. *New J. Phys.*, 15(9):093027, sep 2013. ISSN 1367-2630. doi: 10.1088/1367-2630/15/9/093027. URL http://stacks.iop.org/1367-2630/15/i=9/a=093027?key=crossref.3324202cc5d2f60e1abb61d87323cdb8.

[127] O. Hemmers, S. B. Whitfield, P. Glans, H. Wang, D. W. Lindle, R. Wehlitz, and I. A. Sellin. High-resolution electron time-of-flight apparatus for the soft x-ray region. *Rev. Sci. Instrum.*, 69(11):3809–3817, nov 1998. ISSN 0034-6748. doi: 10.1063/1.1149183. URL http://scitation.aip.org/content/aip/journal/rsi/69/11/10.1063/1.1149183{%}5Cnhttp://scitation.aip.org/deliver/fulltext/aip/journal/rsi/69/11/1.1149183.pdf?itemId=/content/aip/journal/rsi/69/11/10.1063/1.1149183{&}mimeType=pdf{&}containerItemId=content/aip/jour.

[128] D. Nečas and P. Klapetek. Gwyddion: an open-source software for SPM data analysis. *Open Phys.*, 10(1), jan 2012. ISSN 2391-5471. doi: 10.2478/s11534-011-0096-2. URL http://www.degruyter.com/view/j/phys.2012.10.issue-1/s11534-011-0096-2/s11534-011-0096-2.xml.

[129] D. A. Shirley. High-Resolution X-Ray Photoemission Spectrum of the Valence Bands of Gold. *Phys. Rev. B*, 5(12):4709–4714, jun 1972. ISSN 0556-2805. doi: 10.1103/PhysRevB.5.4709. URL http://link.aps.org/doi/10.1103/PhysRevB.5.4709.

[130] Y. Mairesse and F. Quéré. Frequency-resolved optical gating for complete reconstruction of attosecond bursts. *Phys. Rev. A*, 71(1):011401, jan 2005. ISSN 1050-2947. doi: 10.1103/PhysRevA.71.011401. URL http://link.aps.org/doi/10.1103/PhysRevA.71.011401.

[131] K. W. DeLong, R. Trebino, and W. E. White. Simultaneous recovery of two ultrashort laser pulses from a single spectrogram. *J. Opt. Soc. Am. B*, 12(12):2463, dec 1995. ISSN 0740-3224. doi: 10.1364/JOSAB.12.002463. URL https://www.osapublishing.org/abstract.cfm?URI=josab-12-12-2463.

[132] T. A. Carlson and G.E. McGuire. Study of the x-ray photoelectron spectrum of tungsten—tungsten oxide as a function of thickness of the surface oxide layer. *J. Electron Spectros. Relat. Phenomena*, 1(2):161–168, jan 1972. ISSN 03682048. doi: 10.1016/0368-2048(72)80029-X. URL http://linkinghub.elsevier.com/retrieve/pii/036820487280029X.

[133] O. F. Schirmer. Dependence of WO3 Electrochromic Absorption on Crystallinity. *J. Electrochem. Soc.*, 124(5):749, 1977. ISSN 00134651. doi: 10.1149/1.2133399. URL http://jes.ecsdl.org/cgi/doi/10.1149/1.2133399.

[134] H. Tsai, E. Hu, K. Perng, M. Chen, J.-C. Wu, and Y.-S. Chang. Instability of gold oxide Au2O3. *Surf. Sci.*, 537(1-3):L447–L450, jul 2003. ISSN 00396028. doi: 10.1016/S0039-6028(03)00640-X. URL http://linkinghub.elsevier.com/retrieve/pii/S003960280300640X.

[135] M. Cardona and L. Ley. *Photoemission in Solids I: General Principles*. Springer-Verlag, Berlin, 1978.

[136] J. Jauhiainen, H. Aksela, S. Aksela, A. Kivimaki, O. P. Sairanen, E. Nommiste, and J. Vegh. Correlation satellites in the Xe N 4,5 -OO and Kr M 4,5 -NN Auger spectra. *J. Phys. B At. Mol. Opt. Phys.*, 28(17):3831–3843, sep 1995. ISSN 0953-4075. doi: 10.1088/0953-4075/28/17/020. URL http://stacks.iop.org/0953-4075/28/i=17/a=020?key=crossref.aa612f5cc2513f8b700619317edd1620.

[137] G. Hermann, C. Liu, J. Manz, B. Paulus, J. F. Pérez-Torres, V. Pohl, and J. C. Tremblay. Multidirectional Angular Electronic Flux during Adiabatic Attosecond Charge Migration in Excited Benzene. *J. Phys. Chem. A*, 120(27):5360–5369, jul 2016. ISSN 1089-5639. doi: 10.1021/acs.jpca.6b01948. URL http://pubs.acs.org/doi/abs/10.1021/acs.jpca.6b01948.

[138] F. Calegari, D. Ayuso, A. Trabattoni, L. Belshaw, S. De Camillis, S. Anumula, F. Frassetto, L. Poletto, A. Palacios, P. Decleva, J. B. Greenwood, F. Martin,

and M. Nisoli. Ultrafast electron dynamics in phenylalanine initiated by attosecond pulses. *Science (80-.).*, 346(6207):336–339, oct 2014. ISSN 0036-8075. doi: 10.1126/science.1254061. URL `http://www.sciencemag.org/cgi/doi/10.1126/science.1254061`.

[139] P. B. Johnson and R. W. Christy. Optical Constants of the Noble Metals. *Phys. Rev. B*, 6(12):4370–4379, dec 1972. ISSN 0556-2805. doi: 10.1103/PhysRevB.6.4370. URL `http://link.aps.org/doi/10.1103/PhysRevB.6.4370`.

[140] E. Palik. *Handbook of Optical Constants of Solids*. Academic Press, Orlando, 1985.